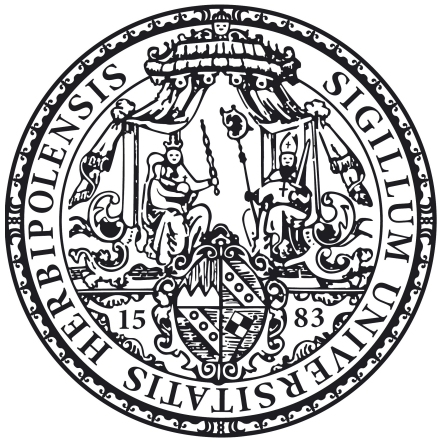

A non-invasive microscopy platform for the online monitoring of hiPSC aggregation in suspension cultures in small-scale stirred tank bioreactors

Entwicklung und Etablierung einer Mikroskopieplattform zur zerstörungsfreien Messung der Aggregierung von hiPSCs in kleinmaßstäbigen Bioreaktor-Suspensionskulturen

Doctoral thesis for a doctoral degree
at the Graduate School of Life Sciences,
Julius-Maximilians-Universität Würzburg,
Section Biomedicine

submitted by

Ivo Peter Schwedhelm

from

Würzburg

Würzburg, 2019

Submitted on: ……..……..

Office stamp

Members of the *Promotionskomitee*:

Chairperson: **Prof. Dr. Markus Engstler**

Primary Supervisor: **Prof. Dr. Jan Hansmann**

Supervisor (Second): **Prof. Dr. Heike Walles**

Supervisor (Third): **Prof. Dr. Philipp Wiedemann**

Date of Public Defence: ……..……

Date of Receipt of Certificates: ……

Für Gabriel. Danke für die Musik.

“Ein gutes Glas Wein ist geeignet, den Verstand zu wecken.”

- Konrad Adenauer

Teilergebnisse der vorliegenden Arbeit wurden als wissenschaftlicher Artikel mit dem Titel “Automated real-time monitoring of human pluripotent stem cell aggregation in stirred tank reactors” am 15.12.2018 zur Veröffentlichung bei *Nature Biomedical Engineering* eingereicht.

Im Rahmen dieses Kooperationsprojektes sind folgende Daten, die in dieser Arbeit zur Erstellung von Abbildungen und Textabschnitten verwendet wurden, durch die Leistungen folgender Co-Autoren entstanden:

- Durchflusszytometrie: Dr. Daniela Zdzieblo (Fraunhofer-Institut für Silicatforschung ISC)
- RNA Isolierung und qRT-PCR: Constantin Berger (Fraunhofer-Institut für Silicatforschung ISC)
- Plasmabehandlung der Bioreaktoren: Dr. Tobias Schmitz (Universitätsklinikum Würzburg)
- PluriTest-Assay: Dr. Bernhard Schuldt, Prof. Dr. Andre Franke, Dr. Franz-Josef Müller (Universitätsklinikum Schleswig-Holstein) und Dr. Ole Pless (Fraunhofer-Institut für Molekularbiologie und Angewandte Oekologie)

Ich möchte mich an dieser Stelle für die gute Zusammenarbeit bedanken.

Abstract

The culture of human induced pluripotent stem cells (hiPSCs) at large-scale becomes feasible with the aid of scalable suspension setups in continuously stirred tank reactors (CSTRs). Suspension cultures of hiPSCs are characterized by the self-aggregation of single cells into macroscopic cell aggregates that increase in size over time. The development of these free-floating aggregates is dependent on the culture vessel and thus represents a novel process parameter that is of particular interest for hiPSC suspension culture scaling. Further, aggregates surpassing a critical size are prone to spontaneous differentiation or cell viability loss. In this regard, and, for the first time, a hiPSC-specific suspension culture unit was developed that utilizes *in situ* microscope imaging to monitor and to characterize hiPSC aggregation in one specific CSTR setup to a statistically significant degree while omitting the need for error-prone and time-intensive sampling. For this purpose, a small-scale CSTR system was designed and fabricated by fused deposition modeling (FDM) using an in-house 3D-printer. To provide a suitable cell culture environment for the CSTR system and *in situ* microscope, a custom-built incubator was constructed to accommodate all culture vessels and process control devices. Prior to manufacture, the CSTR design was characterized *in silico* for standard engineering parameters such as the specific power input, mixing time, and shear stress using computational fluid dynamics (CFD) simulations. The established computational model was successfully validated by comparing CFD-derived mixing time data to manual measurements. Proof for system functionality was provided in the context of long-term expansion (4 passages) of hiPSCs. Thereby, hiPSC aggregate size development was successfully tracked by *in situ* imaging of CSTR suspensions and subsequent automated image processing. Further, the suitability of the developed hiPSC culture unit was proven by demonstrating the preservation of CSTR-cultured hiPSC pluripotency on RNA level by qRT-PCR and PluriTest, and on protein level by flow cytometry.

Zusammenfassung

Die Vermehrung von humanen induzierten pluripotenten Stammzellen (hiPSCs) im Industriemaßstab wird durch skalierbare Bioprozesse in aktiv durchmischten Rührkessel-Bioreaktoren (CSTRs) ermöglicht. Hierbei zeichnet sich das Wachstum von hiPSCs durch die charakteristische Bildung von sphäroidischen Zellaggregaten aus, deren Durchmesser sich im Laufe der Kultivierung vergrößert. Die Agglomeration von hiPSCs ist sowohl abhängig vom Grad der Durchmischung als auch vom jeweiligen Kulturgefäß, und stellt somit einen wichtigen Prozessparameter dar, welcher während der Prozessskalierung berücksichtigt werden muss. Weiterhin weisen hiPSCs in Aggregaten, welche eine kritische Größe überschreiten, eine erhöhte Wahrscheinlichkeit auf, ihre Pluripotenz zu verlieren oder hinsichtlich ihrer Viabilität beeinträchtigt zu werden. Auf Grundlage dessen wurde im Rahmen dieser Arbeit eine Plattform für die Durchführung von hiPSCs-Suspensionskulturen entwickelt, welche die zerstörungsfreie Überwachung des hiPSC-Aggregatwachstums in Echtzeit durch den Einsatz von *in situ*-Mikroskopie ermöglicht. Neben den eigens entworfenen Bioreaktoren, welche zum Großteil aus 3D-gedruckten Komponenten bestehen, wurde eine Peripherie in Form eines Inkubator-Prototyps entwickelt und konstruiert, welcher die Unterbringung der Bioreaktoren, der Systemkomponenten zur Erzeugung von Zellkulturbedingungen sowie einer *in situ*-Mikroskop-Spezialanfertigung gewährleistet. Als Ausgangspunkt der Entwicklung des CSTR Systems diente ein Strömungssimulationsmodell, welches dazu verwendet wurde, prozesstechnische Kennzahlen zu ermitteln um das CSTR System hinsichtlich des spezifischen Leistungseintrags, der Mischzeit und der Scherbelastung zu charakterisieren. Das erstellte Simulationsmodell wurde zudem erfolgreich anhand eines Messdatenabgleichs der Mischzeit hinsichtlich seiner Aussagekraft validiert. Des Weiteren wurde die Funktionsfähigkeit des gesamten Systems durch Langzeitversuche belegt. Hierbei wurden hiPSCs in den entwickelten Bioreaktoren über einen Zeitraum von vier Passagen expandiert und das Aggregatwachstum mittels *in situ*-Mikroskopie in Kombination mit einer automatisierten Bildauswertung beschrieben. Überdies hinaus wurde die Qualität der kultivierten hiPSCs hinsichtlich ihrer Differenzierungskapazität durch den Nachweis von Pluripotenzmarkern auf RNA (qRT-PCR und PluriTest) sowie Proteinebene (Durchflusszytometrie) untersucht.

Contents

Nomenclature

3D	three-dimensional
AC	alternating current
AQ	alanine-glutamine
ATP	adenosine triphosphate
CAD	computer-aided design
CCD	charge-coupled device
cDNA	complementary desoxyribonucleic acid
CFD	computational fluid dynamics
DMEM	dulbecco's modified Eagle's medium
DMSO	dimethyl sulfoxide
ECM	extracellular matrix
EDTA	ethylenediaminetetraacetic acid
ELISA	enzyme-linked immunosorbent assay
ESC	embryonic stem cell
FACS	fluorescence-activated cell sorting
FCS	fetal calf serum
FDM	fused deposition modeling
GABA	gamma-aminobutyric acid
GCDR	gentle cell dissociation reagent
H_2O_2	hydrogen peroxide

hESC human embryonic stem cell

hESC human embryonic stem cells

hiPSC human induced pluripotent stem cell

HMI human-machine interface

HPLC high performance liquid chromatography

ISM *in situ* microscope

LDH lactate dehydroxygenase

LED light-emitting diode

mAb monoclonal antibody

mRNA messenger ribonucleic acid

NSC neural stem cell

PBS- phosphate buffered saline without Ca^{2+} and Mg^{2+}

PEEK polyether ether ketone

PLA polylactic acid

POM-C polyoxymethylene

PPSU polysulfone

qRT-PCR quantitative reverse transcription polymerase chain reaction

RANS Reynolds-averaged Navier-Stokes

rh bFGF recombinant human basic fibroblast growth factor

rh TGF{b} recombinant human transforming growth factor {b}

RNAi RNA interference

RPM revolutions per minute

TE tissue engineering

VH_2O_2 vaporized hydrogen peroxide

Chapter 1

Introduction

1.1 Stem cells - a brief overview

Stem cells are characterized by the cardinal properties of self-renewal for the life span of each individual, and their capability to differentiate into various tissue lineages [128, 141, 2]. Because of these unique features, stem cells are of crucial importance for maintaining tissue homeostasis and for tissue repair after injury [132, 137]. More importantly, stem cells have caused a paradigm shift of conventional medicine by opening the doors for cell-based therapies in several human diseases like ischemic heart disease, dopaminergic neuron replacement in Parkinson disease, and the regeneration of insulin-producing cells for the treatment of type 1 diabetes [150, 85, 176]. Stem cells are categorized according to their differentiation potential as totipotent, multipotent, and pluripotent stem cells. Totipotent cells are capable of forming all cell types of multi-cellular organisms such as the human body, and therefore inherit the greatest differentiation and regeneration potential. However, the only cells that are truly considered totipotent are embryonic cells within the first couple of cell divisions after fertilization [39, 28]. Multipotent cells show the ability to give rise to other cell types but are limited in their ability to differentiate. Their specialization potential is commonly confined to a specific cell lineage, e.g. connective tissue such as bone, cartilage, and adipose tissues [79], or cells that support hematopoiesis [149]. In contrast, pluripotent stem cells demonstrate long-term proliferation potential and show the ability to contribute to cell types of any of the three germ layers, i.e. endoderm, mesoderm, or ectoderm [23, 121, 143].

1.1.1 Adult stem cells

Adult stem cells are unspecialized, multipotent entities with the main role to maintain and repair the tissue in which they are found [133]. They are located in various spaces among differentiated cells in a tissue or organ throughout the body, commonly referred to as stem cell niches [136]. The stem cell niche is the complex *in vivo* microenvironment within which stem cells are sheltered from

differentiation stimuli or apoptotic stimuli [104]. As a direct consequence of this interaction, stem cells are maintained in a quiescent state, induced to self-renewal, or commit to a more specialized entity [41]. Stem cell niches have been been outlined for many tissue types e.g. the hematopoietic stem cell niche in the bone marrow [20], the hair follicle epidermal stem cell niche [172, 83], and the intestinal stem cell niche [168], to name a few.

1.1.2 Human embryonic stem cells

The embryo of mammals is characterized by high developmental plasticity and proliferative capacity, and has traditionally been the preferred source for the isolation of stem cells [14]. Embryonic stem cells (ESCs) are considered pluripotent due to their capability to develop into progenies of the embryonic germ layers *in vitro* [63]. The successful isolation and propagation of ESCs from early mouse embryos has been reported more than 30 years ago [95]. More importantly, knowledge gained from these experiments paved the way for the isolation and *in vitro* culture of human embryonic stem cells (hESCs) [171]. Human embryonic stem cells are derived from blastocysts in cleavage stage human embryos produced by *in vitro* fertilization. In principle, with the establishment of robust cell culture protocols that ensure unlimited proliferation and maintenance of cell "stemness", hESCs serve as an unlimited source of any cell type in the body [189, 144]. Therefore, hESCs represent the starting point for generating *in vitro* models for use in drug discovery, and cell-based therapies to treat impairments like Parkinson disease, spinal cord injury, and juvenile diabetes [140, 171]. Despite their unique potential, ESC-based therapies remain controversial. For instance, a major concern that severely limits the use of ESCs in tissue replacement is the immune response that has been observed against differentiated and undifferentiated cells following allotransplantation into immunocompetent organisms [163, 35, 118, 121]. Further, the harvest of ESCs from human embryos and their later use as cell reservoir gave rise to serious ethical concerns, thereby limiting the widespread use of hESCs in clinical applications [46]. In an attempt to provide remedy to these ethical and practical limitations, the reinduction of the pluripotent state in somatic cells by direct reprogramming gave rise to a novel stem cell type, commonly referred to as induced pluripotent stem cell (iPSC) [165].

1.1.3 Human induced pluripotent stem cells

Human induced pluripotent stem cells (hiPSCs) were first generated by Yamanaka and co-workers by directly reprogramming the nuclei of differentiated adult fibroblasts from the facial dermis of a 36-year-old Caucasian woman to obtain ESC-like, pluripotent cells [192]. At this time, the reprogramming of human somatic cells has been achieved by the transduction of the quadruplet of transcription factors OCT3/4, SOX-2, c-Myc, and KLF4 by a combination of lentiviral and ecotropic retroviral vectors [165, 195]. Upon the introduction of these factors, cells begin to bypass apoptosis and cell senescence, lose somatic cell characteristics, and undergo a metabolic shift for faster energy generation [166]. These emerging induced pluripotent cells further showed comparable differentiation

potential to that of human embryonic stem cells, and additionally, were marked by a robust proliferation and high telomerase activity [165]. The first advantage over hESCs that comes to mind is the chance to generate autogenic disease models and tissue replacement therapies. The critical aspect of immune rejection is thereby overcome if pluripotent stem cells are directly derived from the patients' somatic cells [48]. An additional ambition is to take advantage of the proliferative and developmental potential that hiPSCs offer. In contrast to hESCs, unprecedented access to differentiated cells that make up the human body is feasible while alleviating ethical controversies.

1.2 Biomarkers for hiPSC pluripotency

The testing of cell pluripotency maintenance is a vital task during stem cell culture. In this sense, a common approach is to characterize the genomic profile of specific marker genes and their progenies that indicate cell pluripotency. In doing so, the overall stem cell quality is ensured and cell differentiation is possible. The most prominent markers for stem cell pluripotency are the transcription factors NANOG, OCT3/4, and SOX-2.

NANOG

NANOG is a highly divergent DNA-binding protein that is commonly found in mammalian pluripotent cells and developing germ cells [21]. Its deletion was shown to cause early embryonic lethality and therefore NANOG is considered essential for early embryonic development [103]. NANOG is expressed in pluripotent ESCs, iPSCs, and in the developing germ-line of mammals, where constitutive expression is responsible for autonomous self-renewal [21, 103, 191]. The presence of NANOG is considered a hallmark of pluripotent cells both *in vivo* and *in vitro*, and thereby offers a robust marker for the pluripotent nature of cells. Consequently, the loss of NANOG expression represents an early indication for cell differentiation [22]. Interestingly, NANOG is not part of the transcription factor quartet that was used in the initial reprogramming of human fibroblasts [165, 192, 182]. Still, due to its core position in the transcriptional network of pluripotency, the selection for endogenous NANOG expression allows for the isolation of fully pluripotent stem cells [121].

OCT3/4

OCT3/4 is a transcription factor that was identified as a novel OCT family protein. In particular, the expression of OCT3/4 has been reported in pluripotent stem cells such as ESCs and germ cells alike [120, 145, 193]. In ESCs, OCT3/4 was found to often bind in partnership with SOX-2, among others [131]. In the absence of OCT3/4, embryo development is severely affected, ultimately leading to the death of embryos *in utero* [111]. Beyond that, the later suppression of OCT3/4 via RNA interference (RNAi) resulted in the spontaneous differentiation in human embryonic cells [198]. Then again, the

up-regulation of OCT3/4 expression above the endogenous level lead to the induction of endoderm lineage commitment in ESCs [115]. These data conclusively indicate that OCT3/4 plays an essential role in embryonic development and the maintenance of pluripotent nature of ESCs.

SOX-2

The SOX family has been shown to play key roles during nearly all stages of mammalian development [66, 111, 7]. Furthermore, proteins of the SOX transcription factor family, in general, regulate their target genes by associating with specific partner factors. For instance, SOX-2 was found to partner with the pluripotency-indicating transcription factor OCT3/4 [142, 196]. Therefore, the duet of SOX-2 and OCT3/4 mark the pluripotent lineage of the early embryo and is required for the generation of iPS cells. In a similar manner as with OCT3/4, the deletion of SOX-2 gave way to spontaneous differentiation in ESCs [96]. Therefore, SOX-2, like OCT3/4, is a crucial factor for the stabilization of pluripotency.

1.3 Pluripotent stem cells in tissue engineering applications

The field of tissue engineering (TE) focuses on creating tissue-like arrangements from functional, differentiated cells *in vitro*. These constructs rely on the combination of cells and scaffolds for physical support to closely mimic the respective *in vivo* environment in the human body [76]. The overall aim of TE is to develop biological substitutes of tissues that are used for disease modeling, pharmaceutical compound testing, tissue regeneration therapies, and toxicology screening. A common issue in TE applications, however, is to secure a source for functional mature cells that maintain the appropriate phenotype and perform the required biological functions in the TE-construct. In early TE efforts, primary cells have been isolated from donor tissue and propagated for use on scaffolds [184, 135, 92]. Primary cells are still routinely in use for some TE applications [169, 97], however, yields and proliferation rates tend to be low and for some phenotypes, e.g. spinal cord neurons, harvesting from a patient or donor is not an option. As an alternative to primary cells from donors, the use of stem cells provides a virtually inexhaustible cell source for theoretically all lineages. Due to the scarce availability and immunological incompatibility of adult stem cells and embryonic stem cells, the generation of iPSCs from various somatic cell types provided a significant boost to the TE community, and the number of reports on tissue constructs that rely on iPSC technology has been increasing rapidly [127, 173, 93]. For example, tissue models of the heart, the liver, and the blood-brain barrier have been described recently [13, 138, 4, 167]. On a larger scope, previous animal model studies also successfully evaluated the potential of hiPSCs and their progenies for tissue regeneration in cell deficiency scenarios such as spinal cord injury, type I diabetes, and Parkinson disease [47, 125, 116].

One of the major challenges that hinders the large-scale implementation in clinical stem cell therapy is the lack of long-term studies to evaluate the tumorigenic risk by genetic mutations in iPSC-derived

tissue grafts [78, 119]. Still, a first clinical trial reported the successful generation of autogenic hiPSC-derived retinal pigment epithelial cells and the transplantation thereof into a patient suffering from neovascular age-related macular degeneration. One year after surgery, the transplanted tissue graft remained intact and showed no sign of tumorigenicity [94], thereby confirming the promising potential of iPSC technology.

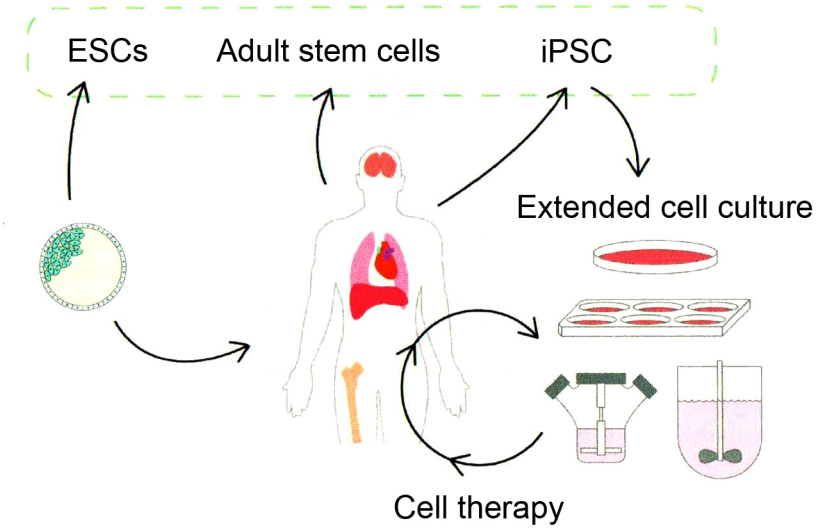

Figure 1.1: *Sources of stem cells for research and tissue engineering purposes. The use of embryonic stem cells (ESCs) is viewed as ethically questionable and cell sources are scarce. Equally, the isolation and in vitro maintenance of adult stem cells outside of their niche is challenging. The reprogramming of sampled adult somatic cells facilitates the generation of induced pluripotent stem cells (iPSCs) that are expanded ex vivo and used for disease modeling and patient-specific cell therapy. Image modified from [124].*

While a few million hiPSCs are adequate to perform research, significantly greater amounts in the order of $10^9 - 10^{12}$ undifferentiated stem cells are required to generate sufficient quantities of differentiated progenies for clinical applications and regenerative purposes [86, 156]. For instance, $1-2\cdot10^9$ cardiomyocytes are needed to replace damaged cardiac tissue after myocardial infarction [57, 110]. Likewise, approximately $1.3\cdot10^9$ insulin-producing beta cells are necessary for insulin independence of a 70-kg patient after islet transplantation [87]. Therefore, the choice of culture system is largely dictated by the intended use and application. In this context, the propagation of hiPSCs *in vitro* is routinely performed as monolayer cultures to create amounts that are sufficient for research purposes. If the main focus, however, is put on the accumulation of hiPSC biomass, undifferentiated hiPSCs are expanded in suspension cultures.

1.4 hiPSC culture strategies

1.4.1 Lab-scale maintenance of hiPSC monolayer cultures

Conventional culture of iPSCs is based on the expansion of adherent cell monolayers to generate cell amounts for routine use. Maintenance culture is commonly performed using polystyrene tissue culture lab-ware for cell expansion, comprising multi-well plates, T-flasks, and Petri dishes of various sizes. Cell proliferation is typically characterized by propagating colonies that merge into larger monolayer patches over the culture duration (fig. 1.2). Besides the advantage of convenient handling during media addition or aspiration, two-dimensional cell layer culture offers equal nutrient supply to all cells while providing optimal visual microscopic accessibility.

A vital component of hiPSC culture is the provision of suitable cell adhesion matrices with surface functionalization to promote E- and N- cadherin-based cell adhesion and cell self-renewal. In this sense, cell culture lab-ware is coated with protein-hydrogel combinations based on structure molecules that serve as *in vitro* basement membrane matrix, e.g. collagen, fibrin, or vitronectin [51]. To mimic the complexities of the natural habitat of human embryonic stem cells (hESCs), an arrangement of appropriate extracellular matrix (ECM) molecules and growth factors is integrated into the hydrogel coating. The required protein extract is derived from Englebreth-Holm-Swarm (EHS) tumors produced in mice, and commonly referred to as Matrigel^{TM}, EHS matrix^{TM}, or Geltrex^{TM}[67, 189, 177]. As stem cell applications are sensitive to culture irregularities through batch-to-batch variations of media supplements, efforts were made to characterize the inherent compositional complexity of Matrigel^{TM} protein extracts. For instance, in a recent proteomic analysis of Matrigel^{TM}, a total of 1851 unique proteins were identified next to the main components laminin, 56 %; collagen IV, 31 %; entactin, 8 % and several growth factors (bFGF, EGF, IGF-1, TGF-β, etc.)[68]. However, the same investigation also revealed that only 53 % batch-to-batch similarity in proteins was given [51]. As a consequence, and with the aim to provide for reproducible cell culture conditions under minimal batch-to-batch variations, efforts are currently made to replace Matrigel^{TM} by chemically defined synthetic hydrogel matrices [109, 32].

Still, Matrigel^{TM} is the current convention for many applications and represents the gold-standard substrate for the expansion of undifferentiated human stem cells [167, 36, 91]. The intrinsic heterogenous composition, however, is widely accepted on behalf of the cost-effectiveness of Matrigel^{TM} basement membrane preparations compared to chemically defined laminin or vitronectin hydrogels [80, 75]. Matrigel^{TM} cell adhesion is primarily conducted via its ECM bulk components laminin and collagen [189]. Collagen harnesses its fibril structures to bind to the integrin $\alpha2\beta1$ membrane receptor domain [59]. Cell attachment to laminin on the other hand is mediated by integrins $\alpha1\beta1$, $\alpha2\beta1$, $\alpha3\beta1$, $\alpha6\beta1$, and $\alpha7\beta1$ [53, 178]. Both human embryonic and induced pluripotent stem cell lines facilitate cell adhesion by the expression of $\alpha5$, $\alpha6$, αV, $\beta1$, and $\beta5$ integrin transmembrane subunits.

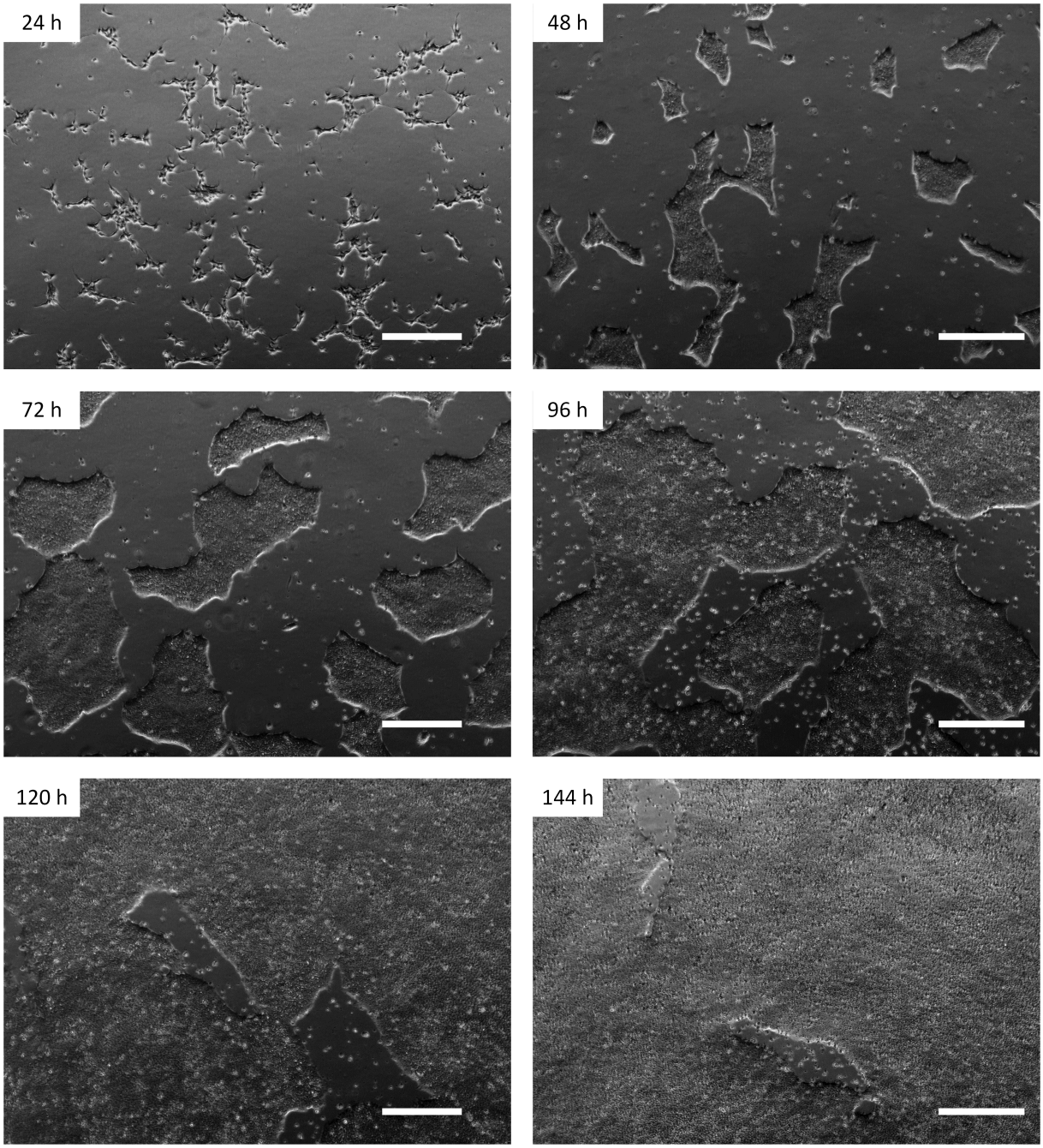

Figure 1.2: *Propagation of IMR 90-4 hiPSCs monolayer colonies cultured in mTeSR™1 medium on Matrigel™ coating. Cell proliferation is characterized by the formation of cell colonies with sharp leading edges. Early colony development is recognizable 24 h after seeding. Cell monolayer clusters reach 95 % confluency after 144 h of culture. Scale bar = 500 µm.*

When culture on Matrigel™ matrices is performed, the proliferation of self-renewing hiPSCs is characterized by rapidly propagating cell colonies. To describe the monolayer growth behavior more precisely, several studies provided a wide range of doubling times of 18 h up to 60 h [151, 99, 190]. Detailed investigations on proliferation kinetics eventually revealed that the diversity between proliferation rates is closely linked to increasing cell senescence on the one hand [129], and to the initial

cell seeding density on the other hand [187]. Several biotechnology companies developed specific stem cell culture media that meet the demanding, complex compositions required for maintaining undifferentiated embryonic stem cells and induced pluripotent stem cells, mTeSR™1 being the most prominent. In contrast to attachment matrix compositions, culture media rely on serum-free, defined formulations that allow for feeder-free maintenance stem cell culture. Next to a DMEM/F12 base, key components comprise human serum albumin, vitamins, antioxidants, trace minerals, specific lipids, γ-aminobutyric acid (GABA), pipecolic acid and cloned growth factors such as recombinant human basic fibroblast growth factor (rh bFGF) and recombinant human transforming growth factor β (rh TGFβ), amongst a wide range of other biochemical substances [90]. During passaging, cell adhesion is segregated by the application of Accutase®, a proteolytic and collagenolytic enzyme solution. Accutase® conveys the natural enzymatic activity of trypsin and collagenase at the same time, which allows its formulation to contain much lower enzyme concentrations. As a consequence, the use of Accutase® is considered less cytotoxic and more gentle during cell detachment, while preserving high dissociation effectiveness [8].

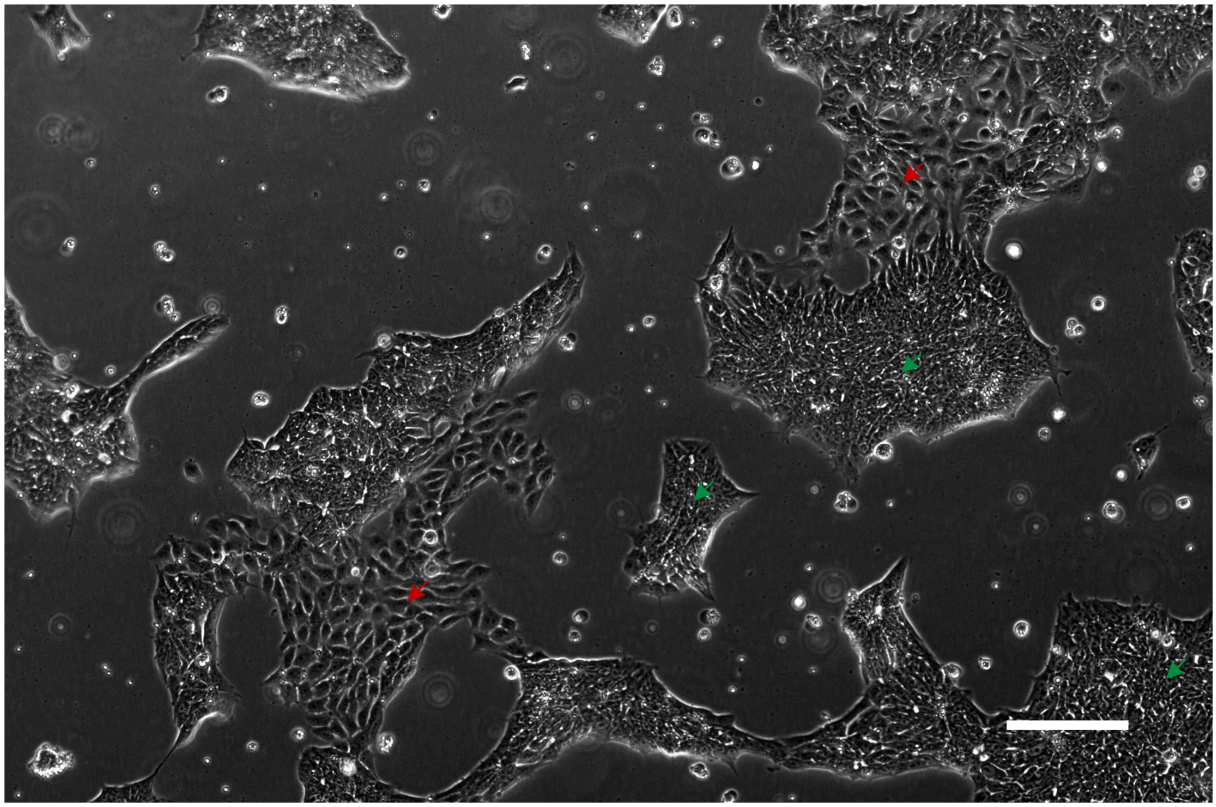

Figure 1.3: *Unwanted, spontaneous differentiation of IMR 90-4 colonies during monolayer maintenance culture. Red arrows indicate regions of cells undergoing undirected differentiation. Green arrows mark cell colonies exhibiting normal hiPSC phenotype. Scale bar = 200 µm.*

The spontaneous, unwanted loss of pluripotency in iPSCs is a gradual event that may occur during culture. The corresponding initiating factors, however, are largely unknown [105]. Yet, a diversity of reasons is believed to trigger iPSCs to exit the pluripotent state and undergo spontaneous differen-

tiation. For instance, physical cues such as temperature or shear stress [10, 82], chemical induction through the availability of growth factors [16, 98], altered cell metabolism [105], and when grown to confluence [171] are aspects that have been reported to lead to spontaneous differentiation *in vitro*. To provide an example, a characteristic change in phenotype of hiPSC monolayer-colonies is shown in figure 1.3. As a consequence, hiPSC cultures that undergo unwanted differentiation during monolayer or suspension culture become unusable for further cell expansion and differentiation endeavors. Therefore, extra care is crucial during iPSC handling, and a robust incubation environment is imperative.

Taken together, the use of standard labware such as T- or shake flasks is adequate for small-scale studies and routine use in research. However, in order to obtain cell numbers that are necessary for clinical applications and tissue regeneration ventures, hiPSCs are cultured as three dimensional (3D) scalable cell suspensions [153].

1.4.2 Scalable hiPSC suspension culture in bioreactors

In the absence of a suitable matrix or scaffold, hiPSC proliferation in suspension is characterized by self-aggregation, and, as a result, the formation of macroscopic spheroids that increase in volume over time [49]. Reports hint that the increased expression of cell-cell attachment proteins E- and N-cadherin plays an important role in the orchestration of the aggregation process. While stem cells that undergo early differentiation are marked by a down-regulation of cell attachment proteins, enriched cadherin levels have been reported for agglomerated stem cells in aggregates. Therefore, the probability of suspended cells with increased E-cad levels to adhere and agglomerate is enhanced. Apart from that, non-aggregated cells are commonly observed to die off quickly [158, 29]. Cell aggregation is further promoted by the agglomeration of two or more free-floating aggregates (fig. 1.4). As a consequence of unhindered aggregation, nutrient and oxygen concentration gradients may occur and affect cell layers in the spheroid centre. Likewise, the removal of metabolic waste products is unbalanced, ultimately leading to cell starvation, undirected differentiation, and necrotic aggregate cores [3, 45]. More importantly, the size of aggregates was shown to have an impact on the subsequent differentiation outcome [9, 18]. Many factors were shown to influence the aggregation behavior in stem cell suspension cultures, e.g. the single cell inoculation density, or the degree of fluid agitation in shaken cultures or actively stirred vessels [148]. The balancing of these aggregation-driving factors is delicate, and mismanagement may quickly lead to over-aggregation and subsequent aggregate clumping (fig. 1.5). As mentioned above, and, in the particular case of extensive cell massing, it is more difficult for cytokines and nutrients to penetrate the aggregates which results in increased undirected differentiation, decreased cell proliferation, and ultimately to culture failure [24].

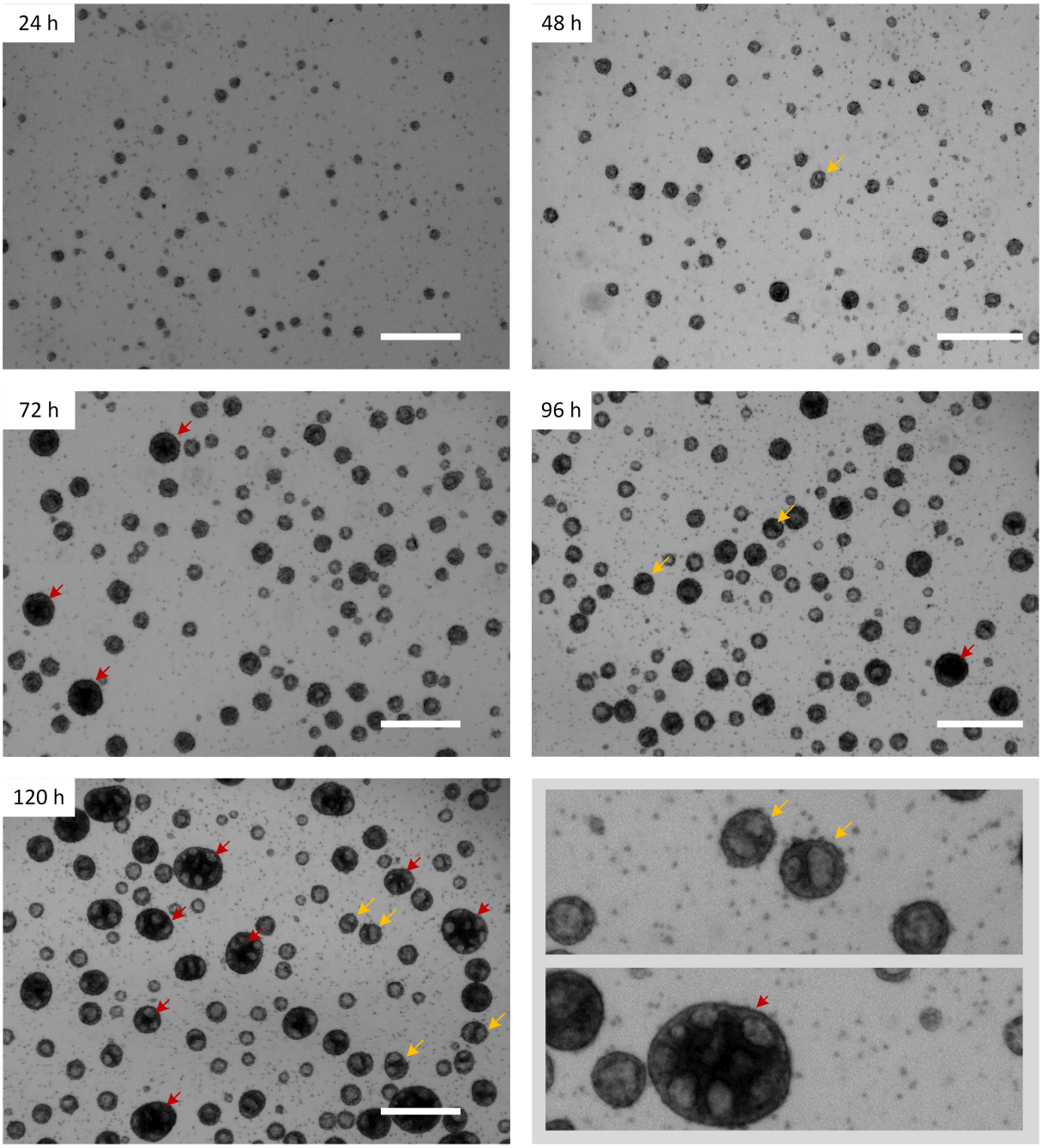

Figure 1.4: *Static suspension culture of IMR 90-4 hiPSC in mTeSR™3D medium. Aggregation of single cells leads to the formation of spheroid-shaped aggregates of increasing size. Yellow arrows indicate the merge of two aggregates into larger entities. Aggregates emerging from the unification of multiple single aggregates are highlighted by red arrows. Magnifications are shown in the bottom right. Scale bar = 500 µm.*

When conducted in a well-defined manner, the format of aggregate-based hiPSC suspension culture offers striking advantages over conventional monolayer culture. For instance, the need for extracellular matrix components that are characterized by high batch-to-batch variations is omitted, thereby paving the way for defined culture conditions that are compliant with good manufacturing practice

(GMP) [64]. Consequently, suspension cultures provide a more homogeneous culture environment, thus decreasing the risk of culture variability [155]. Further, hiPSC suspension bioprocesses are highly prone to automation through controlled liquid handling, which, from an economic point of view, allows for reduced labor costs and increased process reproducibility [4, 155]. In this sense, hiPSC suspension cultures have been shown to be the format-of-choice for generating hiPSC quantities that reach the required biomass scope necessary for clinical applications [202, 112, 65].

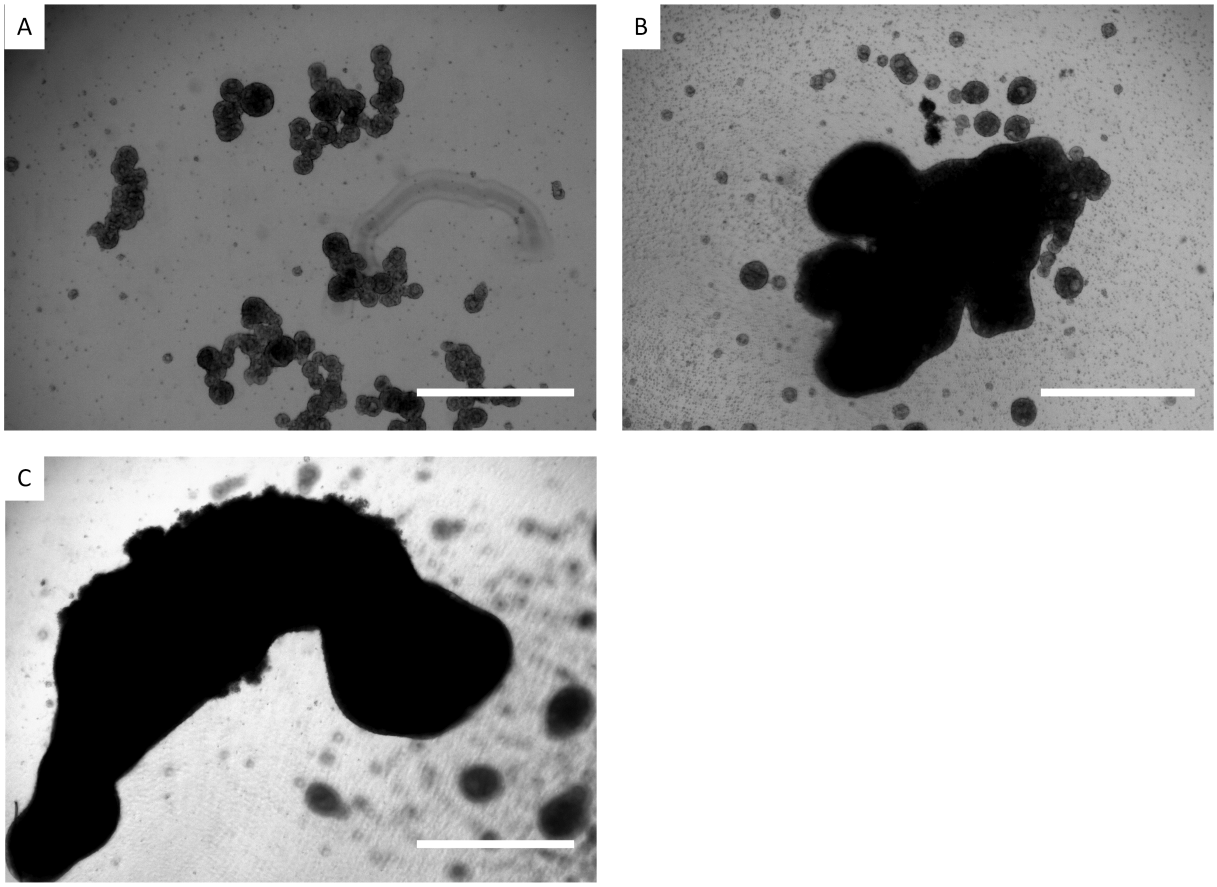

Figure 1.5: *Development of oversized IMR 90-4 hiPSC clumps in static 2 ml suspension cultures in six well plates.* ***(A)*** *Interconnection of smaller aggregates in close proximity.* ***(B)*** *Merge of larger aggregates into a bulky hiPSC patch.* ***(C)*** *Further converging leads to large, irregularly shaped hiPSC clumps. Scale bar = 1000 µm.*

As soon as a bioprocess is successfully established at preliminary small-scale level, a straightforward scale-up to greater culture volumes becomes feasible. Here, a common approach is to start off in small vessels comprising Petri dishes, multi-well plates, or spinner flasks and then transit to continuously stirred tank reactors (CSTRs) of increasing working volumes. CSTRs represent the key element in any biopharmaceutical production process, and have been the gold standard of the pharmaceutical industry for many decades [27]. Besides their scalability, further advantages include the possibility of full process control and automated instrumentation of physical process parameters such as pH and dissolved oxygen, which ultimately contributes to reproducible and robust bioprocesses.

Still, despite the mentioned benefits of scalable suspension cultures, it deserves mentioning that, in contrast to adherent monolayer cultures, a homogenous aggregate hiPSC population is desirable for clinical and industrial applications [30]. On that score, hiPSC aggregation under suspension culture conditions represents an important process parameter that demands specific monitoring.

1.5 CSTR characterization

Next to cell line and cell culture medium, the bioreactor vessel represents the principal starting point for process optimization [88]. Bioprocesses are commonly described by traditional bioengineering parameters that are specific for the current bioreactor vessel and process setup. The investigation of these parameters is necessary to identify key parameters that may need adjustment in terms of process optimization. More importantly, the detailed description of these engineering parameters allows to compare the performance of various bioreactor sizes, which is essential for process transfer in bioreactor scaling studies [11, 44]. Parameters that describe the bioprocess at hand commonly include the flow regime, the maximum fluid velocity, the mixing time, and the specific power input. The determination of a bioreactor's engineering parameters is traditionally performed by experimental methods. However, some parameters may be derived from numeric methods, such as computational fluid dynamics simulations. Thereby, *in silico* bioreactor models are evaluated prior to the actual production stage, which offers more efficient bioreactor design at the development stage.

1.5.1 Fluid flow regime in CSTRs

The fluid flow regime in a stirred bioreactor is described by the Reynolds number N_{Re}, which is derived from the ratio of the inertial forces to the viscous forces in the fluid flow. Therefore, the Reynolds number is a function of fluid-specific parameters and the bioreactor geometry. It is defined by

$$N_{Re} = \frac{\rho N D^2}{\mu} \tag{1.1}$$

where ρ is the fluid density (kg m^{-3}), N is the stirrer rotational speed (s^{-1}), D is the stirrer diameter (m) and μ is the dynamic viscosity of the fluid (Pa s). In principle, three main flow conditions are distinguished: the laminar, transient, and the turbulent flow regime. In stirred vessels, laminar fluid flow is considered for $N_{Re} < 10$, while a fully developed turbulent flow is achieved above a critical Reynolds number of $N_{Re} > 10^4$ [130, 114, 159].

Stirrers are categorized according to their characteristic flow field that is promoted while the fluid is agitated. In principle, two major stirrer types are commonly used for stirred vessels in the bioprocessing field: radial flow and axial flow stirrers. The most prominent examples are Rushton turbines (radial flow) and marine impellers (axial flow). Their typical flow field patterns are promoted in the

presence of baffles. Baffles are lean, flat paddles that are attached to the inner wall of a stirred tank. Their width commonly varies between 1/12 to 1/10 of the tank diameter.

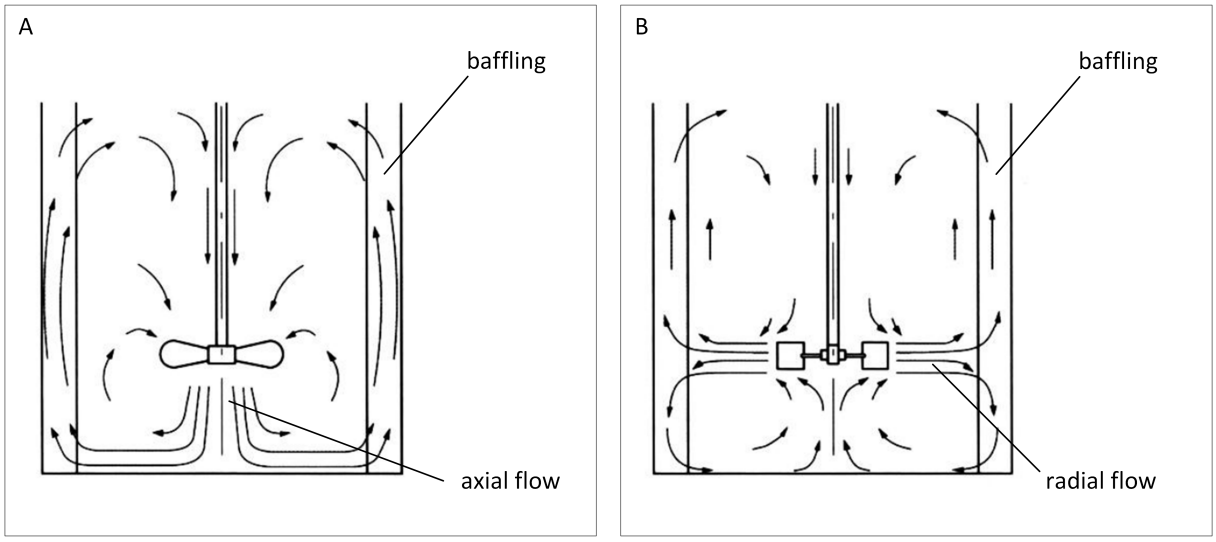

Figure 1.6: *Flow patterns for common stirrer types.* ***(A)*** *Marine stirrers show axial flow circulation.* ***(B)*** *Radial flow is induced by Rushton turbine stirrers. Baffles enhance the pumping capacity of stirrers by preventing the formation of swirl flow by guiding the fluid in the vertical direction. Image modified from Zlokarnik et al. [200].*

In the absence of baffles, the fluid flow pattern is characterized by unhindered, homogeneous swirl flow around the stirrer shaft. In this case, the field velocity components in the axial and radial directions are very small, thereby reducing the mixing efficiency [69]. Hence, the use of baffles prevents the formation of swirl flow patterns and thus promotes top to bottom fluid pumping. In baffled tanks equipped with Rushton turbines, the main flow is horizontally directed from the stirrer towards the vessel wall. For marine impellers, the flow is directed vertically upwards or downwards [113] (fig. 1.6).

1.5.2 Maximum fluid velocity

In a stirred vessel, the maximum fluid velocity u_{max} is equal to the tip speed of the rotating stirrer. This parameter is dictated by the diameter of the stirrer and the corresponding rotation speed. The maximum introduced fluid velocity is calculated according to

$$u_{max} = 2r\pi f \tag{1.2}$$

where r is the stirrer radius (m), and f is the rotation frequency (s^{-1}).

1.5.3 Power input

The specific power input P/V_L (W m^{-3}) describes the electrical energy that is drawn from the motor by the rotating stirrer to agitate the bulk fluid of the bioreactor. It is one of the most important process parameters for the operation of stirred tank vessels [88]. In addition, mixing operations such as particle suspension, fluid homogenization are directly correlated to the specific power input. It is evaluated by a function of the vessel geometry, stirrer configuration, the rotational speed N (s^{-1}), the stirrer diameter D (m), the density of the medium ρ (kg m^{-3}), and the dimensionless Newton power number N_p. The power P consumption (W) is calculated according to

$$P = \rho N^3 D^5 N_P. \tag{1.3}$$

The dimensionless Newton power number N_p represents a stirrer-specific scalar, which may further depend on the bioreactor geometry, stirrer design, vessel baffling, and the Reynolds number N_{Re} [146]. When plotted as a function of N_{Re}, the progression of the Newton power number N_p gives the stirrer-specific power curve (fig. 1.7). Power curves can be used to visualize the dependency of the Newton power number on the current flow regime type, i.e. laminar, transition, and turbulent flow. For the laminar region ($N_{Re} < 10$), the Newton power number N_p is characterized by linear decay. During the transition from laminar to a turbulent flow regime ($10 < N_{Re} < 10^4$), the Newton power number varies continuously according to the stirrer type. As the Reynolds number exceeds 10^4, the flow regime becomes fully turbulent. In this region, the power curve reaches a quasi-constant N_p value, indicating that the power function becomes independent of the Reynolds number. The plateaued value for N_p that is attained in the turbulent flow regime is confined to the used combination of stirrer type and vessel geometry. More importantly, the specific power input P/V_L as well as the N_p value are key characteristics that describe the bioreactor system and thus are of high interest for bioreactor scaling endeavors.

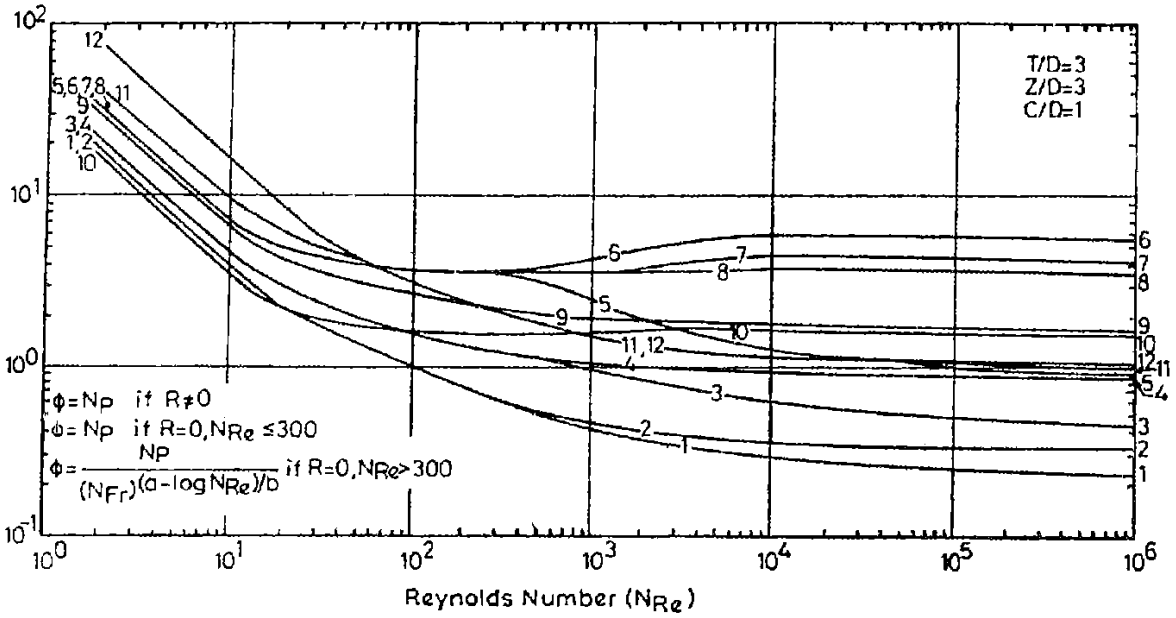

1. Propellers, $p = D$; R = 0; a = 2.1, b = 18, B = 3
2. Propellers, p = D; R = 4; J = 0.1 T; B = 3
3. Propellers, $p = 2D$; R = 0; a = 1.7; b = 18; B = 3
4. Propellers, $p = 2D$; R = 4; J = 0.1T; B = 3
5. Flat blade disc turbine, R = 0; a = 1; 0; b = 40.00
6. Flat blade disc turbine, R = 4; J = 0.1T; B = 6
7. Curved blade disc turbine, R = 4; J = 0.1T; B = 6
8. Arrow-head disc turbine, R = 4; J = 0.1T; B = 6
9. Pitched blade turbine, R = 4; J = 0.1T; B = 8
10. Flat paddle, R = 4; J = 0.1T; B = 2
11. Shrouded turbine, R = 4; J = 0.1T; B = 6
12. Diffuser ring shrouded turbines stator ring having 20 blades, B = 6.

Figure 1.7: *Power number for common stirrer types versus Reynolds number [146].*

1.5.4 Computational fluid dynamics

Computational fluid dynamics simulations are one of the most effective techniques for the mathematical prediction of local and time-dependent flow field velocities, species concentration gradients, energy dissipation, and shear stress [52, 89]. The principal application of CFD in bioprocessing includes the characterization of bioreactors in the pre-, and/or the post-production phase. CFD approaches are typically performed in three work steps: *pre-processing*, *processing*, and *post-processing*. During the *pre-processing*, a model geometry is created *in silico*. This is either done in the CFD software directly, or more complex computer-aided design (CAD) files are generated with the help of advanced design tools. Furthermore, the geometry is assigned with the required physics for fluid dynamics and boundary conditions. Boundary conditions represent an essential component of the computational model as they are used to confine the model. Boundary conditions direct motion of

flow by prescribing the value of a variable at the boundary, e.g. the flow velocity is set to zero at walls ($u = 0$). Lastly, the model geometry is subdivided into a finite number of control elements, which is commonly referred to as "meshing". During the *processing* step, the selected governing equations are solved. Finally, during the *post-processing*, the obtained solution from the processing step is visualized and data extraction is facilitated. CFD studies typically rely on the solving of equations for the conservation of mass and momentum balance, known as the Navier-Stokes equation and the continuity equation. The Navier-Stokes equation is derived from Newton's second law of motion which states that the change of momentum of a body with mass m (kg) traveling at velocity v (m s^{-1}) is directly proportional to the applied force F (N) according to

$$m\frac{dv}{dt} = F. \tag{1.4}$$

In the case of an incompressible Newtonian fluid, the Navier-Stokes equation for stationary fluid flow ($d/dt = 0$) is expressed as

$$\rho\,(u \cdot \nabla u) = -\nabla p + \mu\nabla^2 u + F \tag{1.5}$$

in which u is the fluid velocity (m s^{-1}), p is the fluid pressure (Pa), ρ the fluid density (kg m^{-3}), μ is the fluid dynamic viscosity (Pa s), and F describes acting volume forces (N m^{-3}) e.g. gravity force. Analogous to eq. 1.4, the left side of the equation describes the body mass, which is replaced by the fluid density ρ, and the direction of flow. The right side of the equation represents the sum of acting forces, i.e. pressure force ∇p, internal force $\mu\nabla^2 u$, and external force F. The Navier-Stokes equation is solved together with the continuity equation for incompressible fluids

$$\rho\nabla \cdot u = 0 \tag{1.6}$$

where the Navier-Stokes equation represent the balance for the conservation of momentum, while the continuity equation solves for the conservation of mass.

As the flow velocity increases, the flow regime enters the transition phase and further becomes turbulent. Turbulent flows are characterized by the formation of small eddies that lead to spatial and temporal velocity oscillations. The progression of the flow regime in dependency of the Reynolds number N_{Re} is shown in fig. 1.8 A.

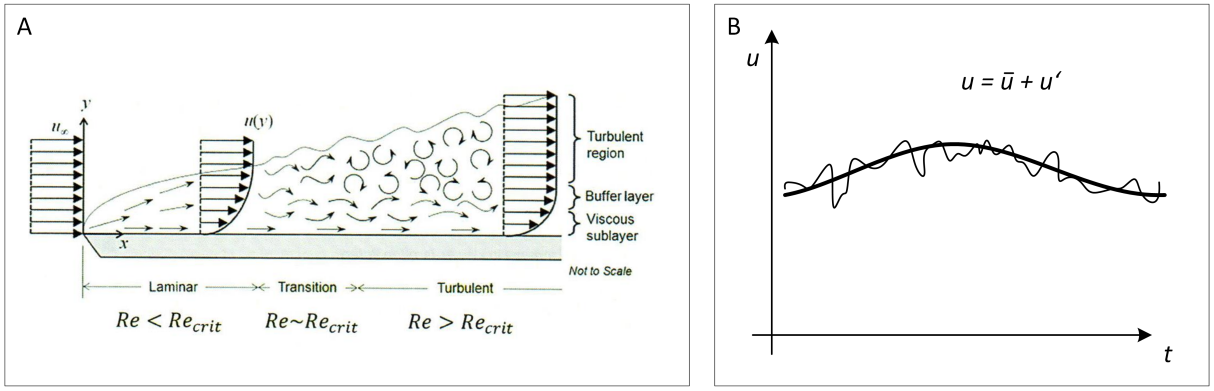

Figure 1.8: *Flow regime in developing turbulent flow.* ***(A)*** *The flow velocity profile for laminar, transient, and turbulent flow is indicated as function of the wall distance u(y).* ***(B)*** *The turbulent flow velocity is averaged by introducing the average flow velocity $\bar{u}$ and the corresponding temporal oscillations term u'. Figure modified from [161].*

From an economical point of view, the exact computation of these velocity fluctuations is unreasonable due to the immense computational effort that is required. Therefore, in order to approximate the altered velocity field in turbulent flow, the Navier-Stokes equations are extended by substitution of the flow variables for velocity u and pressure p by time-averaged formulations

$$u = \bar{u} + u'; \qquad p = \bar{p} + p' \tag{1.7}$$

in order to account for the velocity and pressure fluctuations. In this case, $\bar{u}$ and $\bar{p}$ represent the time averaged variables for the flow velocity and pressure, and u' and p' are introduced to describe the deviation from that average with $\bar{u'} = 0$ and $\bar{p'} = 0$ (fig. 1.8 B). This operation is commonly referred to as Reynolds averaging. Transferring the time-averaged flow variables for velocity and pressure into the Navier-Stokes equation, the Reynolds-Averaged Navier-Stokes (RANS) formulation is

$$\rho \nabla \cdot \bar{u} = 0 \tag{1.8}$$

$$\rho \left(\bar{u} \cdot \nabla \bar{u}\right) = -\nabla \bar{p} + \nabla \bar{\tau} + F. \tag{1.9}$$

Therein, the Reynolds stress tensor $\bar{\tau}$ describes the proportion of inertial viscous forces acting in turbulent fluid flow [62]. It is calculated as a function of the eddy viscosity μ_t (Pa s) and the turbulent kinetic energy k ($m^2\ s^{-2}$) according to

$$\bar{\tau} = \mu_t + \nabla \bar{u} - \frac{2}{3}\rho k. \tag{1.10}$$

By averaging the flow variables, the RANS equations contain more unknowns than equations. Therefore, to solve for the Reynolds stress tensor, the turbulent eddy viscosity μ_t is calculated with the help

of turbulence models that introduce additional transport equations. In most industrial applications, two-equation models are used. The most prominent of these models is the k-ε turbulence model.

k-ε turbulence model

Aspects that render the strength of the k-ε turbulence model favorable lie in its robustness and comparably low computational memory usage. Next to solving for flow mass and momentum balance, the k-ε turbulence model solves for the turbulent viscosity μ_t according to

$$\mu_t = \rho C_\mu \frac{k^2}{\epsilon} \tag{1.11}$$

with the characteristic turbulence model parameters turbulent kinetic energy k, turbulent dissipation ε, and the model constant C_μ. In order to solve for the turbulence parameters, additional transport equations are introduced as

$$\rho(\bar{u}\cdot\nabla)k = \nabla\left(\left(\frac{\mu_t}{\sigma_k}\right)\nabla k\right) + p_k - \rho\epsilon \tag{1.12}$$

$$\rho(\bar{u}\cdot\nabla)\epsilon = \nabla\cdot\left(\left(\frac{\mu_t}{\sigma_\epsilon}\right)\nabla\epsilon\right) + C_{\epsilon 1}\frac{\epsilon}{k}p_k - C_{\epsilon 2}\rho\frac{\epsilon^2}{k} \tag{1.13}$$

with the model constants $C_{\epsilon 1}$, $C_{\epsilon 2}$, σ_k, and σ_ϵ. The k-ε turbulence model performs well to compute flow fields in the bulk fluid domain where turbulent flow is assumed. The flow in the viscous sublayer close to walls, however, is dominated by friction forces which leads to the deceleration of the flow velocity to $u(y) = 0$ (fig. 1.9). Since the flow close to walls can not be assumed turbulent, the k-ε model relies on wall functions that approximate the true flow field close to walls. This approach therefore leads to notably faster computations because a high detail resolution of the viscous sublayer is omitted. On the downside, the viscous sublayer and buffer layer at walls is not accurately simulated, which is an acceptable trade if the flow at walls is of lesser interest.

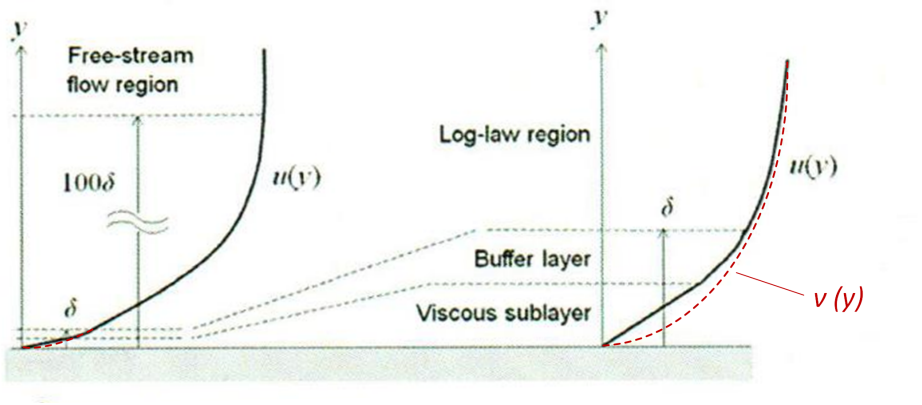

Figure 1.9: *True flow velocity profile $u(y)$ and wall function $v(y)$ in dependency on the wall distance y in turbulent flow. The k-ε turbulence model uses wall functions to describe flow in the viscous sublayer and buffer layer region δ. Modified from [161].*

Low-Reynolds k-ε turbulence model

In contrast to the standard k-ε turbulence model, the Low-Reynolds k-ε turbulence model does not use wall functions and thus provides a very accurate description of the fluid flow in the viscous sublayer and the buffer layer close to walls. As a consequence, the deployment of the Low-Reynolds k-ε model requires very high mesh resolutions close to boundaries to correctly model the transition of laminar flow at the wall to turbulent flow in the free-stream flow region (fig. 1.9). Therefore, the use of this model is linked to considerably elevated computational efforts compared to the standard k-ε model. The Low-Reynolds k-ε turbulence model is commonly used to compute forces that occur in close proximity to boundaries, e.g. lift and drag forces, and is useful to accurately evaluate wall shear stress.

1.6 Aim of study

The successful propagation of hiPSCs in stirred tank systems has been reported by several work groups around the globe, thereby paving the way for scalable bioprocesses that will provide sufficient cell numbers for clinical applications. However, a notable variation concerning the size of hiPSC aggregates is reported, indicating that the aggregation process is strongly culture biased by the culture strategy. The size development of hiPSC aggregates is a critical process parameter that is of high interest for bioprocess scaling endeavors, and little attention has been paid to this aspect, although implications on cell health and differentiation outcome have been reported. In this sense, the prime objective of this study is the development of a tool to monitor the aggregation of hiPSC in suspension cultures. To achieve this goal, a CSTR-based platform that provides for an appropriate culture periphery for the expansion of hiPSCs is designed and constructed. Therein, a stationary *in situ* microscope is used to perform imaging of hiPSC aggregates during suspension culture in a non-destructive manner. From the sampled images, the size distribution of hiPSC aggregates is derived by automated image processing. A second objective is to characterize the developed CSTR design *in silico*. Therefore, a computational model of the CSTR system is developed to derive engineering parameters i.e. power input, shear stress, and mixing time. In doing so, the foundation for bioreactor scaling in future hiPSC experiments is established. A third objective is to provide evidence for system functionality in regard to the expansion of hiPSC in custom-built CSTRs. Therefore, the differentiation capacity of aggregate-cultured hiPSCs is investigated by evaluating the expression of pluripotency-specific biomarkers.

Chapter 2

Materials & Methods

2.1 Materials

2.1.1 Antibodies

Antibody	Working Dilution	Manufacturer
Mouse OCT3/4 human isoform A PE	1:50	BD Biosciences, Heidelberg, Germany
Rat SOX-2 Alexa Fluor® 488 Conjugate	1:50	eBioscience, Frankfurt, Germany
Rabbit NANOG D73G4 XP® mAb Alexa Fluor® 647 Conjugate	1:50	Cell Signaling Technology, Cambridge, UK
Mouse IgG1 kappa isotype control PE	1:50	BD Biosciences, Heidelberg, Germany
Rat IgG2a kappa isotype control Alexa Fluor® 488 Conjugate	1:50	eBioscience, Frankfurt, Germany
Rabbit DA1E mAb IgG XP® Alexa Fluor® 647 Conjugate	1:100	Cell Signaling Technology, Cambridge, UK

2.1.2 Buffers & solutions

Buffer	Composition
FACS buffer	PBS^-, 1 % FCS, 2 mM EDTA

2.1.3 Cell culture media & serums

Medium	Manufacturer
DMEM/F12 without glutamine	ThermoFisher Scientific, Schwerte, Germany
Knock-out serum	ThermoFisher Scientific, Schwerte, Germany
FCS	Bio & Sell, Feucht, Germany
PBS^-	ThermoFisher Scientific, Schwerte, Germany

2.1.4 Chemicals

Chemical	Manufacturer
Accutase® solution	Sigma-Aldrich GmbH, Munich, Germany
Descosept AF	Dr. Schumacher GmbH, Malsfeld, Germany
GCDR	Stemcell Technologies, Inc., Cologne, Germany
Reagent A100	ChemoMetec, Allerod, Denmark
Reagent B	ChemoMetec, Allerod, Denmark
DMSO	Sigma-Aldrich GmbH, Munich, Germany
EDTA	Sigma-Aldrich GmbH, Munich, Germany
Y-27632 dihydrochloride	Tocris Bioscience, Bristol, UK
Matrigel™	Corning, Kaiserslautern, Germany

2.1.5 Consumables

Consumable	Manufacturer
10-ml serological pipette	Greiner bio-one, Frickenhausen, Germany

10-ml syringe LuerLok	BD Biosciences, Heidelberg, Germany
25-ml serological pipette	Greiner bio-one, Frickenhausen, Germany
37-µm Reversible Strainer, Small	Stemcell Technologies, Inc., Cologne, Germany
37-µm Reversible Strainer, Large	Stemcell Technologies, Inc., Cologne, Germany
5-ml serological pipette	Greiner bio-one, Frickenhausen, Germany
50-ml serological pipette	Greiner bio-one, Frickenhausen, Germany
96-well cell culture plate	Greiner bio-one, Frickenhausen, Germany
96-well TC plate white PS F-bottom µ-clear	Greiner bio-one, Frickenhausen, Germany
A35 microtome blades	Feather Safety Razor Co. Ltd., Osaka, Japan
Cell Scraper 16 cm	Sarstedt, Nümbrecht, Germany
Cell Scraper 24 cm	TPP, Trasadingen, Switzerland
CellStar Tubes 15 ml	Greiner bio-one, Frickenhausen, Germany
CellStar Tubes 50 ml	Greiner bio-one, Frickenhausen, Germany
CellStrainer Nylon 40 µm	BD Biosciences, Heidelberg, Germany
Cover glasses 24 x 24 mm	ThermoFisher Scientific, Schwerte, Germany
Cover slips 24 x 60 mm	ThermoFisher Scientific, Schwerte, Germany
Cryo.S 2 ml yellow	Greiner bio-one, Frickenhausen, Germany
EASYstrainer 100 µm	Greiner bio-one, Frickenhausen, Germany
EASYstrainer 40 µm	Greiner bio-one, Frickenhausen, Germany
EASYstrainer 70 µm	Greiner bio-one, Frickenhausen, Germany
Nucleocounter Via1 Cassettes	ChemoMetec, Allerod, Denmark
Nunc Delta 24-well dish	ThermoFisher Scientific, Schwerte, Germany
Nunc Delta 48-well dish	ThermoFisher Scientific, Schwerte, Germany
Nunc Delta 6-well dish	ThermoFisher Scientific, Schwerte, Germany
Pasteur pipette 125 mm	Brand GmbH & Co. KG, Wertheim, Germany
SafeSeal Reaction tube 1.5 ml	Sarstedt, Nümbrecht, Germany
SafeSeal Reaction tube 2 ml	Sarstedt, Nümbrecht, Germany

2.1.6 Hardware

Hardware	Manufacturer
Vacuboy Hand Operator	Integra, Zizers, Switzerland
Waterbath	Hartenstein, Würzburg, Germany
Neubauer Hemocytometer Improved	Hartenstein, Würzburg, Germany
Eppendorf Research Plus pipette 0.5 - 1000 µl	Eppendorf AG, Hamburg, Germany
Eppendorf Research Plus 8 channel pipette 10 - 100 µl	Eppendorf AG, Hamburg, Germany
Nucleocounter NC-200 automated cell counter	ChemoMetec, Allerod, Denmark
FACS Accuri C6 plus flow cytometer	BD Biosciences, Heidelberg, Germany
Cedex Bio Analyzer	Roche Diagnostics, Mannheim, Germany
EVOS XL Cell Imaging System	ThermoFisher Scientific, Schwerte, Germany
In situ microscope imaging unit	Opto GmbH, Gräfelfing, Germany
CFX96 Touch™ Real-Time PCR System	Biorad, Munich, Germany

2.1.7 SPS control system components

All system components were derived from Siemens AG, Erlangen, Germany.

Component	Description
6ES7132-6BF00-0BA0	digital output module
6ES7135-6HD00-0BA1	analog output module
6ES7132-6HD00-0BB1	relay module
6ES7134-6JD00-0CA1	analog input module
6ES7134-6HD00-0BA1	analog input module
6ES7510-1DJ01-0AB0	SIMATIC ET 200SP CPU
6EP1333-2BA20	SITOP PSU100S 24V power supply
6EP1321-5BA20	SITOP PSU100C 12V power supply
6SL3210-5FB10-4UF1	SINAMICS V90 PN power converter
1FL6034-2AF21-1AA1	SIMOTICS S-1FL6 servo drive

2.1.8 Kits

Kit	Manufacturer
LDH Bio Cedex Bio Analyzer Test kit	Roche Diagnostics, Mannheim, Germany
Glucose Cedex Bio Analyzer Test kit	Roche Diagnostics, Mannheim, Germany
Lactate Cedex Bio Analyzer Test kit	Roche Diagnostics, Mannheim, Germany
Ala-Gln Cedex Bio Analyzer Test kit	Roche Diagnostics, Mannheim, Germany
NH_3 Cedex Bio Analyzer Test kit	Roche Diagnostics, Mannheim, Germany
RNeasy Micro or Mini Kit	Quiagen, Hilden, Germany
iScript™ cDNA Synthesis Kit	Biorad, Munich, Germany
SsoFast™ EvaGreen® Supermix	Biorad, Munich, Germany
mTeSR™1	Stemcell Technologies, Inc., Cologne, Germany
mTeSR™3D	Stemcell Technologies, Inc., Cologne, Germany

2.1.9 Software

Software	Manufacturer	Application
OriginLab 9.0	OriginLab, Northampton, MA, USA	General statistics
Prism 6	GraphPad, La Jolla, CA, USA	General statistics
ImageJ	National Institutes of Health, USA	Western blot quantification
Comsol Multiphysics 5.1-5.4	Comsol GmbH, Göttingen, Germany	Finite elements method simulations
Microsoft Excel 2010	Microsoft Corporation	General data analysis
SolidWorks 2015	Dassault Systèmes, Vélizy-Villacoublay, France	Computer aided design

2.2 Methods

2.2.1 General cell culture methods

All hiPSC maintenance cultures were kept in standard lab incubators (Heraeus, Germany) at 37 °C, 5 % CO_2 and 95 % atmosphere humidity. Cell culture medium, washing solutions, and enzyme solutions were pre-warmed to 37 °C prior to use. If not stated otherwise, all centrifugation steps were performed at 200 *g* for 5 min at room temperature. All experiments were performed using the IMR 90-4 hiPS cell line (WiCell, USA). This hiPSC line was derived from IMR 90 fetal lung fibroblasts of a 16 week old female Caucasian fetus by viral transduction of a combination of *OCT3/4*, *SOX-2*, *NANOG*, and *LIN28* genes. IMR 90-4 hiPSCs have a normal karyotype, demonstrate telomerase activity and express ESC surface markers.

Freezing of hiPSCs for long term storage

Long-term storage of hiPSC was accomplished by liquid nitrogen cryoconservation. Cells were detached from underlying matrices by Accutase® (Sigma-Aldrich, Germany) treatment for 5 min at 37 °C. Following, cell suspensions were spun at 300 *g* for 5 min and Accutase® solution was aspirated from the cell pellet. In order to reduce hiPS cell damage during freezing, the cell pellet was resuspended in Knock-out serum containing 10 % dimethyl sulfoxide (DMSO) (Sigma-Aldrich) at a cell concentration of $1 \cdot 10^6$ cells ml^{-1}. Batches of 1 ml cell suspension were evenly distributed among cryoconservation vials. Cells were stored in freezing containers at -80 °C overnight before being transferred to liquid nitrogen storage tanks.

Thawing of hiPSCs for culture inoculation

Cells were extracted from liquid nitrogen storage tanks and the content of each vial was combined with 9 ml pre-warmed mTeSR™1 (Stemcell Technologies, Germany) in a 50-ml centrifuge tube. Cell pellets were dissolved by gently inverting the centrifuge tubes several times. To separate cells from DMSO-containing freezing medium, thawed cells were collected by spinning at 300 *g* for 5 min at room temperature. Medium supernatant was aspirated and cell pellets were resuspended in freshly prepared mTeSR™1 supplemented with 10 µM Y-27632 dihydrochloride (Tocris Bioscience, UK).

2.2.2 Monolayer culture of hiPSCs

Coating of cell culture multi-well plates

To provide a suitable matrix for IMR 90-4 monolayer cultures, Nunclon™Delta multi-well plates (ThermoFisher Scientific, Germany) were coated with Matrigel™ red GF (Corning, Germany). During preparation, coating solutions were kept at 4 °C in DMEM/F-12 (ThermoFisher Scientific) without

L-glutamine (ThermoFisher Scientific) to prevent curing. The coating solution was applied to culture surfaces at a final Matrigel™ concentration of 8.5 µg cm^{-2} and incubated for 1 h at room temperature. After coating was complete, DMEM/F-12 medium was aspirated and plates were ready for cell seeding.

Monolayer cell culture

IMR 90-4 monolayer cultures were started by plating single cells at $2.5 \cdot 10^4$ cells cm^{-2} in mTeSR™1 supplemented with 10 µM Y-27632 dihydrochloride on Matrigel™ plates. After 24 h, cell culture medium was replaced by mTeSR™1 medium without Y-27632 dihydrochloride. From there on, mTeSR™1 medium was routinely replaced every 24 h. Monolayer cultures were passaged when 75 % confluency was reached. Therefore, cell colonies were washed in phosphate buffered saline (PBS^-, ThermoFisher Scientific) and subsequently incubated in Accutase® solution for 6 min to detach cell colonies and generate single cell suspensions. During enzyme incubation, cells were kept at 37 °C in a standard lab incubator. Following incubation, detached cells were collected in 15-ml or 50-ml centrifuge tubes, respectively, and spun for 3 min at 200 *g*. Accutase® solution was aspirated and cell pellets were resuspended in mTeSR™1 culture medium. Cell concentrations were determined by trypan blue staining (0.4 vol%, Sigma-Aldrich) using a Neubauer improved hemocytometer (Sigma-Aldrich). Lastly, IMR 90-4 single cells were re-seeded on Matrigel™ at 1:3 – 1:16 ratios in mTeSR™1 supplemented with 10 µM Y-27632 dihydrochloride.

2.2.3 Suspension culture of hiPSCs

Preparation and maintenance of well plate suspension cultures

Small-scale IMR 90-4 hiPSC suspension cultures were performed in low adhesion cell culture Nunclon™Delta six-well plates. In contrast to monolayer cultures, the plates used for spheroid suspension culture of hiPSC remained uncoated. Suspension cultures were started from adherent IMR 90-4 maintenance colonies cultured on Matrigel™-coated six-well plates. Briefly, mTeSR™1 culture medium was aspirated and cells were washed with PBS^-. Subsequently, PBS^- was replaced by 1 ml of pre-warmed gentle cell dissociation reagent (GCDR, Stemcell Technologies) per well to detach the colonies from the underlying matrix. Thereafter, plates were incubated at 37 °C for 5 min. Following incubation, GCDR was aspirated and replaced by 1 ml of freshly prepared mTeSR™3D seed medium (Stemcell Technologies) supplemented with 10 µM Y-27632 dihydrochloride. hiPSC colonies were carefully detached from the culture plate surface using a cell scraper (Sarstedt, Germany). To generate homogeneously-sized clumps, the colony suspension was gently passed through a 37-µm reversible strainer (Stemcell Technologies) using a 25-ml serological pipette. To determine the cell concentration and/or cell viability, a kit for automated cell count was used. Therein, a sample was taken from the clump suspension and treated with Reagent 100A plus Reagent B (ChemoMetec, Denmark) as

suggested by the manufacturer. Cell counting was performed using a NC-200 automated cell counter (ChemoMetec). Following, hiPSCs were seeded as clumps at $1 \cdot 10^5$ cells ml^{-1} to $1 \cdot 10^6$ cells ml^{-1}in 1 ml culture medium per well. mTeSR™3D medium-based suspension cultures were performed in a 3-day fed-batch manner in which spent medium was only removed prior to passaging. Therefore, for three days after seeding, mTeSR™3D feed medium was added daily (112 µl feed medium to 1 ml seed medium) to replenish nutrients and growth factors.

Continuously stirred tank reactor suspension cultures

Prior to bioreactor cultivations, self-adhesive sensor spots for dissolved oxygen and pH monitoring (Presens, Germany) were attached to the inside walls of the bioreactor glass vessels. A single-use air filter (Sartorius, Germany) was used to allow gas exchange between the incubator atmosphere and the bioreactor headspace. After assembly, bioreactors were sterilized by plasma treatment. Bioreactors were inoculated with clumps prepared as described in section 2.2.3 at seeding concentrations corresponding to $3 \cdot 10^5$ cells ml^{-1} in 62.5 ml mTeSR™3D seed medium supplemented with 10 µM Y-27632 dihydrochloride. During culture, 500 µl samples were taken every 24 h for off-line metabolite concentration and lactate dehydroxygenase (LDH) activity measurements using a Cedex Bio analyzer (Roche Custom Biotech, Germany). Nutrients and growth factors were replenished daily by adding 7 ml of mTeSR™3D feed medium to each bioreactor culture for three days following inoculation. Visual tracking of hiPSC aggregate sizes was accomplished by circulating cell suspension through a glass flow chamber located in the field of vision of a custom-made imaging unit (Opto GmbH, Germany) inside the incubator. Therefore, cell suspensions were bypassed from and to bioreactor vessels using a stationary mounted roller pump (Spetec, Germany) as shown in fig. 3.6 on page 45. Cell suspensions were circulated for 2 min every 24 h. In-flow images were taken every three seconds and automatically processed at-line by a tailored image analysis algorithm (ImageJ, USA).

Passaging of suspension cultures

In order to prevent overgrowth, hiPSC aggregates were dissociated into small clumps on day 4 following inoculation. Therefore, freely floating aggregates were separated from non-viable single cells by filtering the aggregate suspensions using a 37-µm reversible strainer. By doing so, aggregates larger than 37 µm were collected on the strainer surface while cell debris was discarded. Subsequently, aggregates were transferred to a centrifuge tube and resuspended in 10 ml of pre-warmed GCDR to gently macerate the aggregate structures for 5 min. After incubation, cells were spun at 100 *g* for 3 min and the supernatant was aspirated. Finally, aggregates were dissociated by gently taking up the aggregate pellet in 10 ml of freshly prepared mTeSR™3D seed medium supplemented with 10 µM Y-27632 dihydrochloride and slowly passing the aggregate suspension through the same 37-µm reversible strainer. Lastly, cell concentrations were determined as described in section 2.2.3 and cultivation vessels were re-seeded with hiPSC clumps at the desired cell density.

2.2.4 Flow cytometry

Flow cytometry was performed to investigate hiPSC pluripotency marker expression and thus to demonstrate the pluripotent nature of IMR 90-4 cells. Single cell suspensions were prepared by Accutase® treatment of monolayer and spheroid cultures, respectively. All following steps were performed at 4 °C. In total, $2 \cdot 10^5$ cells were stained per marker. All centrifugation steps were performed at 250 *g* and 4 °C. Briefly, cells were washed two times in BD Perm/Wash™ Buffer (BD Biosciences, Germany). After, samples were stained with antibodies priming for transcription factors OCT3/4, SOX-2 and NANOG for 30 min. For marker expression analysis, cells were incubated with PE mouse anti-OCT3/4 (1:50; Human Isoform A, BD Biosciences), rat anti-SOX-2 (1:50; Alexa Fluor® 488 Conjugate, eBioscience, UK) and NANOG (D73G4) XP® Rabbit mAb (1:50; Alexa Fluor® 647 Conjugate, Cell Signaling Technology, Germany). Isotype control samples were stained with with PE mouse IgG1 kappa isotype control (1:50; BD Biosciences), rat IgG2a kappa isotype control Alexa Fluor® 488 Conjugate (1:50; eBioscience) and Rabbit (DA1E) mAb IgG XP® Alexa Fluor® Conjugate 647 (1:100; Cell Signaling Technology). Following antibody incubation, cells were washed two times in BD Perm/Wash™ Buffer (BD Biosciences) followed by one washing step in FACS buffer (PBS^-, 1 % FCS (Bio & Sell), 2 mM ethylenediaminetetraacetic acid (EDTA, Sigma-Aldrich)). Cells were analyzed using a BD FACS Accuri C6 plus flow cytometer (BD Biosciences).

2.2.5 Real time qRT-PCR

RNA isolation was performed using the RNeasy Micro or Mini Kit (Qiagen, Germany). cDNA was synthesized using the iScript™ cDNA Synthesis Kit (Biorad, Germany). qRT-PCR was performed on the CFX96 Touch™ Real-Time PCR Detection System (Biorad) using SsoFast™ EvaGreen® Supermix (Biorad). For calculation of gene expression, the $2^{-\Delta\Delta C_t}$ method was used with hRPL6 and hRPL4 as reference genes. Reactions were performed in duplicates at 60 °C annealing temperature. Further detail on the used primers is provided in tab. 2.10.

Table 2.10: *Primer sequences used for real time qRT-PCR.*

Primer name	Orientation	Sequence
hRPL6	FW	5'-ATTCCCGATCTGCCATGTATTC-3'
	REV	5'-TACCGCCGTTCTTGTCACC-3'
hRPL4	FW	5'-GCCTGCTGTATTCAAGGCTC-3'
	REV	5'-GGTTGGTGCAAACATTCGGC-3'
hOCT4	FW	5'-CCTCACTTCACTGCACTGTA-3'
	REV	5'-CAGGTTTTCTTTCCCTAGCT-3'
hSOX-2	FW	5'-CCCAGCAGACTTCACATGT-3'
	REV	5'-CCTCCCATTTCCCTCGTTTT-3'
hNANOG	FW	5'-CCAAAT TCTCCTGCCAGTGAC-3'
	REV	5'-CACGTGGTTTCCAAACAAGAAA-3'

2.2.6 PluriTest analysis

For PluriTest analysis, RNA was isolated from hiPSC samples using the RNeasy Mini Kit (Qiagen) with an optional on-column DNase Digestion step (RNase-Free DNase Set, Qiagen). For microarray analysis, 200 - 500 ng of total RNA were amplified and biotinylated using the TargetAmp™ - Nano Labeling Kit for Illumina® Expression BeadChip® (Epicentre®, Illumina, USA). Concentration of Biotin-aRNA was measured with a Qubit 3.0 Fluorometer (Thermo Fisher Scientific) and the concentration of each sample was adjusted to 150 ng μl^{-1}. A total of 750 ng of Biotin-aRNA were used for hybridization with the HumanHT12v4-Expression BeadChip™ (Illumina) and hybridization was performed at 58 °C for 16-20 h. After hybridization, BeadChips were washed and stained according to the manufacturer's standard protocol. BeadChips were scanned using the iScan instrument from Illumina®. Raw data (*.idat files) were submitted to PluriTest analysis (www.pluritest.org). PluriTest results were normalized using a published script (https://github.com/pluritest/pluritestCompared.git) [108].

2.2.7 Measurement of metabolite concentrations

Metabolite concentrations were measured using a Cedex Bio Analyzer with appropriate kits. Metabolites of interest included glucose, lactate, lactate dehydrogenase, ammonia, and alanine-glutamine (AQ) amino acid dimer concentrations. Samples of 100 µl were taken from suspension cultures and spun at 300 *g* for 2 min. From the supernatant, a final sample volume of 75 µl was transferred to suitable Cedex cuvettes and measurements were performed according to the manufacturer's instructions.

2.2.8 Cytotoxicity assay

Stainless-steel is commonly the material of choice that makes up most of conventional, reusable bioreactors and storage vessels in the pharmaceutical and food industry. In contrast, the bioreactor components used in this study were largely made from polylactic acid (PLA) as well as other materials. Several options were evaluated for the milled stirrer geometry: stainless steel, polyether ether ketone (PEEK), and polyoxymethylene (POM-C). For this reason, cytotoxicity assays were performed in order to investigate potentially harmful effects by material leaching on hiPSC health. Therefore, a sample of each material was sterilized by plasma treatment as described in 2.2.13, and soaked in 10 ml of freshly prepared mTeSR™3D seed medium at 37 °C for 24 h. After incubation, the tested material samples and the incubation medium were aseptically separated. The incubated medium was subsequently used to start 1 ml hiPSC static suspension cultures in Nunclon™Delta six-well plates at $3 \cdot 10^5$ cells ml^{-1} as described in section 2.2.3. Subsequently, suspension cultures were incubated at 37 °C for 24 h in standard cell culture incubators. Cytotoxic effects were assessed on the basis of cell viability. In this sense, the quantity of available adenosine triphosphate (ATP) in each sample was measured by CellTiter GLO® luminescence assay following the manufacturer's instructions (Promega, Germany). In this respect, cells from each sample were washed and resuspended in 500 µl PBS^-. Following, equal volumes of cell suspension and CellTiter GLO® reagent were mixed. The cell suspension was then transferred to a flat bottom non-binding 96-well plate (Greiner, Germany). For each sample, 200 µl triplicates were measured using an Infinite M200 micro-plate reader (Tecan, Germany).

2.2.9 Incubator-prototype construction

The incubator-protoype was designed using CAD software Solidworks (Dassault Systèmes, Germany) in combination with a library package of aluminum profiles, sealings, and panels (Item GmbH, Germany). For construction, the parts list was extracted from the CAD file and the required parts were obtained from the manufacturer (Item GmbH). The components were subsequently cut to size and manually assembled. Following, system components for process control were installed (Siemens AG, Germany). Lastly, a custom-built *in situ* microscope (Opto GmbH) was fit into the incubator. Details on the used SPS components are provided in section 2.1.7.

2.2.10 Automated image processing

Imaging was achieved by using an image acquisition software provided by the microscope manufacturer (Opto GmbH). Automated image analysis was achieved by generating ImageJ-based image processing algorithms. The image processing was adapted to each imaging unit in use. For this purpose, two algorithms were established and used on images taken by either a digital inverse lab microscope (EVOS XL Cell Imaging System, ThermoFisher Scientific) and the custom-built *in situ* microscope, respectively. Algorithm sequences are presented in supplementary sections 5.1 and 5.2 on page 102.

2.2.11 Computational fluid dynamics simulations

Computational fluid dynamics simulations were performed to mathematically characterize the developed bioreactor design. Aspects of interest involved the flow field that is generated by the stirrer geometry, occurring shear stress during performance, calculation of the stirrer power number, and to estimate the mixing time as a function of the stirring speed. An overview of the study sequences and utilized turbulence models is provided in fig. 2.5 on page 37.

In a first step, a three dimensional computer model of the bioreactor was established. For this purpose, the CAD geometry of the bioreactor fluid domain was generated using Solidworks. To perform fluid dynamics simulations, the model files were subsequently imported into Comsol Multiphysics (Comsol Multiphysics GmbH, Germany) and the "rotating machinery - turbulent flow"- module was applied to the model. Next, material parameters of the fluid model were adjusted to closely match mTeSR™ medium fluid properties as described by Appelt and co-workers [5] and shown in tab. 2.11.

Table 2.11: *Parameters used for computational fluid dynamics simulations*

Parameter name	Value	Unit	Description
N0	0.33…8	s^{-1}	stirrer rotational speed
Da	$3.35 \cdot 10^{-2}$	m	stirrer diameter
rho_u	$9.93 \cdot 10^{-2}$	$kg\ m^{-3}$	mTeSR™1 density at 37 °C
Re_mu	0.765	$mPa\ s$	mTeSR™1 dynamic viscosity at 37 °C

In accordance with experimental conditions, the fluid temperature was set to 37 °C. Following, boundary conditions required for CFD simulations were defined as shown in fig. 2.1. Briefly, a rotating domain comprising the stirrer outline was defined to specify the stirrer agitation region. A "symmetry" boundary condition was applied to the fluid domain liquid/air interface to indicate an opening to the ambient vicinity that forces zero velocity in vertical position of the surface. The fluid domain shell and stirrer surface was specified as "wall" boundary, indicating that the relative velocity is considered zero on all solid/liquid interfaces. Finally, the bioreactor baffles were defined as "interior wall" boundaries. Lastly, a pressure point constraint was defined at the model surface boundary to dictate ambient pressure conditions.

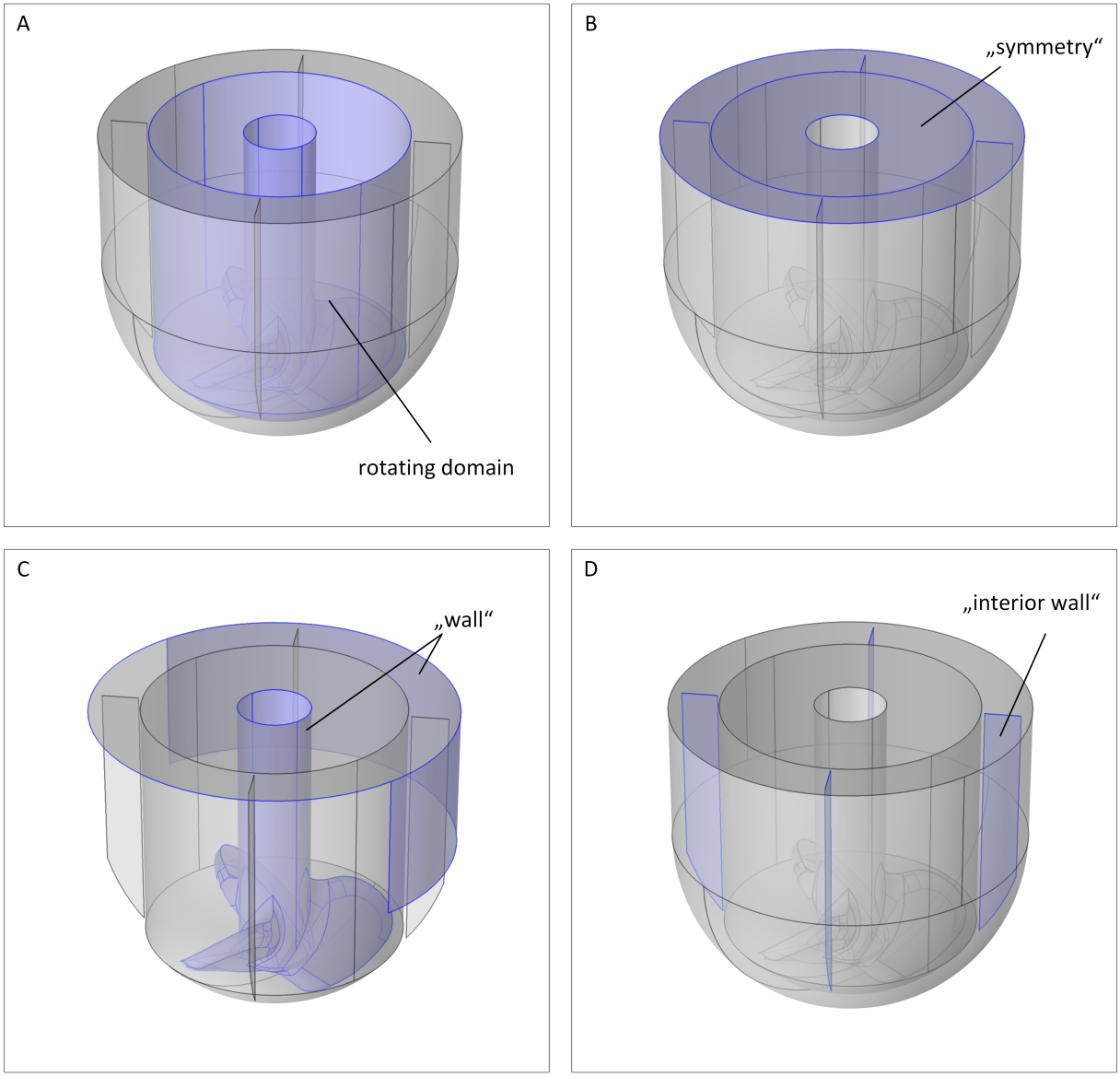

Figure 2.1: *Computational fluid dynamics model setup.* ***(A)*** *The center section of the model comprising the stirrer outline was defined as rotating domain.* ***(B)*** *A symmetry boundary condition was specified for the liquid surface.* ***(C)*** *Remaining boundaries received no-slip wall conditions.* ***(D)*** *Submerged baffles were accounted for by introducing 2D-shapes with interior wall boundary conditions.*

Mesh refinement study

CFD simulations can be performed at any desired degree of detail. However, it is important to recognize that high detail levels entail significantly increased computation efforts. Consequently, a reasonable computation resolution is evaluated prior to launching large-scale simulations. In this sense, a stationary flow field simulation at 120 revolutions per minute (RPM) was performed under varying mesh preset resolutions ranging from “extra coarse” to “extra fine”. From the results, the derived value for the maximum flow velocity was extracted and compared to a reference value calculated by eq. 1.2.

Flow velocity field simulation

For flow velocity field simulations, a stationary solution was computed for a range of stirring speeds from 20 to 600 RPM. Therefore, Comsol's built-in "k-ε turbulent flow" module was utilized to solve the Reynolds-averaged formulation of the Navier-Stokes equations (RANS). The corresponding preset model constants for turbulence fluid flow were used as $C_{\varepsilon 1}$ = 1.44, $C_{\varepsilon 2}$ = 1.92, C_{μ} = 0.09, σ_{κ} = 1.0, σ_{ε} = 1.3, Von Kármán constant K_N = 0.41, and wall roughness B = 5.2. Solver convergence was improved by utilizing "viscosity ramping" as described by Egger and co-workers [37]. The underlying idea of this technique is to solve the problem for higher fluid viscosities and using the solutions as initial conditions for subsequent computations at lower viscosities. Eventually, the actual solution is computed by gradually approximating the final fluid viscosity. In Comsol, auxiliary sweeps are performed to put this technique into practice. Briefly, the fluid dynamic viscosity was subsequently multiplied by the numerical auxiliary factor $visc\_fac$. For a first iteration of the solution, a value of $visc\_fac$ = 100 was defined. Following, stepwise approaches of the final steady-state solution were performed while progressively lowering the auxiliary factor to a final value of $visc\_fac$ = 1. Stationary solutions provided a good estimation of the flow field and pressure distribution. More importantly, they represented the starting point for a range of more detailed CFD simulations (fig. 2.5).

Shear stress estimation

The shear stress that is generated by the stirrer while moving through the bulk fluid was estimated by performing a two-step CFD analysis. First, the stationary solution of the flow field was used to provide initial values for a more detailed resolution of the fluid flow near walls. For this purpose, a subsequent simulation utilizing the Low-Reynolds k-ε turbulence model was performed in a second step. In contrast to the standard k-ε turbulence model, the Low-Reynolds k-ε turbulence model renounces the use of wall functions and thus provides a more accurate solution of the fluid velocity profile within the boundary layers close to walls.

For turbulent flow, the shear stress τ (Pa) that is generated in the bioreactor bulk fluid was calculated as function of the *wall distance y* according to

$$\tau(y) = \tau_v(y) + \tau_t(y) \tag{2.1}$$

where τ_v is the shear stress due to viscous effects and τ_t is the shear stress caused by turbulence.

With the fluid viscosity μ (Pa s) and the flow velocity u (m s^{-1}), the shear stress terms can further be expressed as

$$\tau_v(y) = \mu \frac{\partial u}{\partial y} \tag{2.2}$$

and

$$\tau_t(y) = \mu_t \frac{\partial \bar{u}}{\partial y} = \rho C_\mu \frac{k^2}{\epsilon} \frac{\partial \bar{u}}{\partial y}. \tag{2.3}$$

The term for shear stress due to turbulence further comprises the turbulent eddy viscosity μ_t (Pa s), fluid density ρ (kg m^{-3}), turbulent kinetic energy k (m^2 s^{-2}), turbulent dissipation rate ϵ (m^2 s^{-3}), and the Reynolds-averaged fluid velocity $\bar{u}$ (m s^{-1}). The corresponding syntax expressions for the shear stress equations used by Comsol Multiphysics are noted in table 5.1 in the supplementary section.

Calculation of the Newton power number N_P

The Newton power number N_P describes the power input of the stirrer onto the bulk fluid and is an important characteristic for bioreactor scaling. The power number was calculated according to equation 1.3 by deriving the stirrer power draw P from the computational model of the bioreactor flow regime. Therefore, analogous to shear stress calculations, two-step simulations were performed that comprised the computation of the flow field by subsequently using the k-ε turbulence model and the Low-Reynolds k-ε turbulence model.

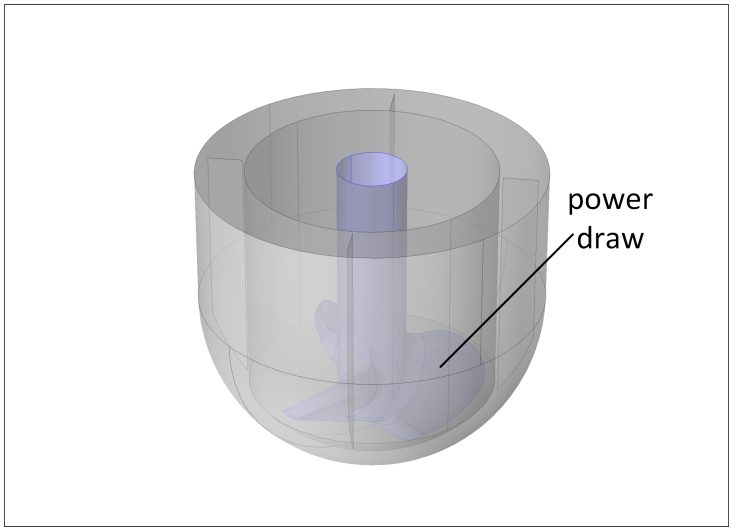

Figure 2.2: *The stirrer power number was calculated by integrating the power draw over the stirrer surface.*

All model parameters that were used are listed in table 5.2 in the supplementary section. Briefly, the area of the submerged stirrer surface was defined as shown in fig. 2.2 and the total torque per area was

computed by integration of the stress tensor on the stirrer surface. Finally, the Newton power number N_P was calculated according to eq. 2.2 on the previous page for both baffled and unbaffled agitation setups across a range of increasing stirring speeds and plotted over the stirrer Reynolds number N_{Re}.

Mixing time computation

To model the mixing time t_m of the bioreactor setup, a tracer substance was virtually injected into the fluid body during mixing. The tracer substance concentration was subsequently tracked and calculated for a matrix of evenly spread points over an estimated time span of mixing. The computation of the mixing time was accomplished by performing a three-step-simulation as outlined in fig. 2.5. First, the stationary solution of the flow field for various stirrer velocities was obtained by using the k-ε turbulence model. In a second simulation, the obtained solutions from the stationary flow field served as initial values for time-dependent studies that calculated the flow field in 0.15 s time steps for a total time span of 60 s.

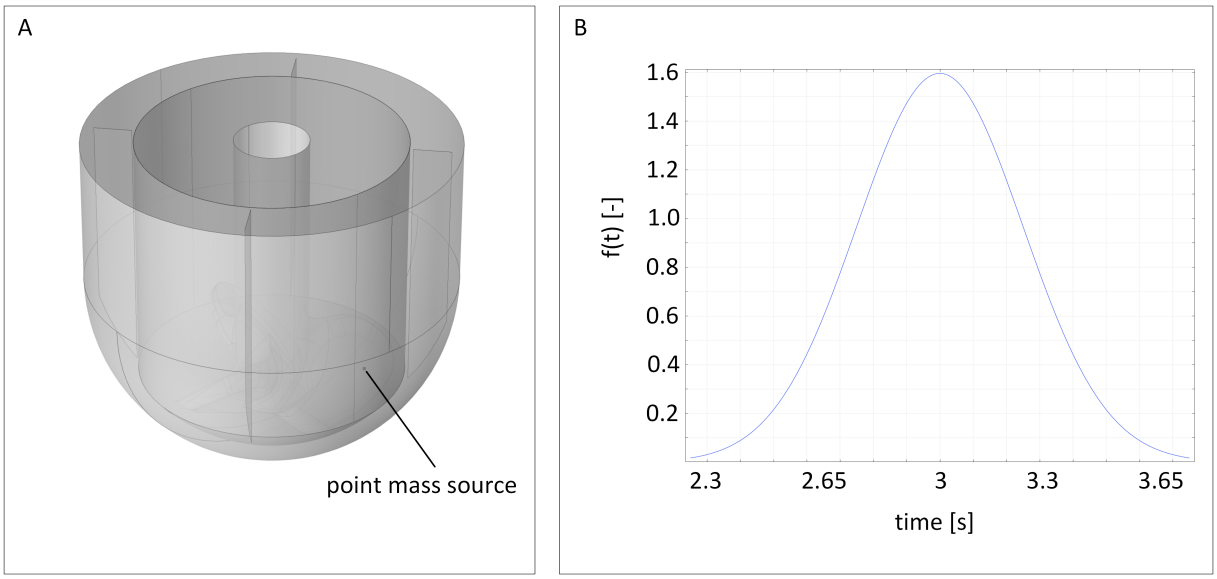

Figure 2.3: *In silico tracer injection setup.* ***(A)*** *The injection of a tracer substance was modeled by defining a point mass source within the fluid domain. At this point, the tracer substance was virtually added to the vessel load while stirring.* ***(B)*** *The tracer substance injection was realized by defining a gaussian function f(t) for the tracer concentration at the point mass source at* $t_{inject} = 3$ *s.*

In a third simulation, Comsol's "transport of diluted species" module was used to define a tracer substance (diffusion coefficient $D_c = 1 \cdot 10^{-9}$ m^2 s^{-1}; turbulent Schmidt number $Sc_T = 1$). The injection of the tracer substance was accomplished by defining a point mass source (fig. 2.3 A) at which the tracer concentration c was prescribed by a gaussian function ($\mu_{f(t)} = 3$ and $\sigma_{f(t)} = 0.25$) (fig. 2.3 B).

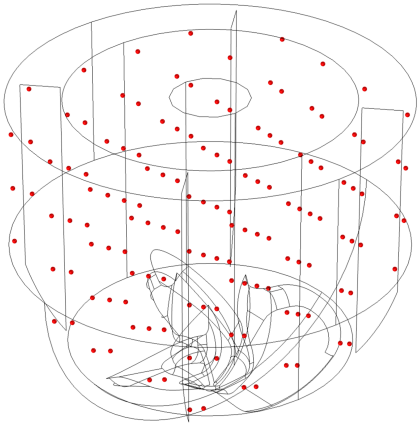

Figure 2.4: *A regular grid point matrix was defined across the computational model to acquire time-dependent tracer concentration curves during mixing.*

In order to study the spreading of the tracer in the stirred vessel, a regular point matrix was generated to extensively cover the agitated fluid domain (fig. 2.4). Subsequently, the tracer concentration was plotted for each point in the matrix as a function of time. The mixing process was considered complete as soon as the tracer concentrations for all points had converged to a steady concentration value within a confidence interval of 90 % and 95 % of the final concentration, respectively.

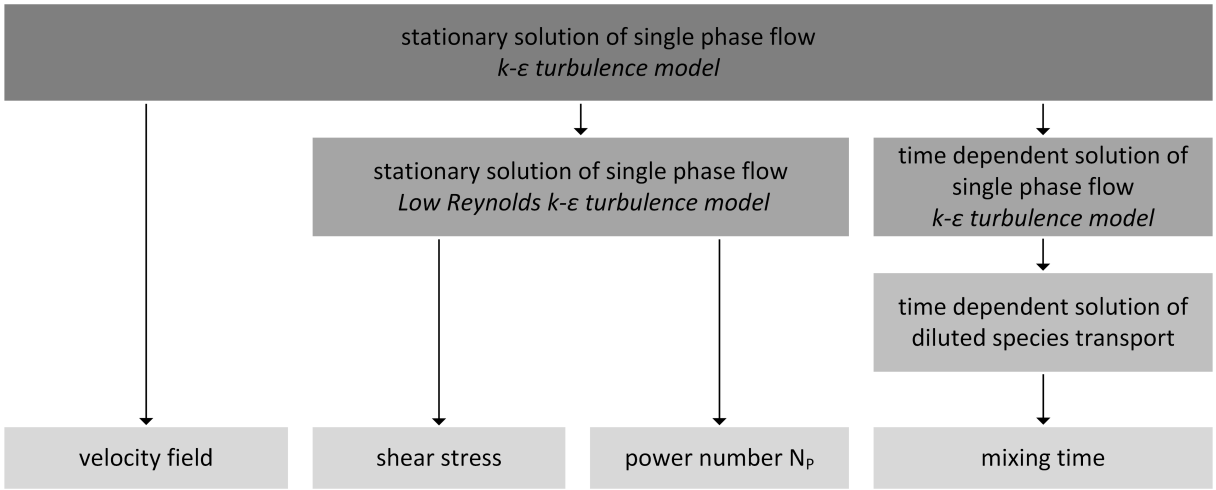

Figure 2.5: *Overview of CFD study sequences and turbulence models. The stationary solution of the fluid flow regime as accounted for by the $k-\varepsilon$ turbulence model was utilized as starting point for a variety of subsequent, more purposive simulations.*

2.2.12 Manual mixing time measurements

The mixing time of miniature stirred tank reactors was visually determined by colorization method. Bioreactors were filled with 100 ml of Millipore water under non-sterile conditions. Stirring was activated and the flow field was allowed to develop for 2 min. Thereafter, 200 µl of phenol red (Sigma-Aldrich) solution (5 vol% in 20 vol% ethanol) was swiftly added through one of the bioreactor ports located in the bioreactor lid. The mixing process was captured on video at all times. Measurements were performed in triplicates for each stirrer agitation speed. Subsequently, the video footage was used to identify the time span until homogenous dye distribution was accomplished.

2.2.13 Plasma sterilization of bioreactor components

Bioreactors were sterilized by VH_2O_2 plasma sterilization method. First, the plasma chamber (Pico Plasma System, Diener electronics, Germany) was heated by a 15 min plasma process using a 100 kHz generator and pure oxygen gas (500 W, 0.3 mbar, 12 sccm O_2). After the first plasma process, the bioreactors wrapped in Stericlin® see-through reels made of paper and film (Stericlin, VP Group, Germany) were inserted into the heated chamber, together with a metal vessel containing 1.5 ml of 60 % H_2O_2 (ThermoFisher Scientific). In order to vaporize the H_2O_2, the chamber was subsequently evacuated to a pressure of 1.0 mbar. The reactors remained in this environment of vaporized H_2O_2 for 90 min, followed by a further evacuation step to 0.4 mbar and a second plasma process with the remaining H_2O_2 vapor as process gas (4 min, 200 W). Finally, a third plasma process using pure oxygen as process gas was carried out to remove the remaining H_2O_2 from the chamber (10 min, 400 W, 12 sccm O_2).

2.2.14 Statistical analysis

Flow cytometry and qRT-PCR data was investigated for statistical deviations using a one-way ANOVA employing Fisher's least significant difference test. For computational modeling-derived mixing times, a One-sample t-test was performed. The investigation of substrate concentration deviations was done using unpaired Student's t-tests. A p-value < 0.05 was considered significant with $n = 3$ for all experiments. All statistical analysis was performed using GraphPad Prism 6 (GraphPad Software Inc., USA).

Chapter 3

Results

3.1 hiPSC-specific culture platform

3.1.1 Incubator system

A versatile platform was designed and constructed to ensures reproducible hiPSC suspension culture performance. Additional requirements that were addressed involved the implementation of process automation and process parameter monitoring. The core of the resultant hiPSC-specific culture platform comprised an all-in-one incubator prototype that was spatially subdivided into three compartments. For an overview, an initial concept drawing is provided in figure 3.1. The resulting device was composed of (1) an incubated space to accommodate CSTRs, motor drive connection cables, and a peristaltic pump for liquid handling of cell suspensions; (2) a cabinet for placing the *in situ* imaging unit; and (3) an additional cabinet to accommodate the required measurement equipment and SIMATIC ET 200SP SPS control system components. The incubator was manually assembled from aluminum profiles and panel elements as shown in fig. 3.2.

For incubator operation, a standard 230 volts AC supply and pressurized CO_2 inlet were required. The incubation compartment provided standard cell culture conditions of 37 °C and a 5 % CO_2 atmosphere for culture medium pH stabilization. To maintain these conditions, CO_2 and temperature sensors were installed to regulate the incubation atmosphere through SPS control (fig. 3.3). A total of four heating foils were attached to the rear panel and the base plate of the incubation chamber to ensure sufficient heat influx for stable cell culture conditions. Fans were installed to either side of the incubation chamber to enhance airflow circulation to promote homogenous heat distribution. In contrast to standard lab incubators, the humidity was kept at room atmosphere niveau.

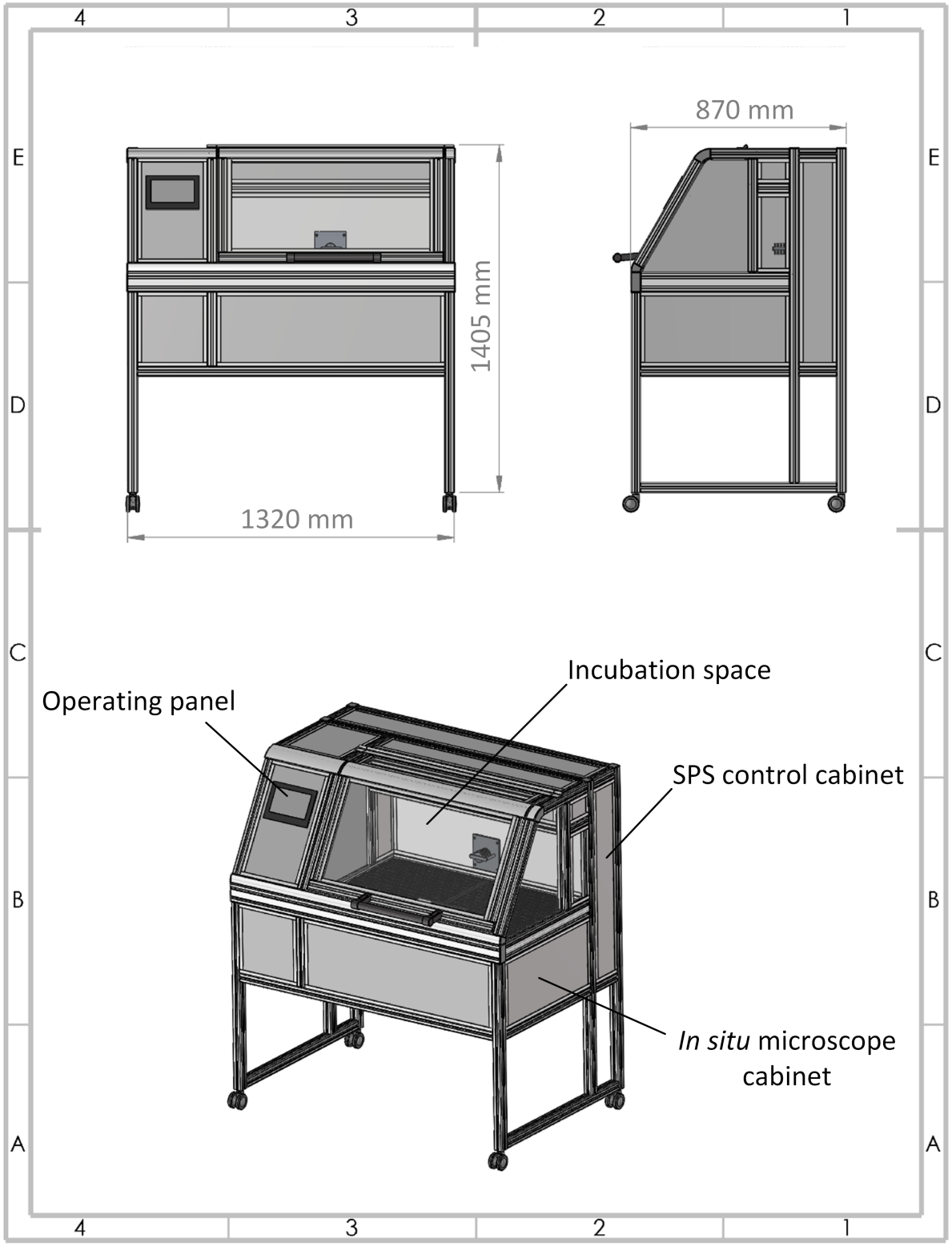

Figure 3.1: *Design drawing of a tailor-made incubator prototype for housing multiple small-scale stirred tank bioreactors for hiPSC suspension cultures. A custom-built in situ microscope unit is accommodated below the incubation cabinet to facilitate real-time imaging of hiPSC suspension cultures. Equipment for process data measurement and acquisition is located within the SPS control cabinet at the rear of the incubation space. Atmosphere composition and liquid handling is controlled via human machine interface operating panel.*

Monitoring of dissolved oxygen and pH in suspension bioreactors was accomplished by implementing hardware for optical sensor spot-based measurements (Presens). To achieve real-time imaging of hiPSC aggregation during suspension culture, a custom-built *in situ* microscope (fig. 3.4) was mounted in the lower cabinet beneath the incubation chamber. The microscope lens was extended into the incubation area and thereby allowed for image acquisition of hiPSC suspension samples. Further details on *in situ* microscope operation are provided in section 3.1.2 on page 43.

Figure 3.2: *A tailor-made incubator system was constructed to provide appropriate culture conditions for hiPSC suspension cultures. In addition, the incubator system contains all equipment necessary for automated process control and monitoring. Suspension culture vessels were placed freely within the incubated space (1). The incubator atmosphere, liquid-handling devices, stirrer agitation speed and data management was accessed via human machine interface (2). The process control equipment and sensor transmitters were located in the rear compartment of the incubator (3). The in situ imaging microscope was incorporated into the lower cabinet beneath the incubation area (4).*

The incubator was designed to operate up to three vessels of adjustable size simultaneously. Bioreactors were placed freely inside the incubation chamber and were subsequently connected to the available motor drives. In a similar fashion, dissolved oxygen transmitter cables were available for each CSTR in use. A schematic overview of the process control elements is provided in fig. 3.6. Device

operation was managed via human-machine interface (HMI) that was installed into the front panel of the incubator. The HMI was used to set the atmosphere temperature, CO_2 content, and peristaltic pump operation for *in situ* imaging. An at-line laptop computer was used to log pH and dissolved oxygen measurement data, set the motor speed for all bioreactors, and to store *in situ* microscope images.

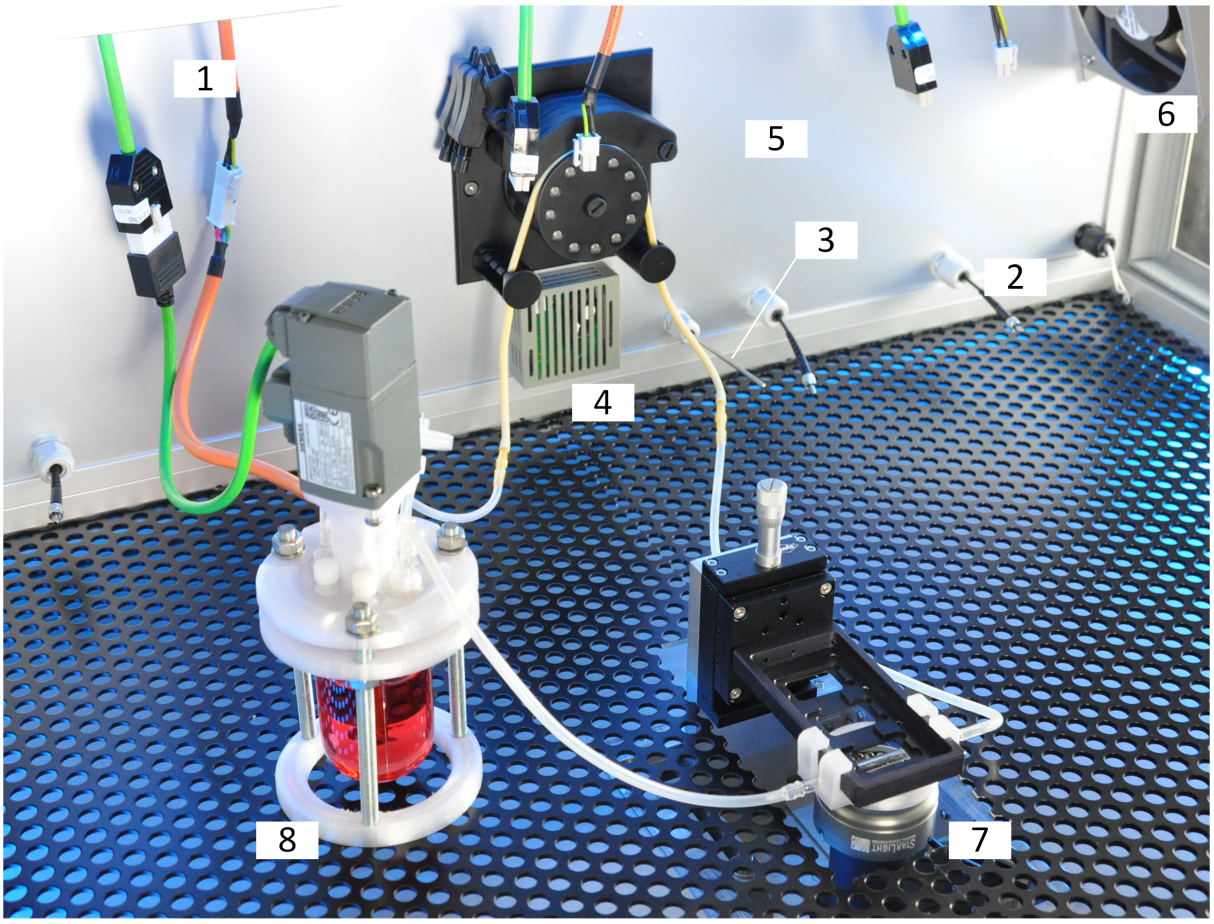

Figure 3.3: *The incubator was designed to operate multiple miniature stirred tank vessels in parallel. Therefore, motor power cables were available to run three reactors simultaneously (1). Equally, optical oxygen measurement and pH measurement was available for each bioreactor in operation (2). The incubator atmosphere was set to 37 °C and 5 % CO_2 with the aid of temperature (3) and CO_2 (4) sensors. The incubation chamber was tempered by heating foils attached to the rear panel of the incubator (5). Fans (6) to either side of the incubation compartment ensured constant air circulation. Online imaging of cell aggregates was achieved by passing a cell suspension sample from the reactors across an in situ microscope prototype (7). Stirred tank reactors (8) were placed freely inside the incubator.*

3.1.2 *In situ* microscope operation and image acquisition

The incubator prototype was equipped with a peristaltic pump that facilitated automated liquid handling. For *in situ* imaging, the pump was used to transport hiPSC cell suspension samples from CSTRs to the built-in *in situ* microscope for in-flow hiPSC aggregate monitoring. Therefore, manual sampling was omitted and reproducible data acquisition was possible by evading user-biased handling errors. Further, the use of *in situ* imaging minimized the risk of contamination during sample pipetting. The *in situ* microscope harnessed dark-field illumination to generate high contrast black/white images of hiPSC suspensions. The pre-manufacturing schematic is provided in figure 3.4.

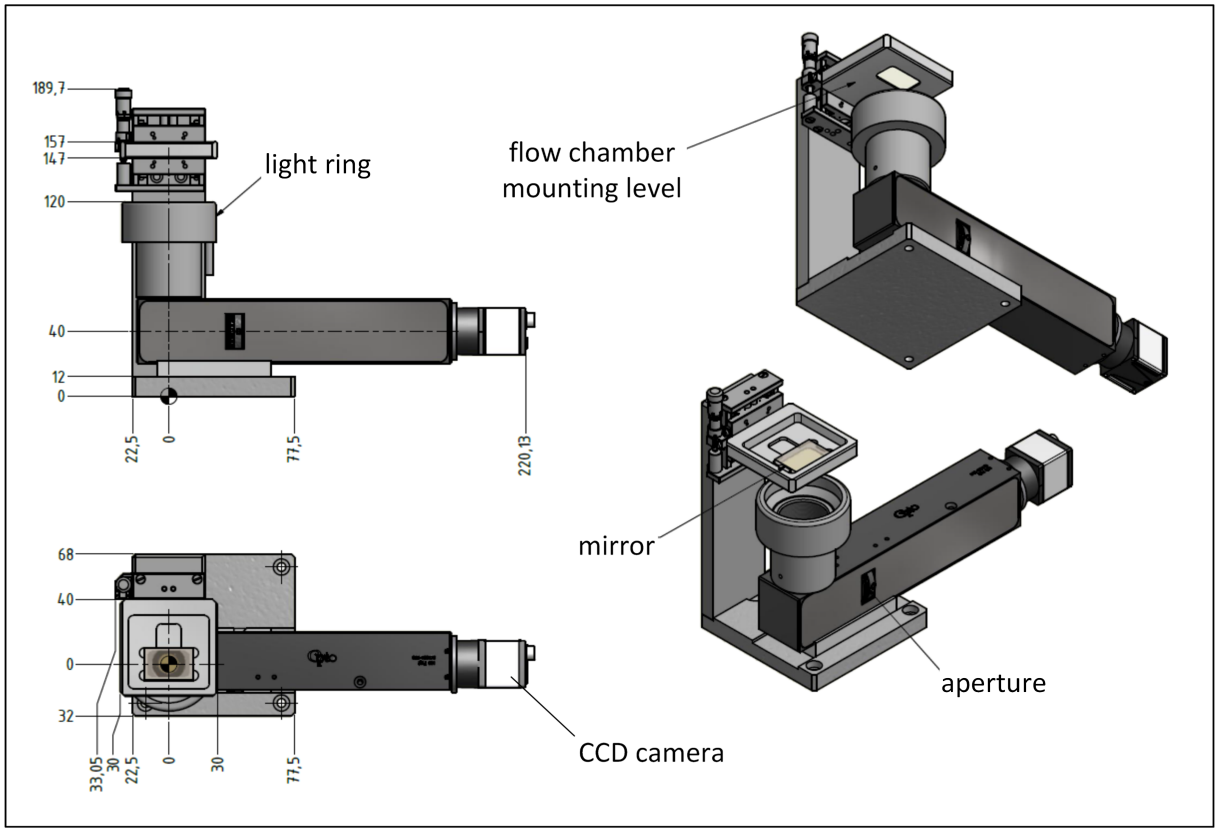

Figure 3.4: *Schematic of the incubator's built-in dark-field in situ imaging unit. During operation, the flow chamber was mounted between the mirror and the light ring. The light emitted by the LEDs passed through the flow chamber and was reflected by the mirror back towards the lens within the light ring center.*

To allow for in-flow bypass imaging, a flow chamber was placed between the flow chamber mounting level and the microscope lens. A glass tube with a flow channel width of 2 mm was found to be the most simple and, at the same time, the most suitable flow chamber design. The glass tube was held in place with a customizable, 3D-printed clamp (fig. 3.5).

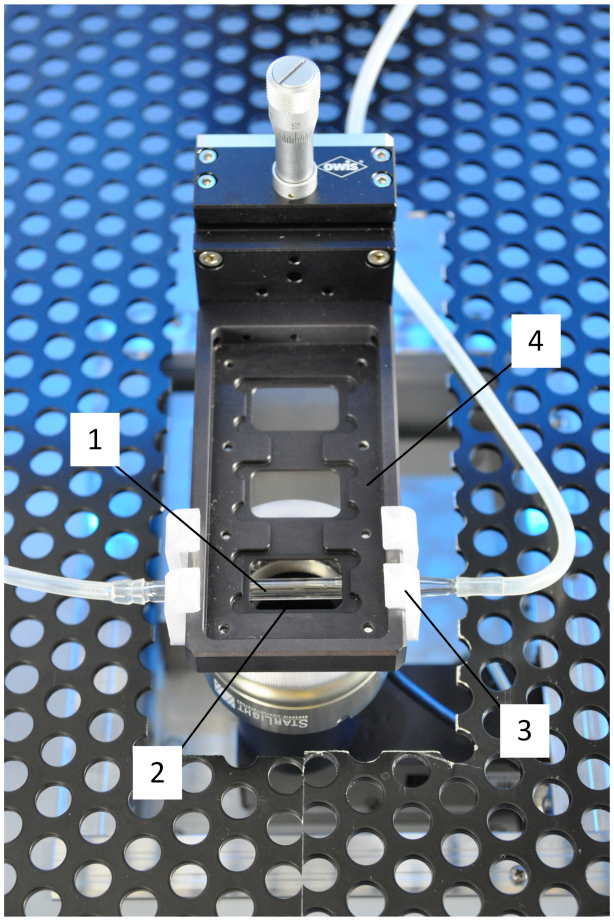

Figure 3.5: *Custom-built in situ microscope. The glass tube flow chamber (1) was positioned over the microscope lens (2) by a 3D-printed clamp (3). For depiction purposes, the mirror on top of the flow chamber mounting level (4) was removed.*

Sample illumination was provided by a light-emitting diode (LED) light ring that surrounded the microscope lens. The light was guided towards the flow chamber and passed through the sample. After, the light hit a mirror that was placed face-down on top of the flow chamber mounting level. The light was subsequently reflected and passed the sample a second time before entering the microscope lens. A charge-coupled device (CCD) sensor based-camera was used for image acquisition. For hiPSC suspension culture experiments, *in situ* imaging was performed for 2 min every 24 h at a sampling flow velocity in the range of 1.5 cm s^{-1}. To avoid cell massing inside the silicone hoses that were used for circulating cell suspensions, the flow direction of the pump was inverted in order to empty the hoses and transfer the sampled cell suspension back to the bulk of the bioreactors after each imaging session.

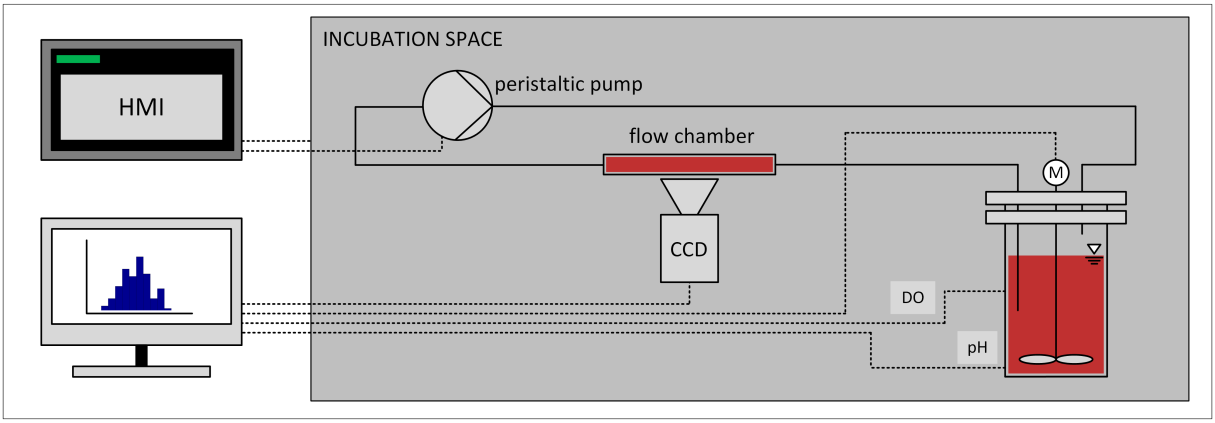

Figure 3.6: *Outline of the cell suspension bypass circulation for in situ imaging. Cell suspensions were sampled from bioreactors by a built-in peristaltic pump and lead through a flow chamber above the microscope lens. Images are acquired via CCD camera while cell suspensions were in flow. An at-line computer was used for image processing, stirrer speed control, and pH and oxygen measurement recording. The incubation atmosphere and pump settings were controlled via human-machine interface.*

3.2 Image processing

To obtain information on aggregate growth, image processing algorithms were developed to facilitate automated data extraction. The algorithms were tailored to the image format output of the custom-built *in situ* microscope and EVOS digital lab microscope, respectively. Algorithm programming was performed using a standard version of the open-source image processing package Fiji (ImageJ). The processing sequences for the generated algorithms are outlined in the figures below. Image analysis was performed in a batch-wise manner on every day of CSTR culture. Therefore, the images that were obtained during daily *in situ* imaging sessions were loaded into the algorithm and aggregate size distribution parameters were calculated for the specific stack of images. The corresponding ImageJ syntax is available in the supplementary section 5.1 and 5.2.

EVOS image processing sequence

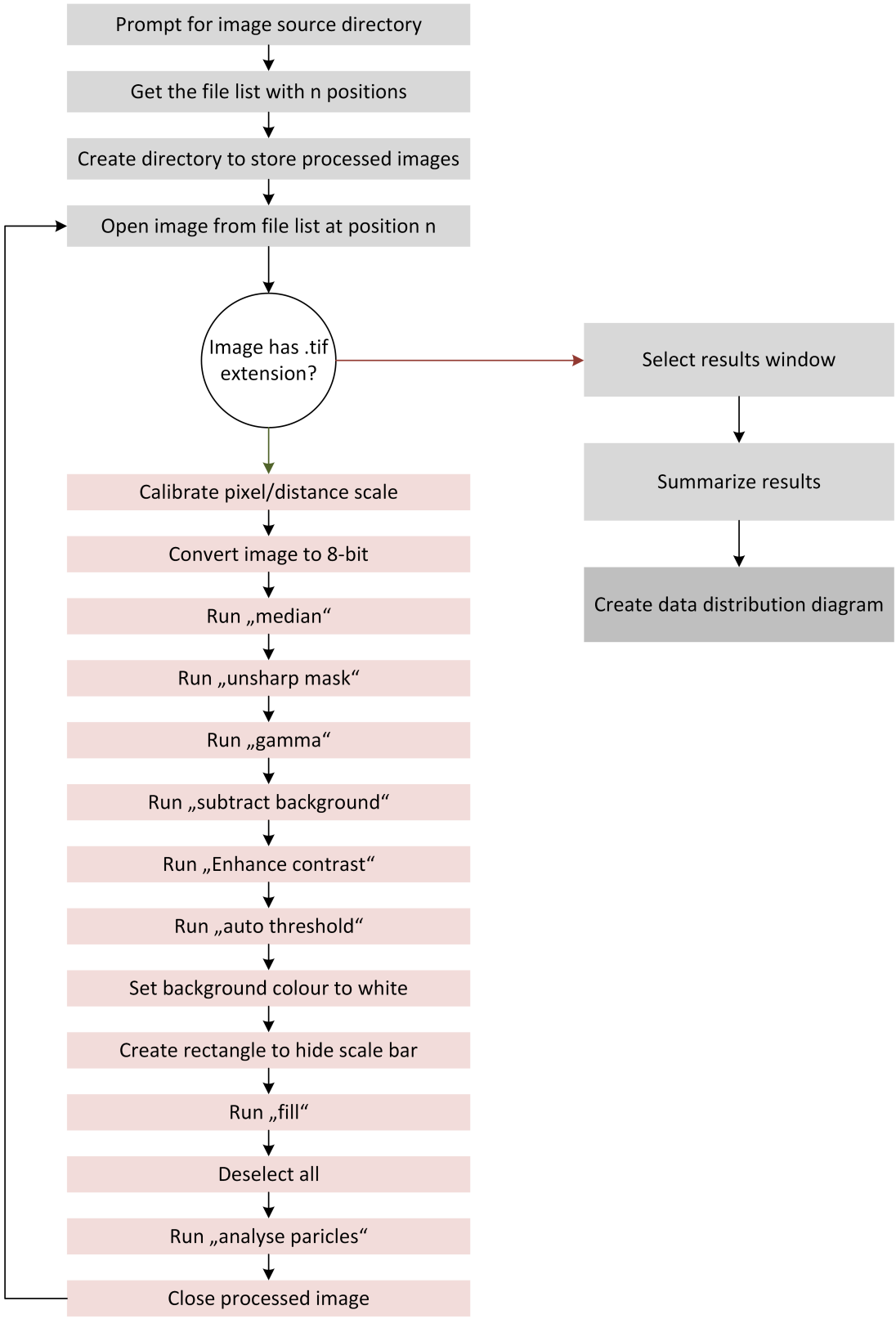

Figure 3.7: *Algorithm sequence used for processing of EVOS lab microscope images.*

***In situ* microscope image processing sequence**

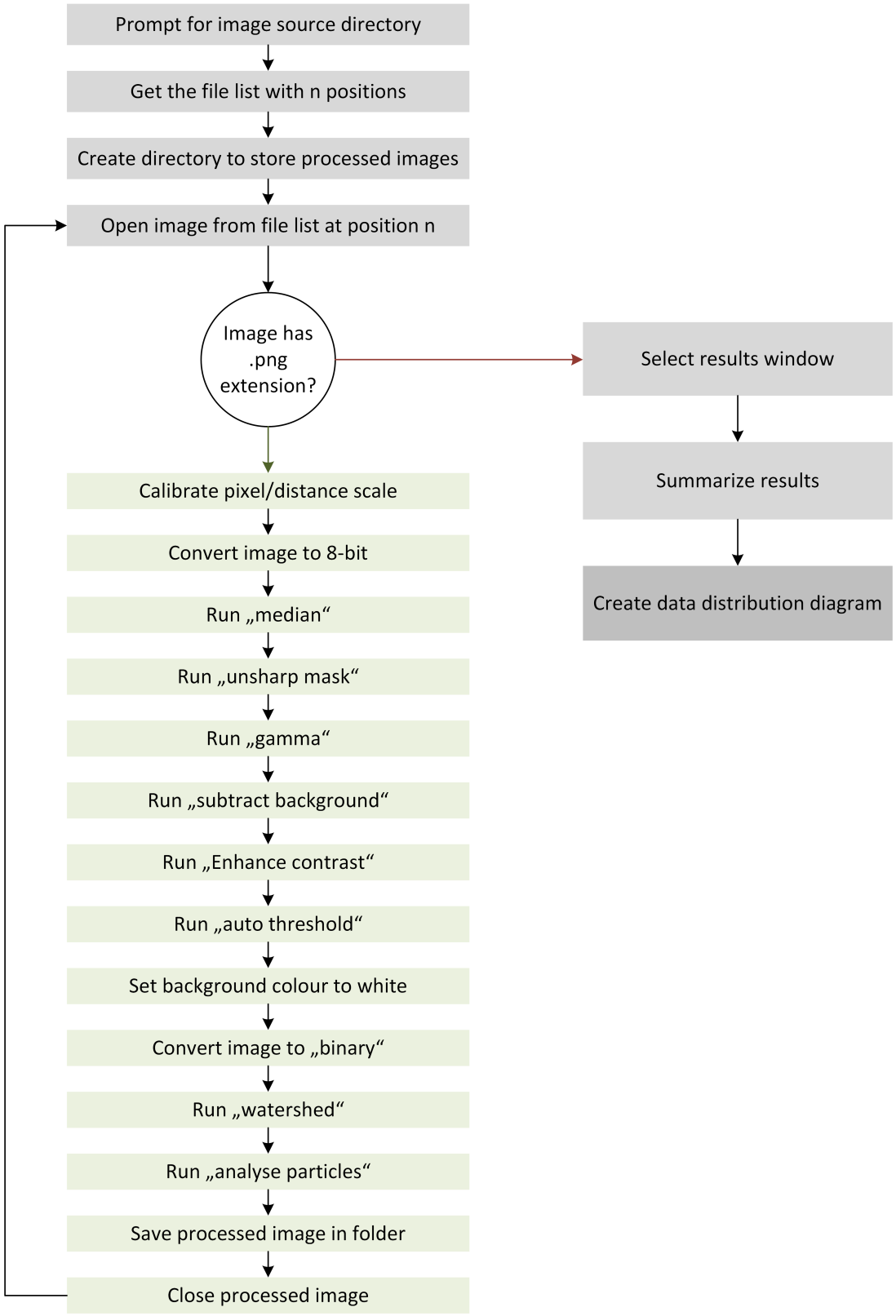

Figure 3.8: *Algorithm sequence used for processing of in situ microscope images.*

3.3 Custom-built stirred tank reactor development

3.3.1 Design aspects

The culture of suspended hiPSC aggregates differs in many ways from the culture of bacterial or mammalian single cell suspensions that are common in industrial applications. Due to their recognized sensitivity to shear stress, their characteristic tendency to rapidly form inseparable aggregate clusters on prolonged contact, and their distinctive sedimentation affinity represent challenges for the design of scalable suspension culture vessels. Since commercially available bench-top CSTR systems are commonly laid out for the culture of single cell bioprocesses, a tailored CSTR system that is specific for the culture of aggregating hiPSCs was developed. Therein, several considerations concerning the bioreactor geometry outline and subsequent manufacturing were addressed.

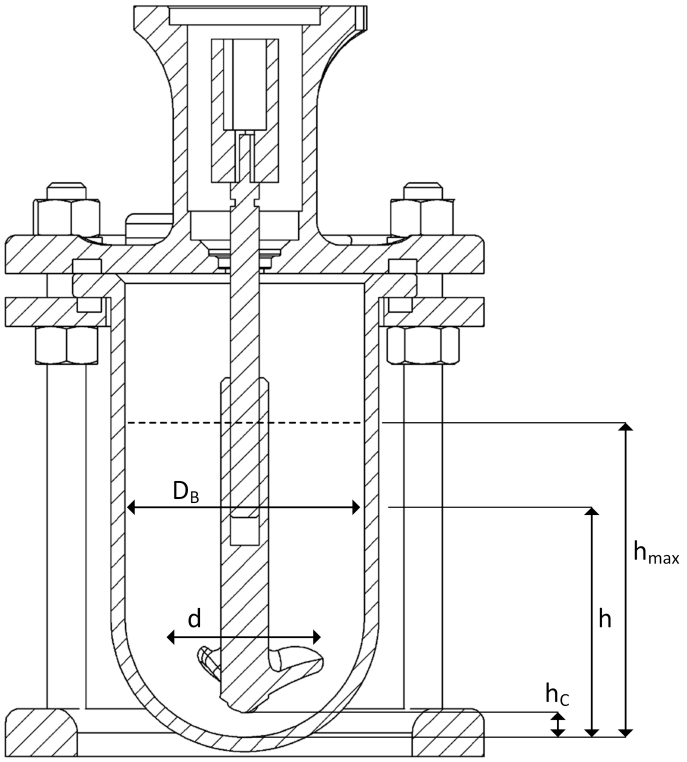

Figure 3.9: *Schematic description of bioreactor design aspect ratios. Bioreactor vessels were designed for operating hiPSC fed-batch suspension cultures starting from 65 ml (h) and ending with 86 ml (h_{max}). For maximum surface aeration, a slenderness ratio of $h/D_B = 1$ was chosen. For enhanced uplift flow, the stirrer diameter was set to $d = 2/3 D_B$ and positioned at clearance level $h_C = d/10$.*

The prime objective was to generate a culture vessel that would avoid massing and subsequent clumping of settled aggregates. Therefore, in a first step, a suitable vessel shape and stirrer design that would lead to pronounced uplift flow was identified to keep hiPSC aggregates suspended. In order to prevent aggregate sedimentation at the vessel bottom, the stirrer clearance was set to $h_C = d/10$

in order to minimize the dead zone beneath the stirrer's center point. The contact angles and shape of the stirrer wings was modified from a previously published design by Jirout and co-workers [58]. The overall stirrer diameter was set to $d = 2/3 D_B$. To enhance the pumping capacity of the stirrer, four baffles were installed to promote the formation of a vertical flow pattern. The corresponding baffle width was set to $w_b = D_B/10$. A round-bottom shape was chosen for the culture vessel to avoid local accumulation of hiPSC aggregates in the bottom corners of cylindrical vessels. The slenderness of the bioreactor vessel was defined $f_s = h/D_B = 1$. Considering the round-bottom shape of the culture vessel, the resulting working volume was $V_L = 62.5$ ml at the beginning of all fed-batch bioprocesses. A full model illustration of the bioreactor assembly is shown in fig. 3.10. The corresponding design aspect ratio details are summarized in tab. 3.1.

Table 3.1: *Bioreactor design aspect ratios*

filling height h	V_L/A	$5 \cdot 10^{-2}$ m
air/liquid interface A	$D_B^2 \pi/4$	$2 \cdot 10^{-3}$ m^2
slenderness f_s	h/D_B	1
max. slenderness $f_{s,max}$	h_{max}/D_B	4/3
stirrer diameter	d	$3.2 \cdot 10^{-2}$ m
stirrer/vessel diameter	d/D_B	2/3
stirrer clearance	h_C/d	0.1
baffle width w_b	$D_B/10$	$5 \cdot 10^{-3}$ m

During bioreactor manufacture, efforts were made to minimize the total number of components for easy bioreactor handling. The larger bioreactor components comprising the base plate, the glass holder ring, and the bioreactor lid, were subsequently produced from PLA by using an in-house fused deposition modeling 3D-printer (Leapfrog, Netherlands). The fabrication process of the required 3D-printed components for one bioreactor was accomplished within 4 h. The glass vessel was hand-crafted by a local glassblower (Glaspunkt, Germany). Customary thread rods were used to stack the glass holder ring and reactor lid. A shaft seal (Trelleborg, Sweden) was installed to shield the bioreactor interior from ambient contamination sources. To stabilize the rotating shaft, a ball bearing was placed above the shaft seal and secured by a shaft retainer. The shaft itself and the stirrer geometry were machined from stainless steel and PEEK, respectively (GT Labortechnik, Germany). Standard lab ware spatulas were manually trimmed and shaped to be used as baffles. To provide gas exchange, ports were installed in the lid component to allow for the placement of air filters via luer-lock connectors. In a similar fashion, rubber gaskets were customized to fit glass riser pipes for cell suspension liquid handling. Finally, optical sensor spots for pH and dissolved oxygen measurement were attached to the inside of the glass vessel.

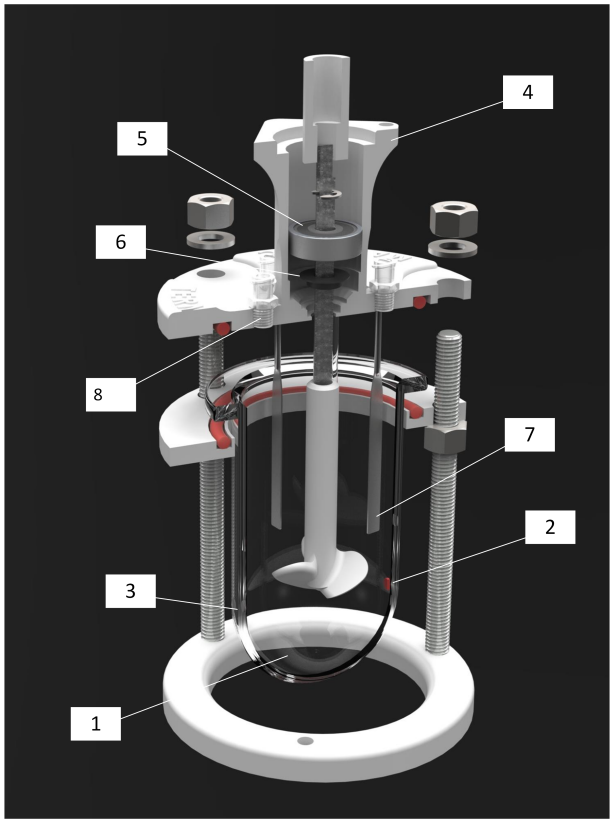

Figure 3.10: *Custom-made continuously stirred tank reactor. Most parts enclosing the culture glass vessel (1) were produced by in-house fused deposition modeling fabrication (3D-printing). All reactors were equipped with optical oxygen sensor spots (2) and pH sensor spots (3) that were attached to the inside of the glass wall. A motor was mounted onto the flange (4) to drive the stirrer. The rotating shaft is stabilized by a stainless steel ball-bearing (5). Sterile conditions inside the vessel were ensured by a shaft seal (6) that was placed below the ball-bearing. A total of four baffles (7) were installed to enhance the impeller pumping capacity. Luer-lock ports in the lid (8) provided head-space gas exchange with the surrounding atmosphere of the incubator through air filters and also allowed fluid removal and fluid addition by riser pipes.*

3.3.2 Fabrication material testing

Next to materials that are routinely used for bioreactor vessel construction in the biopharmaceutical and food production environment such as stainless steel (S/S) and PEEK, less costly materials comprising POM-C and PLA were tested for toxic effects caused by leaching on hiPSCs during culture. The cytotoxicity testing of PLA was of particular interest as it is a commonly used material in fused deposition modeling (3D-printing) applications. During suspension culture, the medium was in direct contact primarily with the CSTR stirrer and the glass vessel. Since glass is commonly considered inert and non-cytotoxic, it was not included in the material testing. The cell suspension was open to the inside of the bioreactor lid and thus was considered to be in indirect contact with the respective material. Therefore, material testings for S/S, PEEK, POM-C, and PLA were performed to investigate potential damping effects on hiPSC viability. The obtained data on cell viability after incubation in

material-contaminated culture medium is shown in fig. 3.11. All data was compared to positive control measurements of cells growing in standard mTeSR™3D medium. For negative control samples, hiPSC were cultured in 10 % of SDS. Additionally, control samples that were cultured in freshly prepared mTeSR™3D medium without the addition of 10 µM Y-27632 dihydrochloride were measured for cell viability to exclude the effect of Y-27632 dihydrochloride adhering to material surfaces and thus losing efficacy.

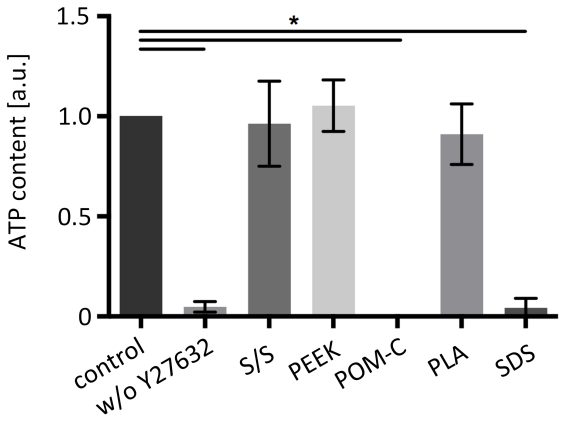

Figure 3.11: *Cytotoxicity testing of potential bioreactor construction materials. (n = 3, p < 0.05)*

As expected, cell viability was significantly decreased in hiPSC suspension samples that were cultured in either 10 % SDS and in mTeSR™3D medium without Y-27632 dihydrochloride supplementation, respectively. Equally predictable, medium incubated with S/S and PEEK showed no negative effect on cell viability. In the same manner, cell viability of hiPSC that were cultured in PLA-incubated medium showed no significant deviation from positive control samples. Interestingly, a significant drop of cell viability in hiPSC samples that were cultured in POM-C-incubated medium was observed.

3.4 CSTR engineering parameter characterization

The characterization of stirred bioreactors is vital in order to determine the engineering parameters that ultimately describe the bioprocess. Further, detailed knowledge of process parameters allows for straightforward bioprocesses to be transferred to greater or lower volume scales by keeping selected parameters constant. In this study, the majority of process engineering parameters were evaluated by establishing a computational model of the CSTR design that was used during hiPSC suspension culture experiments. When performing CFD simulations, a first step is to determine the fluid flow regime - laminar or turbulent - that applies for the selected fluid flow environment. Therefore, the Reynolds number N_{Re} was evaluated to characterize the flow regime according to eq. 1.1. The simulations that were established covered stirring velocities between 20 RPM and 120 RPM. For the calculation of the

respective N_{Re} values, the fluid dynamic properties of the stem cell culture medium mTeSR™1 were set to $\rho = 9.93 \cdot 10^2$ kg m^{-3} and $\mu = 7.65 \cdot 10^{-4}$ Pa s according to Appelt et al. [4]. With the stirrer diameter $D = 3.2 \cdot 10^{-2}$ m, the Reynolds numbers were calculated as $N_{Re,20\ RPM} \approx 440$ and $N_{Re,120\ RPM} \approx 2650$. In accordance with the information provided in section 1.5.1, a transient flow regime applies for stirring velocities between 20 and 120 RPM. Since a laminar flow regime could be excluded, a turbulent flow regime was assumed for all CFD simulations.

3.4.1 CFD model mesh refinement study

The accuracy of any computational fluid dynamics model largely depends on the applied mesh resolution. However, high resolution meshes come at the price of greatly increased computation effort, and as a result, extended computation times. Therefore, as part of the pre-processing, mesh refinement studies help to determine the appropriate mesh resolution that offers an acceptable compromise between the accuracy of the computation readout and the invested computation time. To establish a mesh refinement study, flow field simulations were performed for mixing at 120 RPM while varying the mesh resolution presets from “extra coarse” to “extra fine” as shown in fig. 3.12. In order to evaluate the model accuracy, the simulated maximum flow velocity at the stirrer wing tips was compared to the true value u_{max} derived from eq. 1.2.

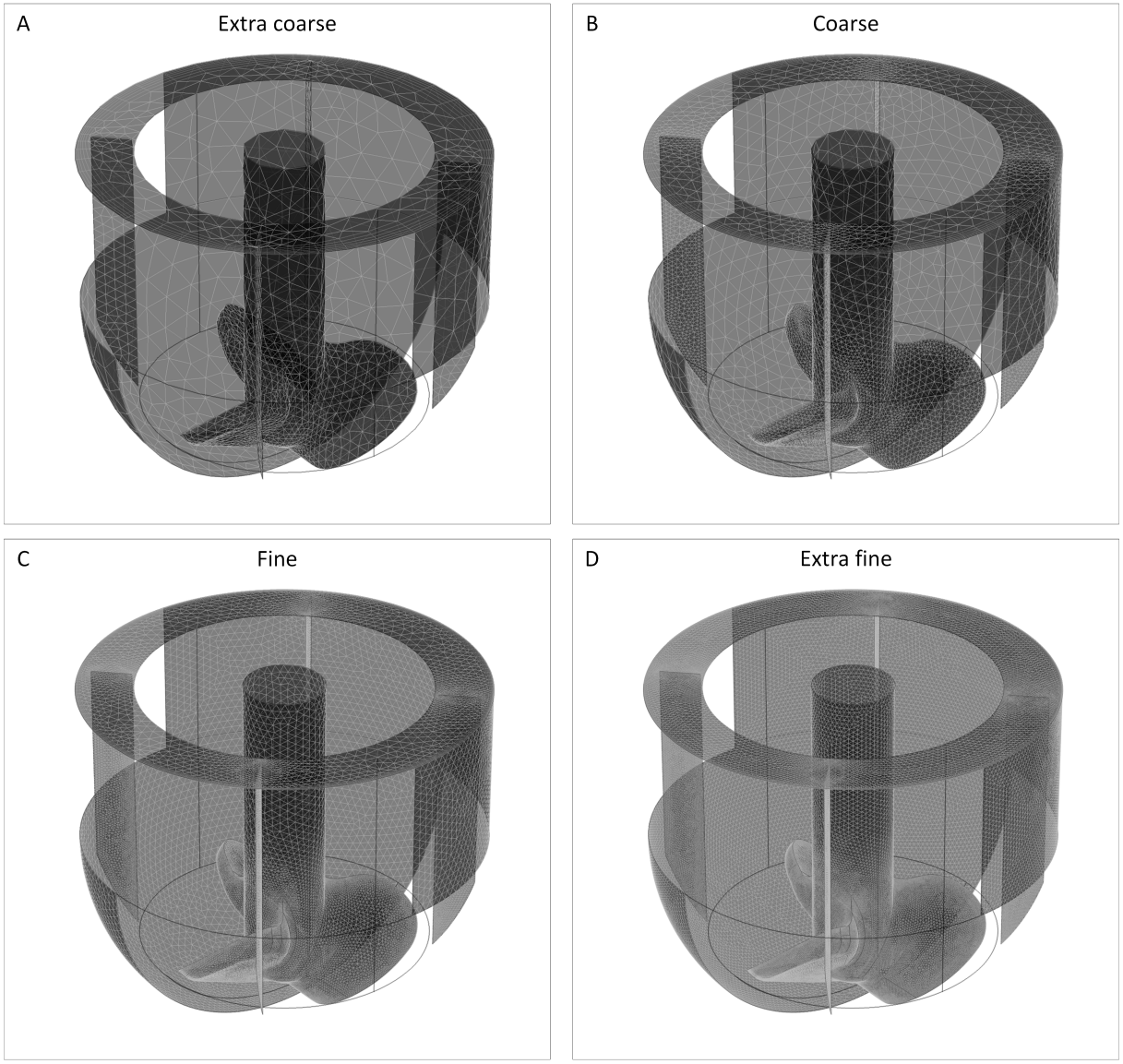

Figure 3.12: *Mesh refinement study. Meshes with extra coarse to extra fine* ***(A-D)*** *element size resolutions were applied to the model geometry and the accuracy of the computation outcomes was compared. The rotational speed of the stirrer domain was set to 120 RPM in all cases.*

With the stirrer radius of $r = 1.68 \cdot 10^{-2}$ m and the rotational velocity of $f = 120$ RPM, the maximum fluid velocity reference value of $u_{max} = 0.211$ m s^{-1} was calculated. The maximum flow velocities that were derived from flow simulations are presented in tab. 3.2. Additionally, details on the amount of mesh elements and the corresponding solution times that were required for the solving at the indicated mesh resolution are provided.

Table 3.2: *Mesh refinement study summary*

Mesh resolution	No. of elements	Solution time	Derived maximum fluid velocity	Deviation from real solution
extra coarse	$0.065 \cdot 10^6$	1 h 8 min	0.189 m s^{-1}	10.4 %
coarse	$0.620 \cdot 10^6$	4 h 22 min	0.201 m s^{-1}	4.7 %
fine	$3.37 \cdot 10^6$	24 h 42 min	0.219 m s^{-1}	3.8 %
extra fine	$18.6 \cdot 10^6$	144 h 4 min	0.217 m s^{-1}	3.1 %

For the lowest mesh resolution, the fluid computation was achieved within approximately one hour. The derived maximum fluid velocity was found to deviate from the real solution of $u_{max} = 0.211$ m s^{-1} by 10.4 %. For increased mesh resolutions, the computation time increased considerably due to the increasing number of mesh elements. For the "coarse" mesh resolution, the flow field simulation was obtained after around 4.5 h and provided a deviation of 4.7 % from the real maximum fluid velocity. For "fine" and "extra fine" mesh resolutions, the computation time escalated to approximately 24 h and 144 h, respectively. The derived maximum fluid velocity values diverged from the true value by 3.8 % and 3.1 %.

3.4.2 Stirrer pumping capacity

The effect of baffling was investigated by computing the flow velocity field for baffled and unbaffled CSTR setups. With the aim of generating sufficient uplift flow to prevent aggregate sedimentation, the focus of the investigation was on the velocity field in the positive z-direction. The resulting flow field magnitude for the investigated CSTR setups is depicted in fig. 3.13 and indicated by color range. For both cases, the agitation velocity was set to 75 RPM. The computations revealed homogenous z-directional flow velocity magnitudes in the range of $2.75 \cdot 10^{-3}$ m s^{-1} for unbaffled mixing (fig. 3.13 A). Further on, swirl flow was detected as denoted by arrows (fig. 3.13 B).

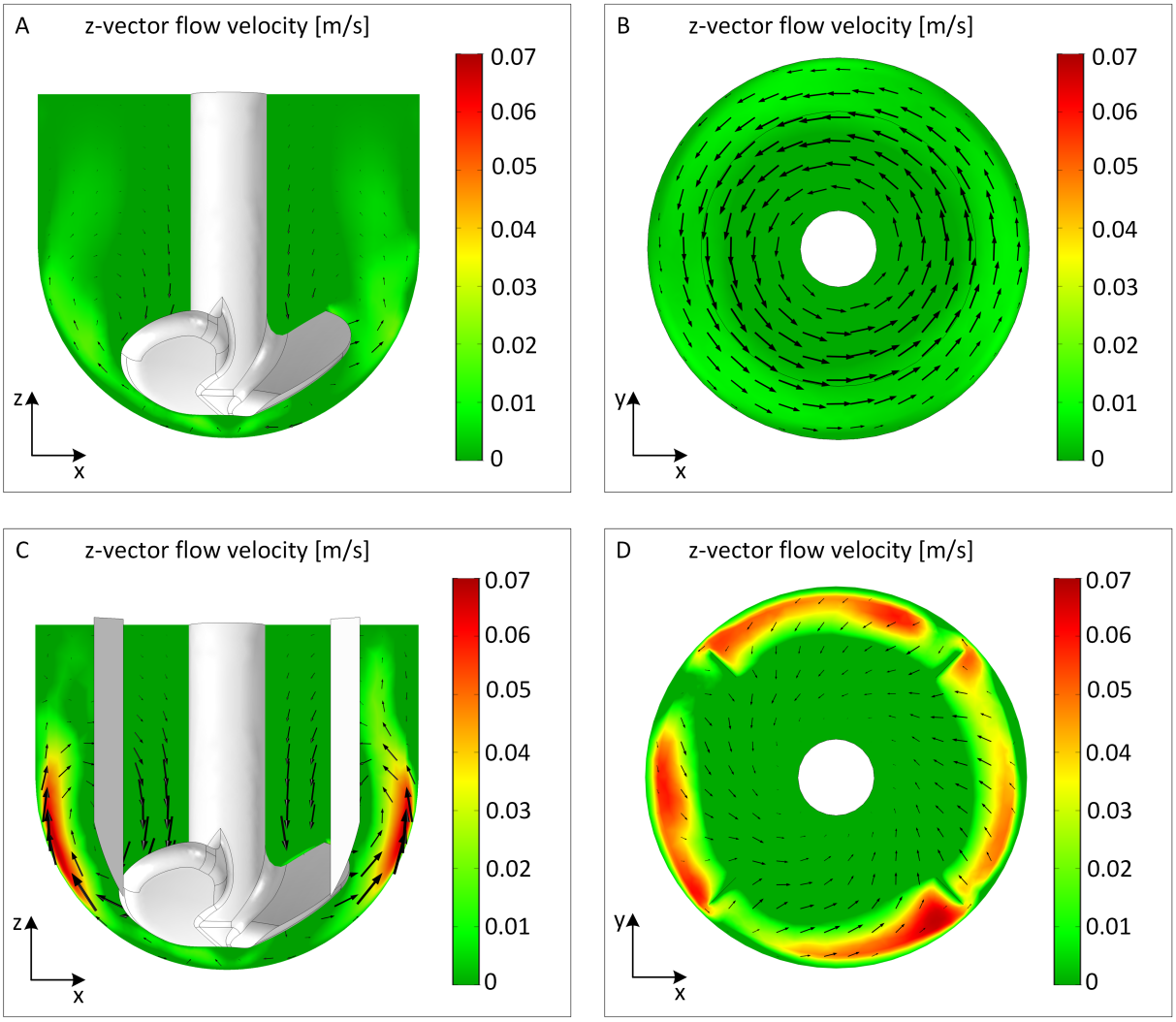

Figure 3.13: *Computational fluid dynamics-based comparison of the fluid flow pattern in baffled and unbaffled bioreactor setups promoted by stirring at 75 RPM.* ***(A)*** *The calculated flow field in unbaffled bioreactors revealed a uniform velocity distribution in the xz-plane.* ***(B)*** *Swirl flow was detected in the xy-plane.* ***(C)*** *The use of baffles lead to inhomogeneous flow velocities in the xz-plane.* ***(D)*** *Simultaneously, the formation of turbulences in the xy-plane was observed. Black arrows indicate direction of flow. The arrow length is proportional to the fluid flow velocity in the xz-plane and is synchronized among subfigures. The velocity magnitude in the positive z-vector direction is indicated by color range and is synchronized between both baffled and unbaffled mixing setups.*

On the other hand, swirl flow was suppressed in the baffled flow regime (fig. 3.13 D). Instead of swirl, the fluid was redirected in the z-direction, which is indicated by elevated z-flow velocity magnitudes at the vessel walls (fig. 3.13 C and D). In average, a z-directional flow magnitude of $9.3 \cdot 10^{-3}$ m s^{-1} was obtained for the baffled CSTR setup.

3.4.3 Shear stress estimation

For an accurate shear stress evaluation, viscous and turbulent effects that contribute to the total shear stress during mixing were considered according to eq. 2.1 on page 34. The shear stress pattern presented in fig. 3.14 was generated by stirring at 75 RPM. As indicated by color range, an average shear stress of $4.5 \cdot 10^{-2}$ Pa was derived. In addition, shear stress peak levels of $1.4 \cdot 10^{-1}$ Pa were calculated for regions that were characterized by considerable flow velocity gradients.

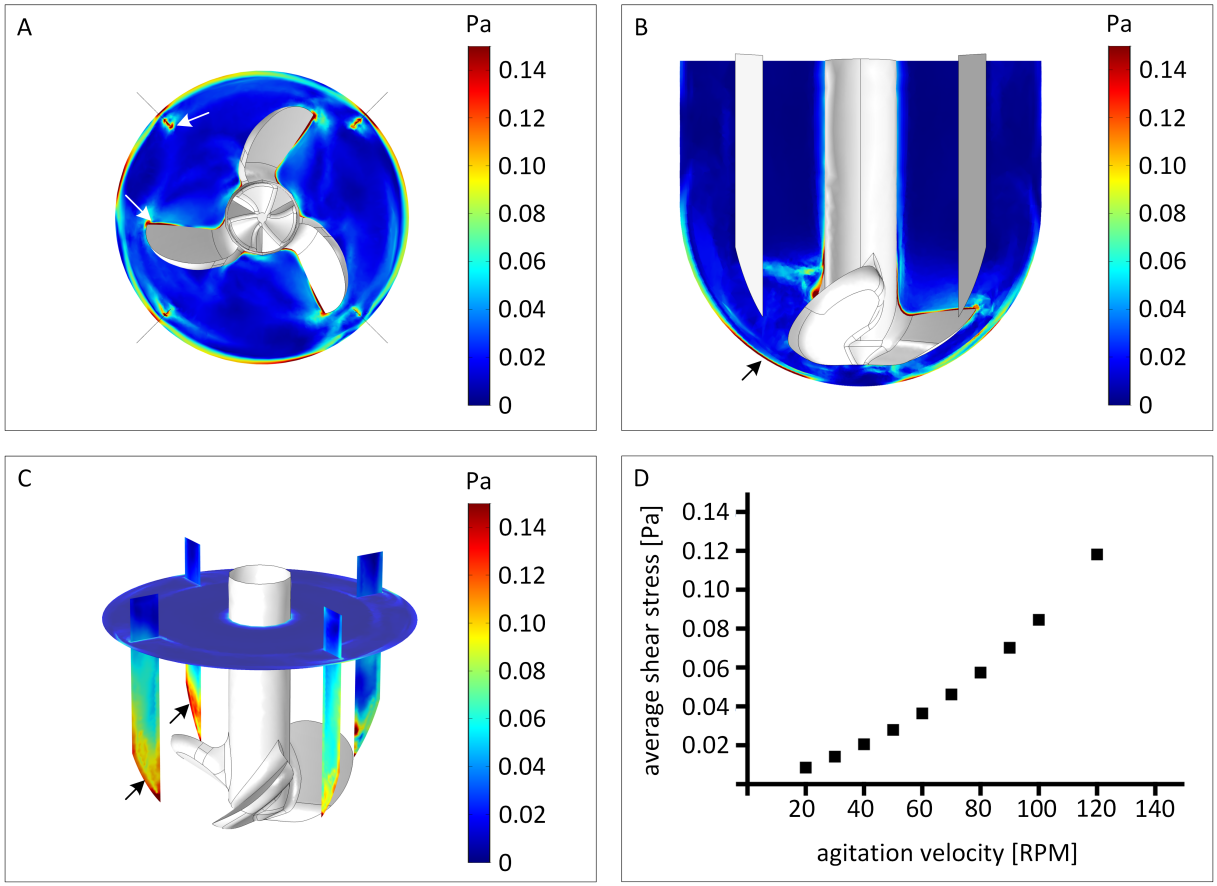

Figure 3.14: *Shear stress estimation by fluid dynamics simulations.* ***(A-C)*** *Shear stress pattern caused by stirring at 75 RPM. Elevated shear stress was generated at the stirrer wing tips and close to the baffle surfaces.* ***(D)*** *Occurring average shear stress as a function of the stirring speed.*

For instance, elevated shear stress levels were calculated for fast moving stirrer sections, e.g. the wing tips (fig. 3.14 A, white arrows). Further flow velocity gradients occurred at the glass vessel bottom where the fluid was accelerated in the upward direction (fig. 3.14 B, black arrow), and at the baffle surfaces (fig. 3.14 C, black arrows). In contrast, low shear stress in the range of $5 \cdot 10^{-3}$ Pa was calculated for less troubled fluid sections, which made up the larger part of the bulk fluid. To obtain information on the shear stress magnitude development, further simulations were performed and the average shearing was calculated for a range of stirring speeds (fig. 3.14 D). Here, a non-linear progression of the average shear stress was obtained for the investigated stirrer speed range.

3.4.4 Newton power number and specific power input

The dimensionless Newton power number N_P is one of the key characteristics of stirred bioreactors. To determine the Newton power number, CFD simulations were performed to estimate the power draw that is inflicted on the stirrer drive performance by the inertia of the bulk fluid mass. Based on the derived *in silico* data, the power number was computed for a range of stirring velocities for baffled and unbaffled mixing setups as shown in fig. 3.15. In accordance with common practice, the Newton power number N_P was plotted over the Reynolds number N_{Re}.

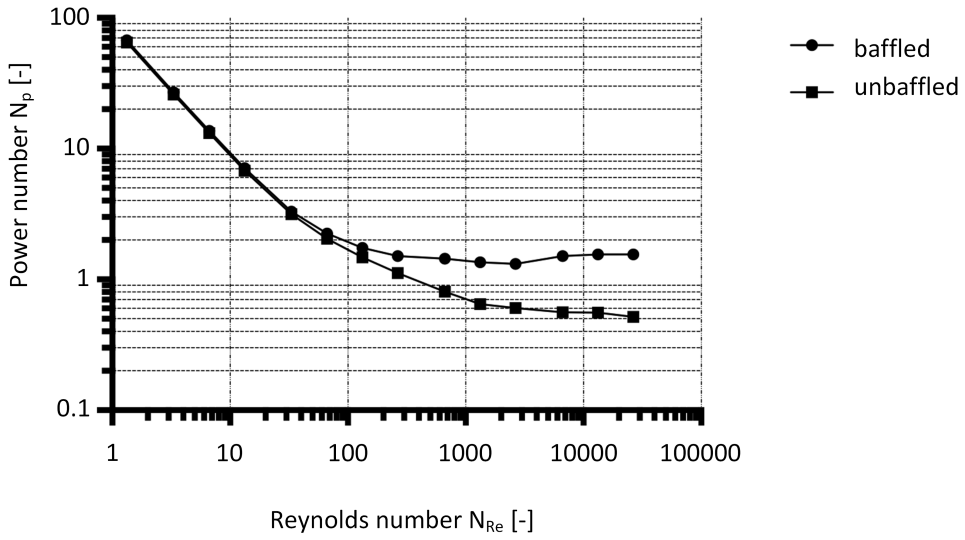

Figure 3.15: *Computational fluid dynamics-derived power curves for baffled and unbaffled mixing.*

The resulting Newton power number curves started at approximately $N_{P,Re<2}$ = 60 for baffled and unbaffled mixing. A linear decline of both Newton power number progressions down to a value of N_P = 9 was obtained for the laminar range 2 < N_{Re} < 10. After, the Newton power number for unbaffled mixing reached a steady-state value of $N_{P,unbaffled}$ = 0.55 for N_{Re} > 5000. In contrast, the baffled agitation setup was characterized by a considerably higher stationary Newton power number of $N_{P,baffled}$ = 1.6. Since CSTR experiments were performed at 75 RPM, a Reynolds number of $N_{Re} \approx 1650$ was derived according to eq. 1.1. By using the CFD-derived power curve for baffled mixing from fig. 3.15, a corresponding Newton power number of $N_{P,Re=1650}$ = 1.5 was obtained. Following, the calculation of the specific power input was possible. According to equation 1.3, a volume-specific power input of P/V_L = 1.32 W m^{-3} was calculated for baffled mixing at 75 RPM.

3.4.5 Mixing time

Manual mixing time measurements

The mixing time was visually determined for increasing stirrer speeds for baffled and unbaffled bioreactor setups. Therefore, the bulk fluid was stained by injecting a phenol red solution to the bioreactor during agitation. Shortly after the injection, a two-phased spreading of the injected dye was visually detectable as shown in fig. 3.16. Although the phenol red solution was injected through one of the ports in the bioreactor lid, the spreading of the dye was observed to progress significantly faster in the lower section of the bioreactor close to the stirrer wings. The agitation was maintained until the dye was evenly dissolved in the bulk fluid. For slow mixing at 20 RPM, a time span of approximately 52 s was necessary to achieve homogenous spreading of the phenol red dye. At higher mixing speed, the blending times decreased as outlined in figure 3.17.

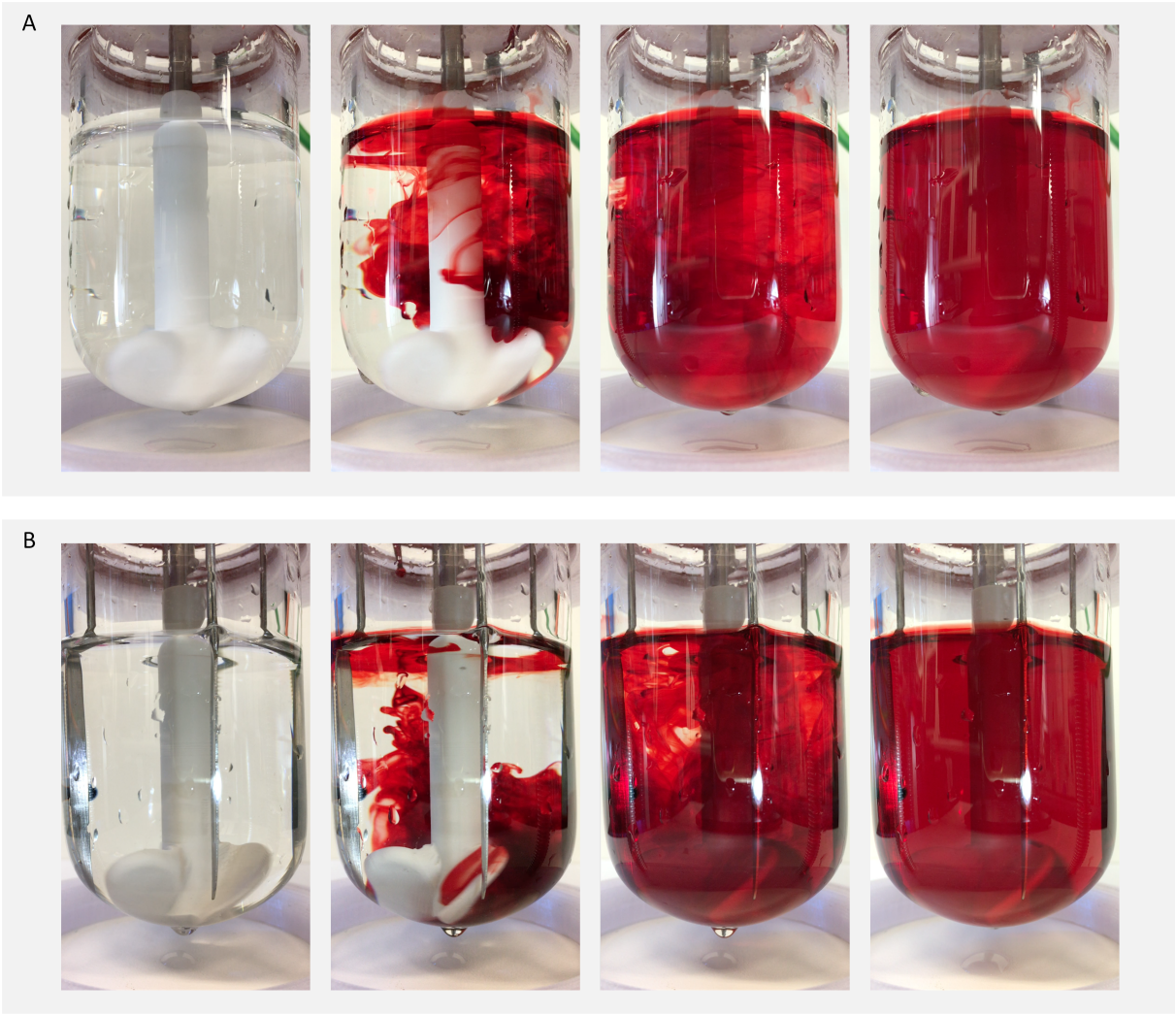

Figure 3.16: *Visual determination of bioreactor mixing times through dye injection for* ***(A)*** *unbaffled and* ***(B)*** *baffled bioreactor configurations.*

Interestingly, the impact of the stirring speed on the mixing time lessened when stirring at 60 RPM or higher. From there on, mixing times in the range of 16 s were observed for stirring velocities between 60 RPM and 120 RPM. Another observation showed that the mixing times did not vary significantly between the baffled and unbaffled bioreactor configuration.

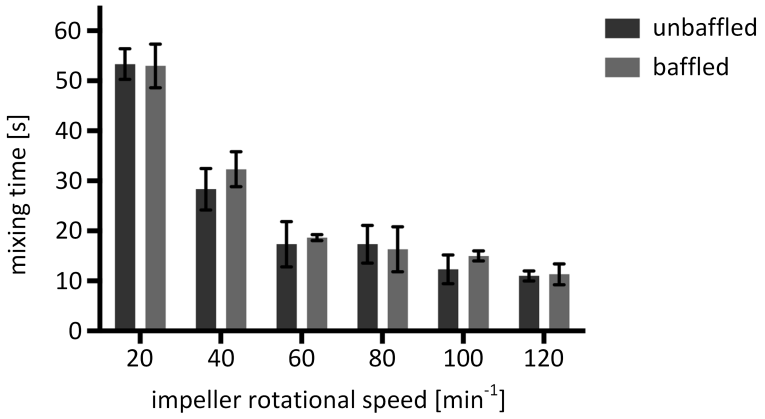

Figure 3.17: *Mixing times in baffled and unbaffled bioreactors.* ($n = 3,\ p < 0.05$)

CFD-derived mixing time

In order to evaluate the overall robustness and accuracy of the computational model, the mixing time was simulated for the same stirrer speed range with the aim to compare the *in silico* read-out to manual measurements. Since the results that were obtained from phenol red stainings indicated no significant variation between baffled and unbaffled mixing setups, the CFD-mixing time simulations were restricted to the baffled agitation setup.

CFD-mixing times were obtained by performing time-dependent mixing studies. A tracer substance injection was modeled by defining a point mass source as shown in fig. 2.3. The progression of the tracer concentration was subsequently computed for a time span of 60 s for each stirring speed. The tracer concentration was monitored for multiple probes of a defined point array (fig. 2.4). For each measurement probe, the tracer substance concentration was plotted over the mixing time. The time points for 90 % and 95 % of mixing completion were obtained by defining confidence intervals as shown in fig. 3.18. The final concentration of the tracer substance was set to $c_{tracer,t\to\infty} = 1$ mol m^{-3}.

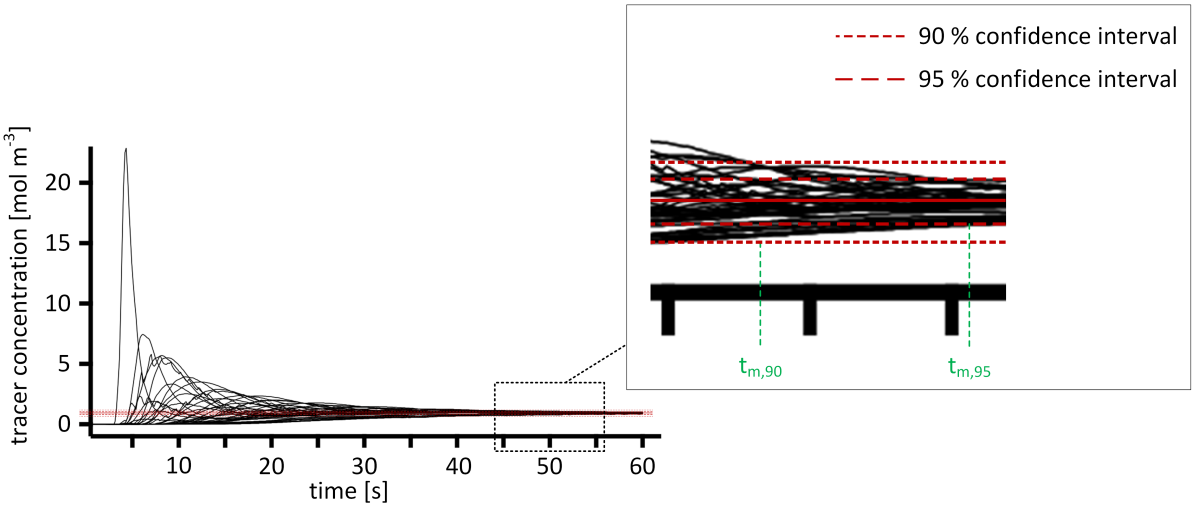

Figure 3.18: *CFD-derived mixing time estimation in baffled bioreactor setups. A point matrix was used to track the concentration of a tracer substance at homogeneously distributed points across the bioreactor fluid over time. The tracer substance injection was initiated at time point* $t_{inject} = 3$ *s. The resulting array of concentration curves converged towards the final concentration of* $1\ mol\ m^{-3}$*. Intervals of confidence were defined and the corresponding time points* $t_{m,90}$ *and* $t_{m,95}$ *indicated 90 % and 95 % mixing process completion.*

The progression of the tracer concentration distribution for a stirring speed range covering 20 - 120 RPM is provided in fig. 3.19. The array of curves for each stirring velocity was characterized by peak concentrations in the range of $15 - 20$ mol m^{-3} shortly after tracer injection for all stirring speeds. The convergence behavior, however, was observed to vary between stirring scenarios. For stirring speeds in the lower segment of 20 RPM and 40 RPM, the convergence towards the final concentration appeared stagnantly compared to higher stirring speeds. Here, a mixing completion of 90 % was reached at time points $t = 48$ s and $t = 33$ s. Convergence at higher stirrer settings was observed to occur more timely. For instance, 90 % convergence was reached at $t = 22.5$ s for a simulated stirring regime of 60 RPM and $t = 18.75$ s for 80 RPM. Even more intense stirring resulted in computed mixing times of $t = 17.25$ s and $t = 14.7$ s for 100 RPM and 120 RPM, respectively. A detailed resume of the obtained mixing times for 90 % and 95 % mixing completion is provided in tab. 3.3.

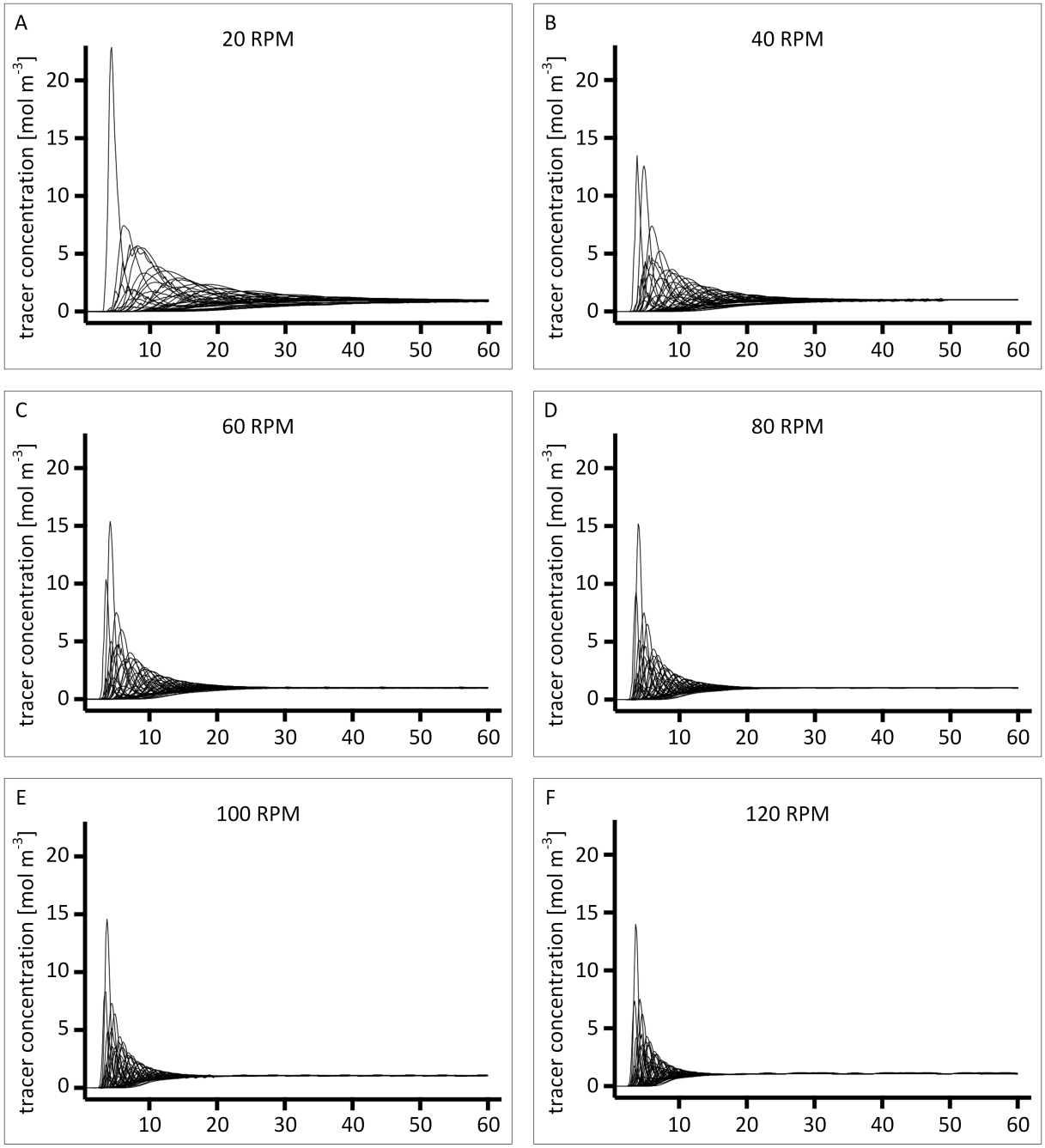

Figure 3.19: *Tracer concentration curves for increasing mixing speed. The concentration of a tracer substance was mathematically modeled for an array of evenly distributed measurement points in the bioreactor fluid domain during agitation of the bulk fluid. Each curve within an array represents one measurement point.* ***(A-F)*** *Time-dependent tracer concentration progressions were compute for a total mixing time of 60 s (x-axis) at increasing agitation velocities in steps of 20 RPM.*

Table 3.3: *Mixing times derived from computational fluid dynamics simulations.*

Stirrer speed (RPM)	Mixing time (s) 90 % confidence interval	Mixing time (s) 95 % confidence interval
20	48.45	54.6
40	33.6	37.5
60	22.5	26.25
80	18.75	21.75
100	17.25	19.95
120	14.7	16.5

Comparison of measurement data and simulated mixing times

Following CFD modeling of the 90 % and 95 % mixing confidence interval, the obtained data sets were compared to phenol red injection measurements. The corresponding mixing times were plotted for the investigated stirring speed range of 20 RPM - 120 RPM. Matching of CFD data and manual measurements delivered a non-linear mixing time decline with increasing stirring speed. With few exceptions, the manually measured time points did not vary significantly from CFD-derived mixing times. For a stirring speed of 60 RPM, the simulated mixing time for both 90 % and 95 % mixing completion were significantly longer compared to the manual measurement. Similarly, the time point for 95 % mixing completion at 100 RPM varied from the manual measurement to a significant extent.

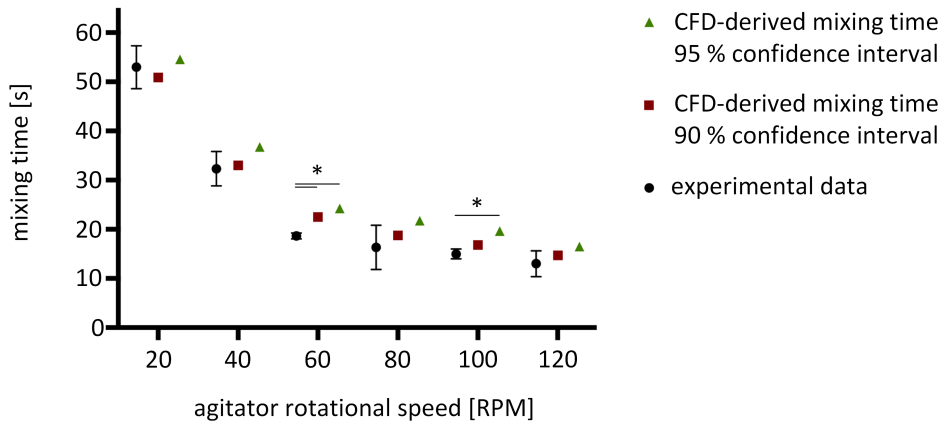

Figure 3.20: *Comparison of manual and CFD-derived bioreactor mixing times for baffled mixing. Manual measurements were obtained from phenol red staining of the bioreactor bulk fluid for a range of mixing speeds. The data was matched versus mixing times derived from computational fluid dynamics simulations at 90 % and 95 % mixing completion. ($n = 3$, $p < 0.05$ for manual measurements)*

3.5 Suspension culture of hiPSC

3.5.1 Evaluation of hiPSC seeding densities

Prior to CSTR experiments, a range of seeding concentrations were tested at 1 ml well plate format (fig. 3.21). With the aim to identify a suitable seeding density that results in optimal medium usage at small-scale, cell concentrations from $1 \cdot 10^5$ cells ml^{-1} to $10 \cdot 10^5$ cells ml^{-1} were evaluated. For all seeding concentrations, the consumption of glucose was determined as read-out parameter. Therefore, glucose concentrations were measured every 24 h for each sample as described in section 2.2.7. The measurements were performed for the duration of one cell passaging cycle.

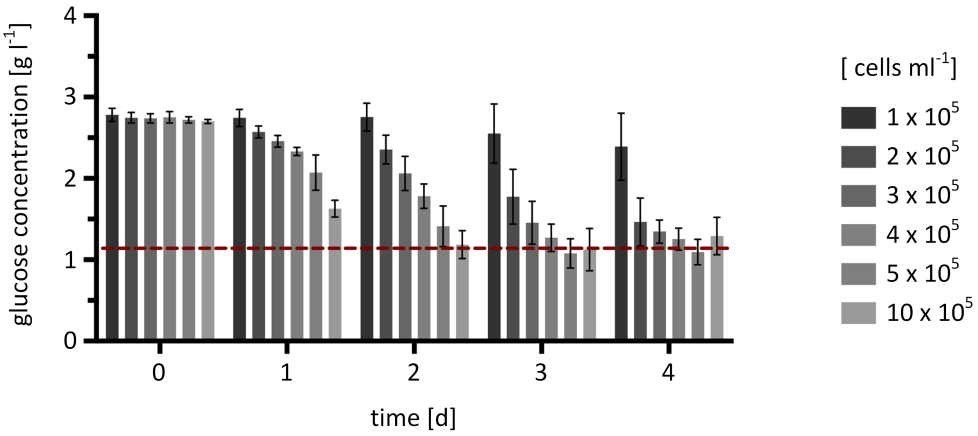

Figure 3.21: *Glucose concentration in hiPSC 1 ml cultures at increasing cell seeding densities. The concentration of glucose reached a plateau independently of the seeding concentration (red slashed line). (n = 3)*

The initial glucose concentration at the beginning of the suspension culture was stable at approximately 2.8 g l^{-1} for all seeding concentrations. On day 1, variations between the investigated cultures were observed and progressively lower glucose concentrations were measured for samples that were inoculated with increasing cell densities. In particular, the highest seeding density plateaued at 1.1 g l^{-1} (slashed red line in fig. 3.21) on day 2. On day 3, well plate suspension cultures that were inoculated with $4 \cdot 10^5$ cells ml^{-1} and higher also reached the plateau concentration. Eventually, all but the two lowest seeding densities were observed to stagnate at 1.1 g l^{-1}. Conclusively, the obtained data provided a first impression of media consumption for a range of seeding densities for static cultures at a small-scale. More importantly, the information obtained served as starting point to evaluate a suitable CSTR seeding density. In this regard, a seeding density of $3.5 \cdot 10^5$ cells ml^{-1} was chosen for subsequent CSTR experiments.

3.5.2 Peristaltic pump-induced liquid handling allows for safe transport of hiPSC suspensions

Lactate dehydrogenase (LDH) is an oxidoreductase enzyme that is, when secreted by cells, commonly associated to cell damage and loss of cell viability. Since any liquid handling device induces shear forces on the transported liquid, a close investigation of pump-induced cell stress was performed prior to CSTR experiments. Therefore, 20 ml static hiPSC suspension cultures were inoculated as described in section 2.2.3 and maintained for 4 days. Every 24 h, the cell suspensions were circulated as shown in fig. 3.6 and LDH levels were measured from 200 µl samples. On the last day of culture, cells were harvested and viability was measured by automated nucleo-staining as described in section 2.2.3.

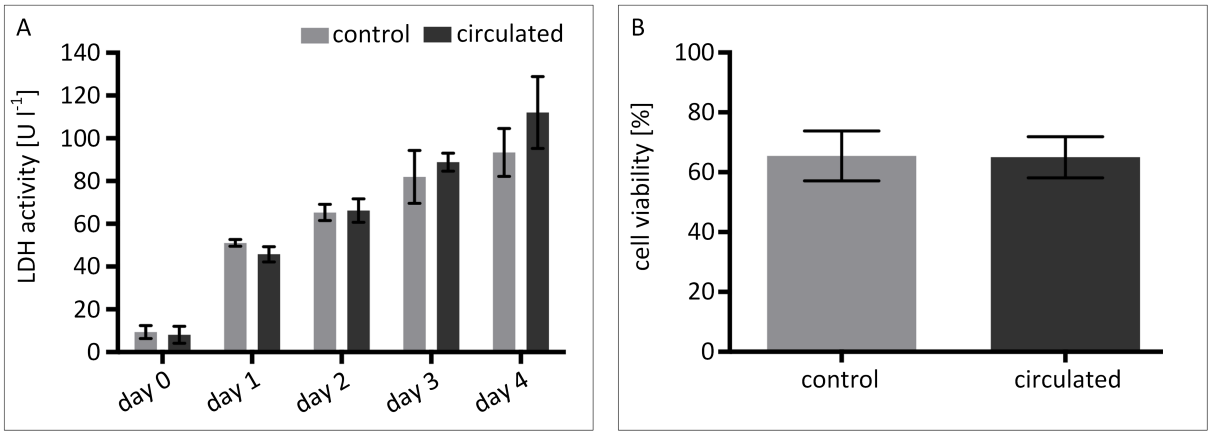

Figure 3.22: *Suspension culture samples were investigated for lactate dehydroxynase (LDH) activity* ***(A)*** *and cell viability* ***(B)*** *to convey potential cell damage caused by the peristaltic pump during circulation. (n = 3, p < 0.05)*

Measurements of LDH levels revealed increasing enzyme activity over the culture duration in both circulated and control suspension culture. Shortly after inoculation, LDH levels of approximately 15 U l^{-1}were detected, and signals increased to peak levels in the order of 105 U l^{-1} on day 4. Statistical analysis indicated no variation between circulated and control suspension cultures at all times (fig. 3.22 A). The assessment of the cell viability showed that the amount of viable cells had dropped to about 65 % in both circulated and control suspension cultures on the final day of the experiment. Similarly to LDH activity data, no significant difference was detected (fig. 3.22 B), indicating that the peristaltic pump was fit for cell suspension handling.

3.5.3 *In situ* imaging facilitates real-time monitoring of hiPSC aggregation during suspension culture

The formation of hiPSC aggregates in CSTR suspension cultures was tracked by the custom-built *in situ* microscope located at the center of the incubator. To transfer cell suspension samples to the microscope, a liquid handling bypass was connected to each CSTR in operation. During cell suspension circulation, a total of 40 images were taken and delivered approximately 2000 aggregate counts per measurement within 2 min. Imaging procedures were carried out every 24 h. An example image is provided in fig. 3.23.

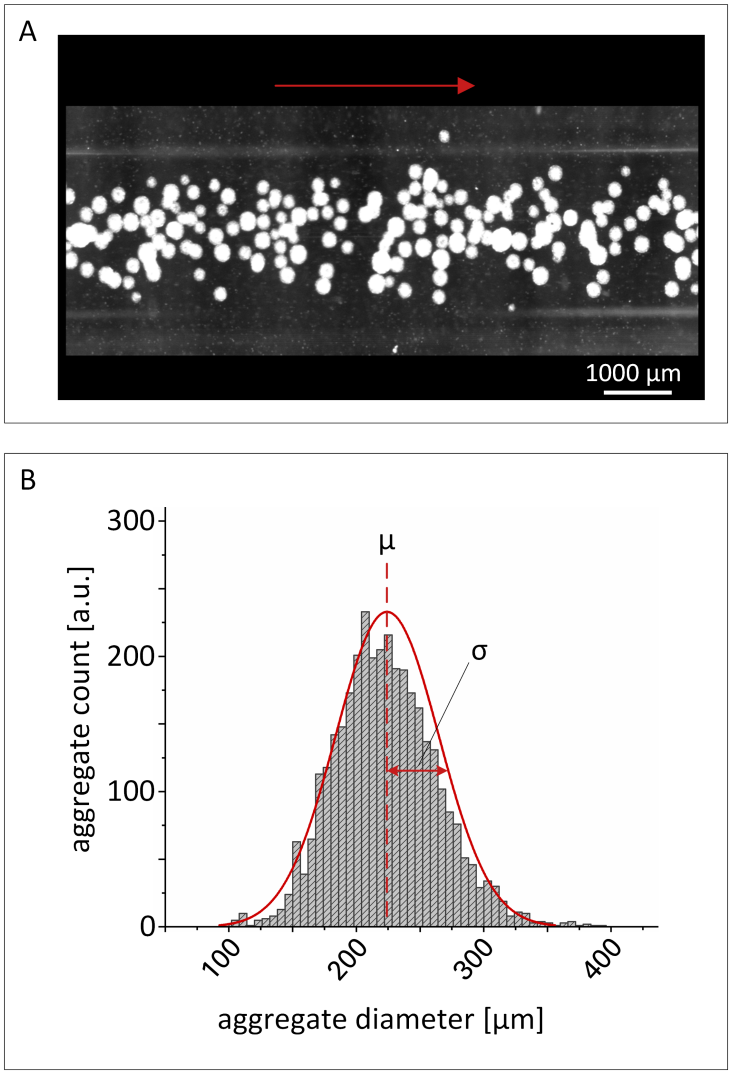

Figure 3.23: *Automated at-line image processing of suspension culture images provided aggregate size distributions.* ***(A)*** *In-flow images were captured by in situ microscopy for at-line image analysis.* ***(B)*** *The average aggregate diameter µ and its standard deviation σ were obtained as numerical data readout to characterize aggregate development in detail. Red arrow indicates direction of flow.*

In addition, images of control suspension cultures in well plates were acquired by using a digital lab microscope. In this case, manual imaging was accomplished within 3 min on average and provided a total of approximately 100 counts per image. Following image acquisition, statistical parameters that described the aggregate size distribution were derived by automated image analysis. In this context, the average aggregate diameter μ together with the average diameter's standard deviation σ were identified as suitable parameters to characterize the formation of aggregates (fig. 3.23, bottom).

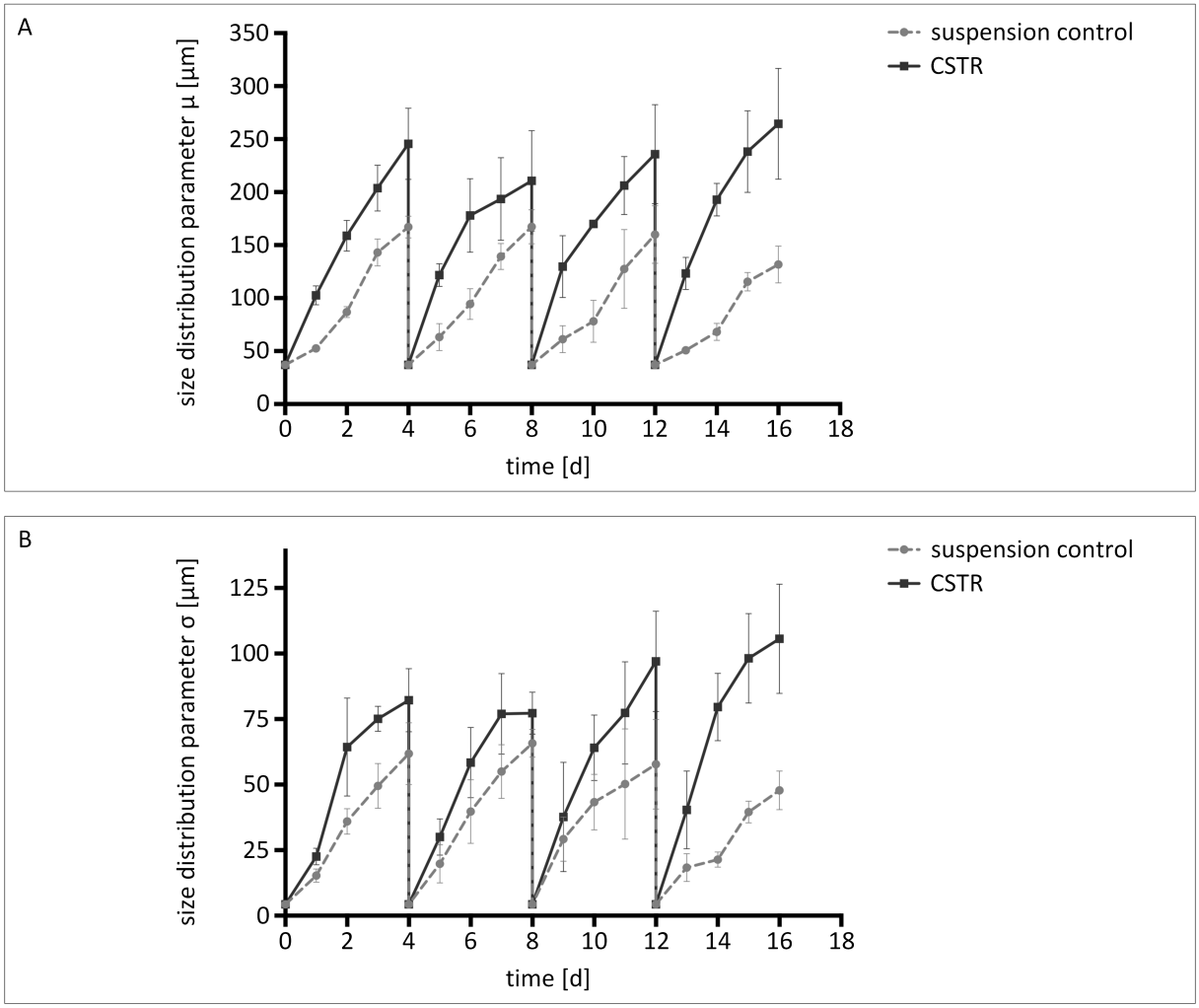

Figure 3.24: *Characterization of aggregate formation during suspension culture. The automated imaging of CSTR cultures and manual imaging of static control suspension cultures provided a detailed characterization of the aggregation behavior of hiPSCs by plotting* ***(A)*** *the average aggregate diameter μ and* ***(B)*** *standard deviation σ as a function of culture duration. (error bars indicate mean ± SD from n = 3 experiments)*

Plotting of the mean aggregate diameter μ revealed recurring size increases throughout each passage (fig. 3.24 A). For CSTR and static suspension control cultures, a starting size of approximately 50 µm was observed for aggregates in every passage. From there on, aggregate size development was detected to vary between culture formats. For CSTR cultures, mean aggregate diameters of approxi-

mately 120 µm were detected 24 h after re-seeding. Towards the end of each passage, mean aggregate diameters were no greater than 260 µm. Static suspension control cultures, on the other hand, showed lower aggregate diameters from day 1 onwards. Here, mean aggregate diameters were consistently smaller by 50 - 90 µm compared to CSTR cultured aggregates. In accordance with this observation, end-point aggregate sizes increased to about 150 µm. To assess aggregate size uniformity, the mean diameter's standard deviation σ was investigated as additional size distribution parameter (fig. 3.24 B). Starting at approximately 5 µm for suspension control and CSTR setups, the average standard deviation σ increased to 75 µm for CSTR cultures during passage 1 and 2. However, throughout the third and fourth passage, notably higher deviations were detected. Here, the standard deviation resulted in end-point measurements in the range of 100 µm. Static control cultures showed comparably lower end-point deviation values of approximately 60 µm during all passages. However, data did not deviate significantly.

In order to investigate a potential effect of altered cell health on hiPSC aggregation, LDH measurements were performed and compared between suspension culture setups. Here, as shown in fig. 3.25, comparable or decreased LDH activity levels were detected for CSTR cultures and suspension controls at all times.

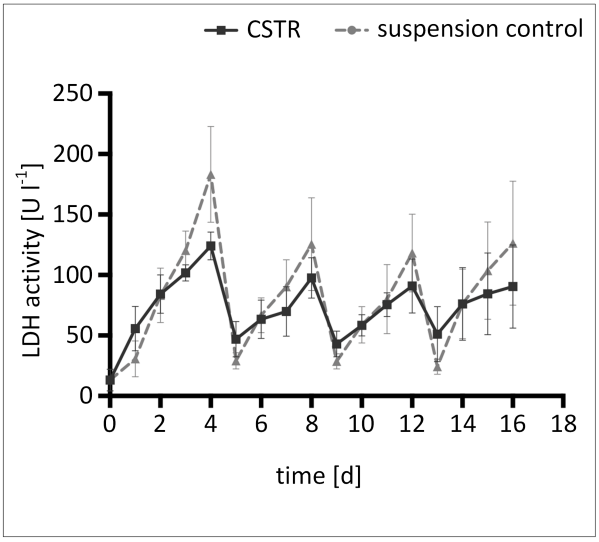

Figure 3.25: *Lactate dehydrogenase (LDH) activity in bioreactor and static control hiPSC suspension cultures. (n = 3)*

More precisely, LDH levels of control suspension cultures reached peak levels of 120 U l^{-1} - 180 U l^{-1} on days 4, 8, 12, and 16. LDH activity was subsequently reduced by the removal of non-viable cells from the suspension culture during passaging. For CSTR cultures, slightly lower LDH levels were measured that increased to a maximum of 90 U l^{-1} - 120 U l^{-1} on passaging days. These observations indicate that hiPSC proliferation is not affected by the CSTR system.

3.5.4 CSTR-cultured hiPSC express pluripotency markers

Changing cell culture conditions that are commonly used for pluripotent stem cells is often associated to the loss of pluripotency and spontaneous differentiation. To provide evidence for pluripotent stem cell qualities after CSTR suspension culture, the expression of the key pluripotency markers OCT3/4, SOX-2 and NANOG was evaluated by qRT-PCR and flow cytometry. Therefore, CSTR-cultured hiPSC were compared to the starter culture in mTeSR™1, a monolayer control culture in mTeSR™1, and a static suspension control culture in 1 ml of mTeSR™3D in multi-well plates.

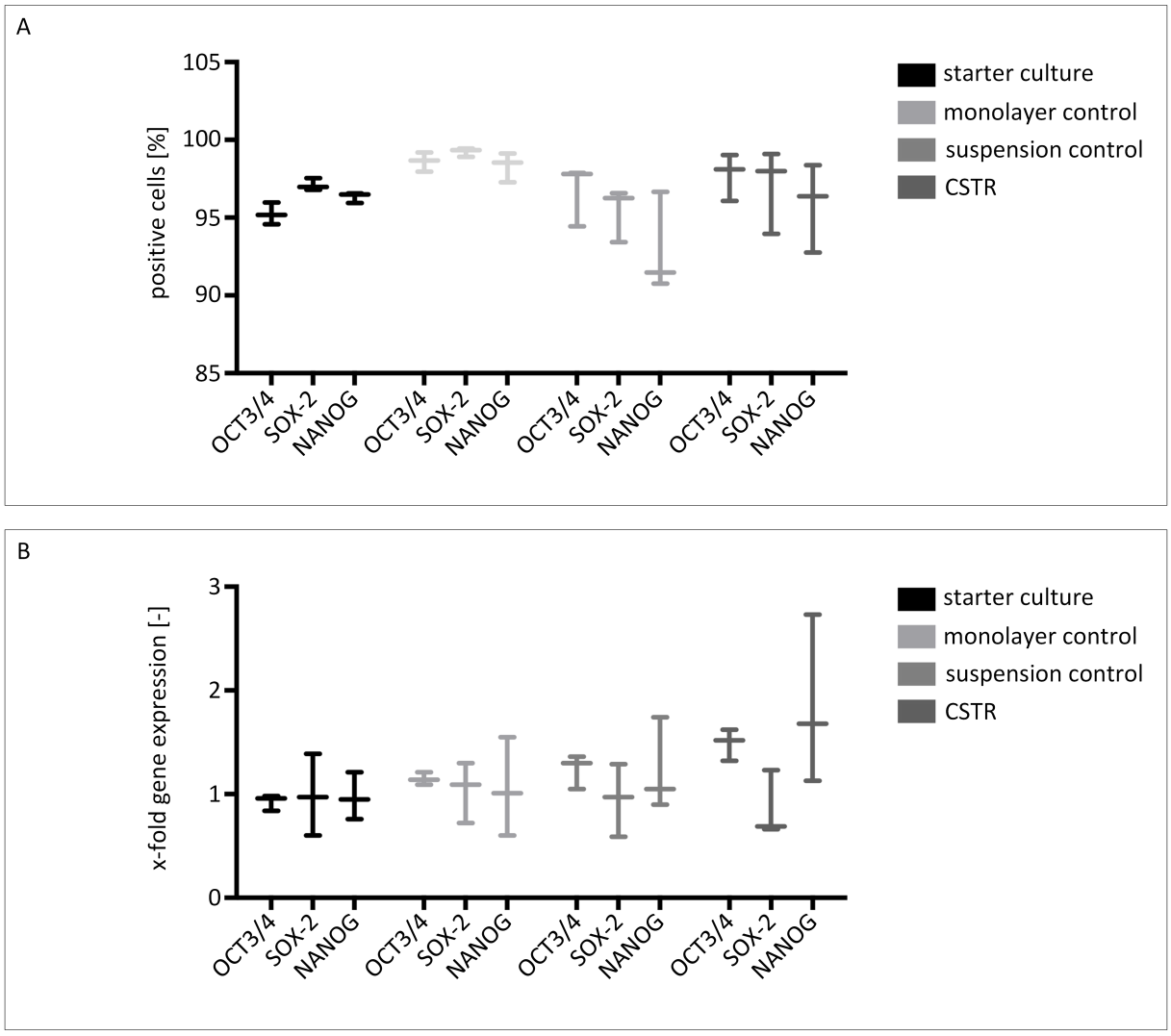

Figure 3.26: *IMR 90-4 hiPSCs preserve a pluripotency-associated protein phenotype throughout four passaging cycles.* ***(A)*** *Flow cytometry and* ***(B)*** *real time qRT-PCR analysis of monolayer cultures, suspension control cultures, and CSTR suspension cultures revealed consistent expression of pluripotency transcription factors for all modes of culture. (n = 3)*

On protein level, flow cytometry data revealed the robust expression of pluripotency-associated transcription factors in the monolayer control culture and in both suspension culture formats. More pre-

cisely, similar levels were obtained for the monolayer control, suspension control, and CSTR-cultured hiPSCs compared to the starter culture, indicating that the CSTR system is capable of upholding the pluripotent state of hiPSC (fig. 3.26 A). On the transcription level, a consistent expression of all investigated pluripotency-associated marker genes was detected. As shown in fig. 3.26 B, CSTR-cultured hiPSCs showed equal *OCT3/4*, *SOX-2* and *NANOG* gene expression compared to the expression profiles of controls and starter culture.

Pluripotency characteristics of hiPSCs in the different culture conditions were additionally assessed by using an unbiased bioinformatics assay termed PluriTest. In doing so, a global transcriptomic assessment of pluripotency was achieved by computing transcriptomic raw data (query) against an empirical model generated from hundreds of pluripotent and non-pluripotent cells and tissues. The output characteristics of the PluriTest algorithm were *Pluripotency* and *Novelty* scores. If criteria for both scores were met, the sampled cells were considered pluripotent. A summary of the data is shown in fig. 3.27. The data that was obtained form PluriTest analysis indicated that all samples pass both *Pluripotency* and *Novelty* score criteria.

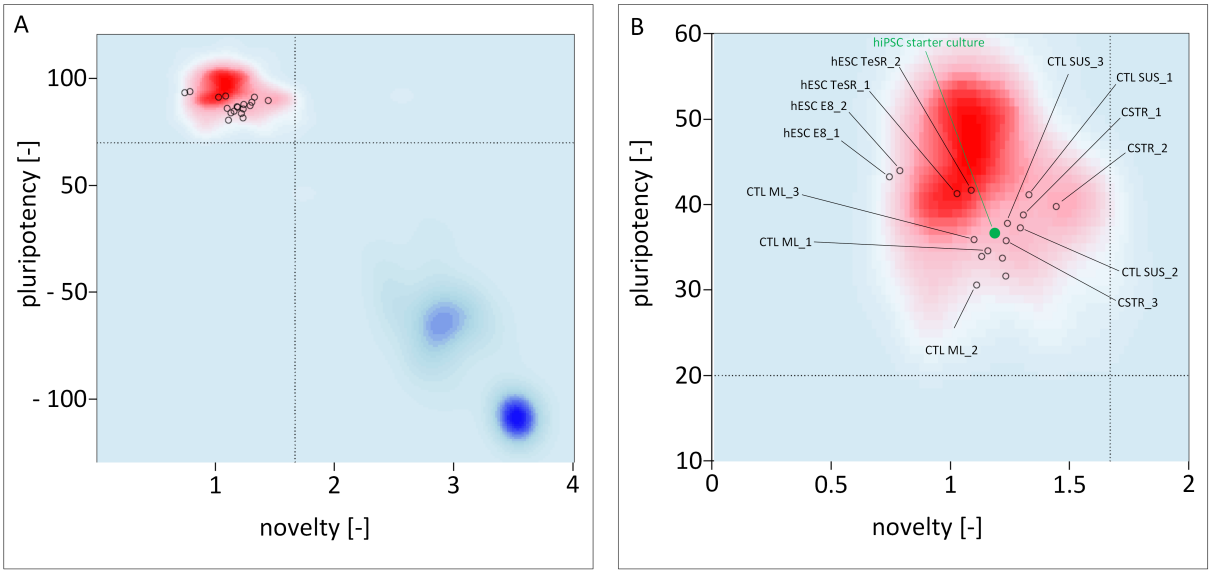

Figure 3.27: *PluriTest results from HT12v4 arrays.* ***(A)*** *PluriTest data was normalized to hESC H9 cultured in E8 medium and TeSR™ medium. The background encoded an empirical density map indicating areas of high Pluripotency/low Novelty scores (red) and high Novelty/low Pluripotency scores (blue) at thresholds for Pluripotency (20, horizontal) and Novelty (1.67, vertical). Scores were indicated with dashed lines. All samples passed both Pluripotency and Novelty score criteria.* ***(B)*** *Magnification of PluriTest results from (A). (n = 3)*

3.5.5 hiPSC show metabolic activity during CSTR culture

The transition of adherently-cultured hiPSCs to the 3D environment of a stirred vessel is often linked to cellular toxicity. To investigate potential effects in this sense, the metabolic activity of hiPSC cultures was assessed by at-line analysis of culture medium supernatant samples in order to investigate

hiPSC health during CSTR culture. In this regard, recurring metabolite concentration patterns for glucose, lactate, glutamine, and ammonia were detected, indicating functional carbon metabolism throughout all passages. The concentration of carbon source substances glucose and glutamine was observed to remain above 1 g l^{-1} and 1.2 mM, respectively, implying sufficient energy sources in both CSTR and suspension control culture formats (fig. 3.28 A and C). For the corresponding waste products, lactate and ammonia, peak concentrations of approximately 1.5 g l^{-1} and 2.5 mM were detected (fig. 3.28 B and D).

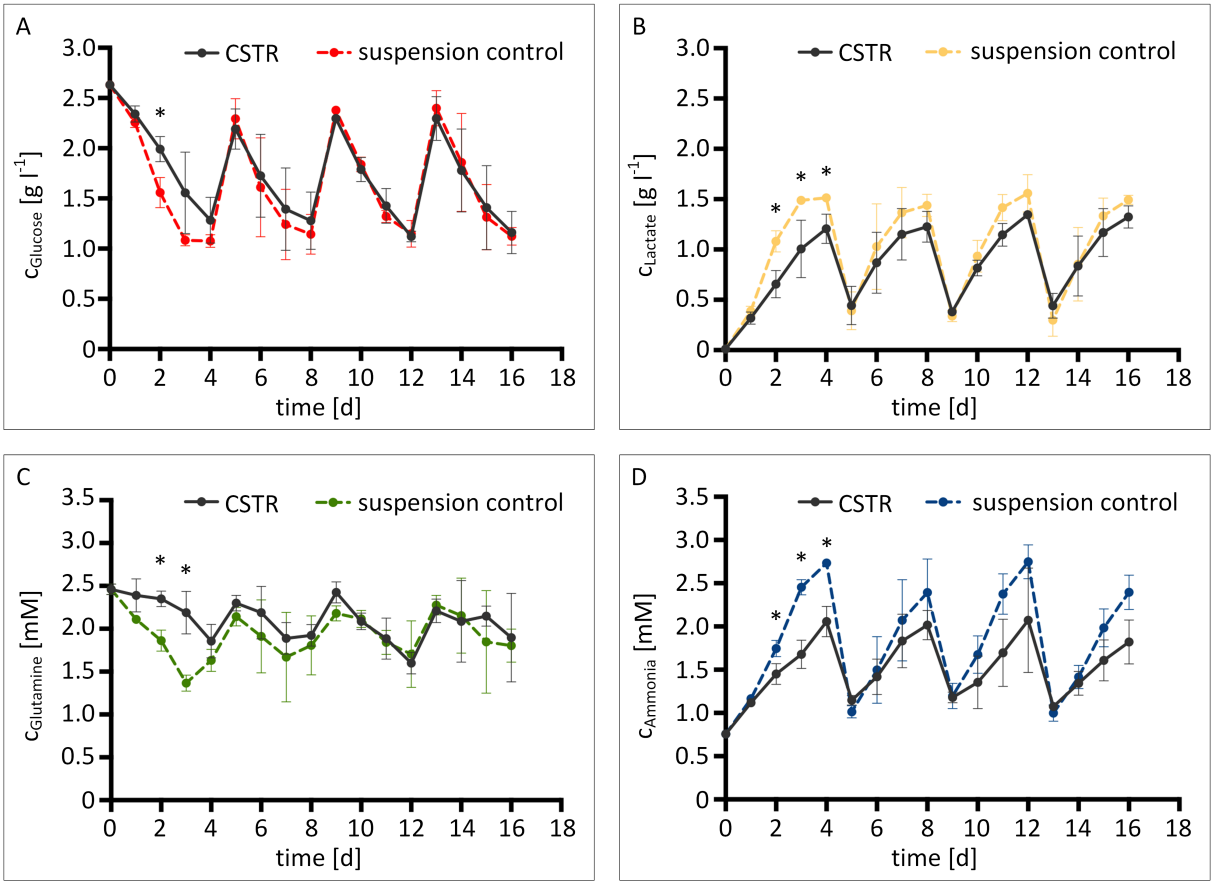

Figure 3.28: *Metabolite concentrations in hiPSC suspension cultures in bioreactors and static well plate suspension control cultures. At-line analysis of culture medium supernatants provided monitoring of* ***(A)*** *glucose,* ***(B)*** *lactose,* ***(C)*** *glutamine, and* ***(D)*** *ammonia metabolic activity. (n = 3)*

During bioreactor runs, dissolved oxygen content and pH levels were measured by using optical sensor spots. Dissolved oxygen levels remained above anoxia conditions at all times and were restored to ambient oxygen content of 20 % through medium change on passaging days (fig. 3.29 A). Regarding the culture medium pH level, measurements were done for bioreactor cultures only. In this case, pH values were in the range of 6.8 at their lowest, and approximately 7.2 immediately after passaging (fig. 3.29 B).

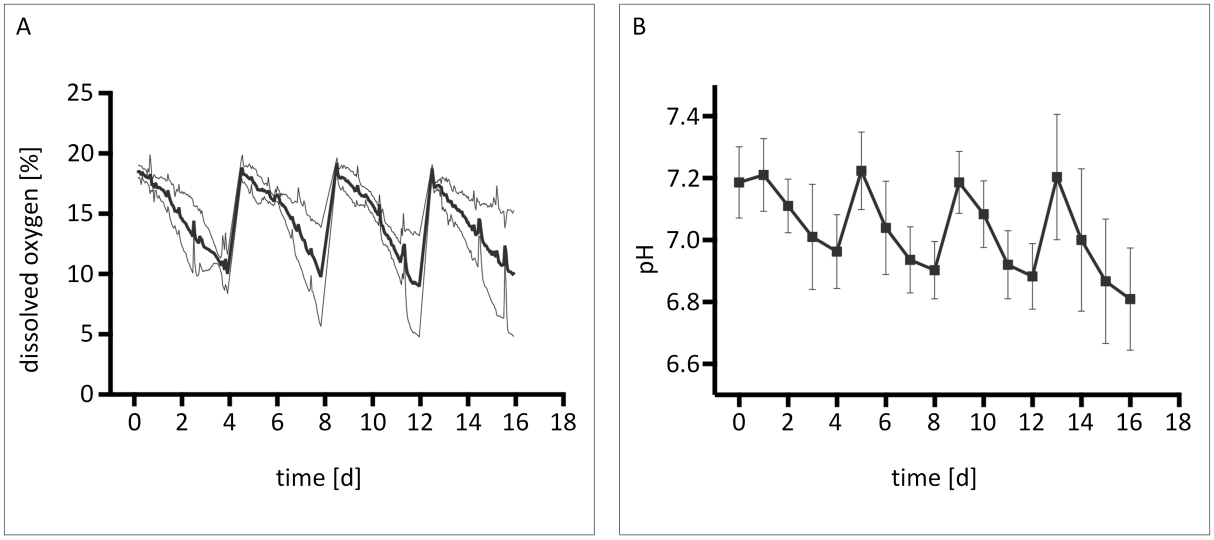

Figure 3.29: *Physical process parameter monitoring in hiPSC suspension cultures performed in CSTRs.* ***(A)*** *Measurements of dissolved oxygen concentrations and* ***(B)*** *pH levels were obtained by non-invasive optical sensor spots. (n = 3)*

Chapter 4

Discussion

4.1 Tailored platform for hiPSC suspension cultures

4.1.1 Incubator prototype

The prime objective of this study was the expansion of high quality hiPSCs that robustly exhibit a pluripotent nature. At the same time, hiPSC-specific process monitoring was necessary to pave the way for reproducible and scalable bioprocesses. With this aim in mind, a tailored incubator prototype was constructed to provide for an appropriate periphery for CSTR-based hiPSC culture, alongside with the necessary monitoring equipment for process characterization. The main purpose of the incubator was to generate optimal cell culture conditions in the atmosphere surrounding the CSTRs. By choosing a CSTR-in-incubator approach, the installation of CSTR-bound temperature probes and control actuators for each CSTR was redundant, thereby facilitating the use of the incubator for various CSTR sizes in future studies. In the same vein, each CSTR vessel was equipped with sensor spots for pH and dissolved oxygen measurements to allow for the monitoring of additional physical parameters. Here again, the considerable benefit of sensor spots lies in the independency from vessel size and shape. More precisely, the same sensor spots may be installed in miniature cultivation vessels as were used in this study, but as well in larger-scale models [134, 180, 34]. Since the corresponding transmitter cables ran freely in the incubation area, the simultaneous pH and dissolved oxygen monitoring in three small-scale vessels was possible. In the same manner, three motor drives were available and may be mounted onto CSTR designs of various working volumes. Another strength of the developed suspension culture platform is the incubator's capability to perform automated liquid handling. For instance, sampling of hiPSC suspensions from and to CSTRs was performed during hiPSC aggregate monitoring without the need for manual intervention. Yet, the implication of automated liquid handling may be extended further in future CSTR studies. For instance, the automated addition of mTeSR™3D feed medium is feasible. Prior to this installment, a refrigerated storage cabinet for cell culture media and feed medium batches in the rear cabinet of the incubator is necessary.

4.1.2 Rapid manufacture and optimization of CSTR designs

In order to lay the foundation for rapid suspension culture scaling and vessel flexibility, the majority of the CSTR components were fabricated by in-house 3D-printing (fig. 3.10). However, some components such as the glass vessel, the agitation shaft, and the impeller were crafted by other means. For instance, the impeller had to be milled as the printing resolution of the 3D-printer was insufficient to meet the amount of detail that was required for the impeller blade curvatures and the surface texture. Therefore, a variety of materials that are typically used in milling were tested in regard to their cytotoxic nature prior to manufacture (fig. 3.11). Here, an unexpected cytotoxic environment towards hiPSC proliferation was caused by POM-C, which is inconsistent with its use in medical engineering applications [170]. The toxic effect, however, is likely to be caused by leaching of formaldehyde monomers into the cell culture medium [73]. Another plausible explanation is the binding and depletion of growth factors from the medium. However, viability measurements that were performed immediately after inoculation indicated a rapid effect of POM-C-contaminated medium on hiPSC viability, which favors the leaching of formaldehyde as a likely reason for cytotoxicity (data not shown). In the end, PEEK was chosen for crafting the impeller geometries, which was mainly owed to its forthcoming workability compared to stainless steel.

For a proof-of-concept, the overall suitability of the suspension culture platform was demonstrated for one specific CSTR model. Thereby, the handcrafted glass vessels that were used ultimately dictated the overall bioreactor scale at this state. However, in the future, full bioreactor models that rely on 3D-printed components to an even greater extent are thinkable. In this context, high-resolution 3D-printing strategies that are based on stereolithography (SLA) are likely to play a major role. Thereby, the proportion of non-printed hardware parts such as glass components is further reduced. In addition, the fabrication process is completed within a few hours, which strengthens the role of 3D-printing technologies for rapid CSTR design and subsequent fabrication.

4.1.3 Sterilization of 3D-printed PLA components

Currently, a major drawback of PLA 3D-printed bioreactors is their sensitivity to thermoplastic deformation during hot-steam sterilization. As a solution to this, a variety of heat-resistant filaments are available for FDM-based 3D printing. Here, different polymers such as PEEK or PPSU are used instead of PLA, to name a few. The deployment of these thermally stable materials, however, dramatically increases the fabrication costs of 3D printed components. Nevertheless, several alternative options are available to provide reliable decontamination at considerably low temperatures, e.g. gamma irradiation or ethylene oxide gas sterilization. The application of irradiation, however, needs careful consideration, as the irradiation will alter the polymer structure of PLA [117]. Therefore, the application of multiple irradiation cycles is questionable. The use of ethylene oxide for gas sterilization is the gold standard procedure to disinfect heat-sensitive hardware components [100]. Yet, the

fact that residual ethylene oxide species need to be removed after the sterilization process render this technique a time-consuming one. Conclusively, the use of plasma sterilization as was performed in this study proved both a reliable and time-efficient sterilization method. Thereby, the sterilization of CSTRs was achieved at peak temperatures of approximately 40-50 °C within 90 min, thus evading thermoplastic deformation. Also, the reactive hydrogen peroxide species disintegrated into oxygen and hydrogen at the end of the plasma process. Consequently, the sterilized CSTRs were ready to use immediately after the sterilization process and no removal of residual species was required.

4.1.4 Computational model validation

The characterization of the flow field magnitude and orientation in a stirred vessel is commonly investigated by applying laser Doppler anemometry (LDA) [56, 179] or particle image velocimetry (PIV) [162, 175]. Although these experimental methods are reliable, they are at the same time not economically sustainable to characterize the complete 3D fluid flow within a typical bioreactor [61]. In contrast, CFD simulations offer a comparably fast and economical approximation of the physical environment in CSTR systems. As a result, the characterization of stirred bioreactor systems by CFD simulations has been progressing swiftly, thereby becoming an appreciated tool that facilitates outlining of bioreactor scaling studies *in silico* [61, 89, 181]. Analogous to this, a computational model was established to characterize the developed CSTR system for information on the occurring shear stress and the specific power input.

In a first step, the model accuracy was assessed by performing mesh refinement studies. The idea behind the stepwise increase of the mesh resolution is to balance the accuracy of the computation result versus the required solving time (tab. 3.2). At this point, it is common to define an accuracy corridor that is acceptable for the computation read-out parameter. For example, the larger portion of CFD simulations that were performed in the course of this study were run at mesh resolutions that, by default, held an accuracy deviation of 3.8 % to 4.7 % of the real solution. Although more precise computations were feasible, the necessary computation times were not acceptable from an economic point of view.

To validate the overall credibility of the developed CFD model, mixing time simulations were performed and compared to experimental data (fig. 3.20). For the majority of biopharmaceutical processes, a mix of 95 % homogeneity is assumed as an adequate mixing performance [42, 160]. Therefore, the confidence interval for the CFD-derived mixing time was adjusted accordingly (fig. 3.18). With few exceptions, the CFD-derived mixing times correlated to the experimental data with no significant deviations. In detail, the only variations that reached significance were obtained for mixing times that lead to 90 % and 95 % mixing homogeneity at 60 RPM, and 95 % mixing homogeneity at 100 RPM. Considering the general appearance of the data, a slight offset profile of the simulated mixing times from the experimental data was recognizable. However, it deserves mentioning that the experimental procedure of mixing time determination is highly experimentator-biased. Because the

measurement is primarily based on visual judgment, a reasonable step is to include multiple experimenters to analyze the mixing time footage. Still, taking into account the complexity of the mixing time simulation, the developed computational model proved to be well purposive of describing the fluid dynamic environment in the CSTR. Thus, the established CFD model was found appropriate to derive engineering parameters that were essential to closely characterize the developed CSTR system *in silico*.

4.1.5 Bioreactor characterization

The knowledge of a bioreactor's physical parameters is necessary to evaluate the suitability of any CSTR design for the specific bioprocess task. Those engineering characteristics commonly include, amongst others, the maximum fluid velocity, mixing time, specific power input, and shear stress. Therefore, a detailed characterization of the used cultivation system is vital for process scaling [60].

Power input

The power input describes the energy transfer of the stirrer into the cell culture medium and correlates with the ability to suspense particles and mixing behavior of bioreactors. In consequence, conclusions about the impeller configuration efficiency is possible [201]. In order to describe the power input, the Newton power number N_P is required. The determination of N_P is commonly done by measuring the torque on the stirrer shaft during mixing [17]. Therefore, special torque sensors have been developed and are routinely used for production fermenters in the pharmaceutical industry [88]. As an alternative, the use of CFD provides a robust starting point to give a good approximation of experimental data without the need to procure any sensor equipment. In this sense, a computational model was used to calculate N_P for $0.5 \leq N_{Re} \leq 3 \cdot 10^4$ in baffled and unbaffled agitation setups in order to convey the power input for the developed CSTR system. In fully developed turbulent flow, the power number is generally constant for a given impeller type, number of impellers, the off-bottom clearance h_c, and the impeller to tank diameter ratio d/D_B [6]. Referring to the results in section 3.4.4, N_P values of 1.6 for baffled and 0.55 for unbaffled setups for $N_{Re} \geq 10^4$ were obtained. The results show that the use of baffles strongly elevates mixing efficiency, which is also shown by flow field simulations in section 3.13. Thereby, the Newton power number is tripled in baffled agitation setups, which is in accord with observations described in the literature [70]. The specific power input P/V_L is a commonly used scale-up criterion in bioprocessing, and therefore a thorough characterization is vital. For baffled mixing at 75 RPM, the obtained power input was calculated and revealed a specific input of $P/V_L = 1.32$ W m^{-3}. This value, however, is lower compared to power input values that are common for mammalian cell culture. Here, power input values in the range of 10 to 250 W m^{-3} have been reported [88]. The comparably low power input for the CSTR system is mainly caused by the low rotating frequency of the stirrer. To be more precise, a maximum fluid velocity of $u_{max} = 0.125$ m s^{-1}

was obtained according to eq. 1.2. This value falls below the critical maximum fluid velocities of 1.0 and 2.0 m s^{-1} that is commonly not exceeded in mammalian bioprocesses due to shear sensitivity [38, 40, 72]. Interestingly, the resulting power input and maximum fluid velocity that were generated in this study were sufficient to suspense hiPSC aggregates and to prevent aggregate settling and subsequent clumping. This is likely due to the baffles that were incorporated into the CSTR system, which led to upward directed flow even for low impeller agitation speed.

Mixing time

The mixing time describes the time that is needed to completely blend a solution after the occurrence of a compound concentration or temperature gradient. These gradients in the culture medium have been reported to show negative effects on cell growth and protein expression [77]. Therefore, the mixing time represents one of the prime criteria for the characterization of bioreactors. The distribution of compound concentrations depends on multiple issues, such as CSTR geometrical layout, number of impellers, and power consumption [70]. In the industrial environment, various methods are established for the characterization of the mixing time. The most commonly applied methods comprise colorimetric, conductivity, and pH measurements [88, 101, 12]. To realize mixing time measurements that rely on the colorization of the bioreactor bulk fluid, optical accessibility is required. For windowless steel tank bioreactor systems, the measurement of conductivity or pH is performed. Therefore, an electrolyte or acidic solution is added to the fluid inside the bioreactor and the conductivity or pH value convergence is monitored by built-in sensors. The drawback of these methods lies in the alteration of the fluid flow pattern by the installed sensor probes. Additionally, the detection of dead zones becomes impossible as measurements are only obtained for the location of the conductivity or pH probe. Increasing the number of probes therefore might increase accuracy, however, complex sensor setups are not practical for small-scale bioreactors. In order to evaluate the mixing efficiency of the newly developed CSTR system, the mixing time was determined by colorization of the bulk fluid through the injection of a dye at increasing mixing speed (fig. 3.17). In this regard, mixing times were observed to remain below 60 s for even the slowest mixing rate. The average mixing time at moderate stirring was observed to be in the range of 15 s, which is sufficient to avoid effects on the cell growth in mammalian cell culture systems [77].

Shear stress

Due to the mechanical sensitivity of mammalian cells and the associated influence of shear stress, the effect of hydrodynamic forces on cell proliferation needs to be considered in order to ensure consistent product quality [194, 26]. In the delicate case of stem cells, fluid shear stress is further linked to affecting the expression of pluripotency markers and germ specification to the mesodermal, endodermal, and ectodermal lineages [186, 82]. To avoid compromising the overall cell quality, understanding these forces is essential to keep local shear stress in a range that cells can tolerate. In actively

aerated bioreactor vessels, the major proportion of shear stress is commonly caused by the rupture of bubbles that arise from the sparger [126]. In contrast, the CSTR system that was used in this study relies on passive aeration via head space gas exchange. Thereby, the shear stress that is caused by sparging is successfully omitted while the ingress of sufficient oxygen is ensured (fig. 3.29 A). Instead, the dominant source for shear stress, however, is the stirrer blades moving through the bulk liquid as was shown with the help of CFD simulations (fig. 3.14). As a result, the application of $4.5 \cdot 10^{-2}$ Pa that was in average generated by the agitation organ did not affect the pluripotent nature of IMR 90-4 cells which was demonstrated by PluriTest (fig. 3.27). However, it deserves mentioning that the application of shear stress during cell differentiation has been reported to play an important role by actively influencing the efficiency of lineage commitment in various stem cell lines [186, 1, 154, 164]. However, without the possibility of CFD simulations, the quantification of shear stress is a challenging task. Still, these findings suggest that fluid shear stress is an important characteristic that requires thorough quantification in order to pave the way for reproducible investigations in the future.

4.2 Advanced hiPSC bioprocess characterization through real-time monitoring of cell aggregation

In comparison to single cell suspension cultures, the size distribution of cell clusters is a process parameter that is confined to aggregate-forming species. For aggregates of 300 µm and greater, a necrotic microenvironment may appear, possibly due to oxygen, nutrient and metabolic byproduct limitations as was reported for ESC and neural stem cell (NSC) lines [188, 152], and/or spontaneous differentiation in regions close to the aggregate core [153]. Therefore, a main challenge of hiPSC suspension culture is the need to monitor the size of aggregates. The data that was obtained from *in situ* imaging showed that the developed CSTR system promoted the steady formation of aggregates at recurring size profiles (fig. 3.24). In average, hiPSC aggregates grew to spheroids of approximately 250 µm in diameter on passaging days. On the one hand, the obtained average maximum size of 250 µm indicated that the agitation setup was capable of preventing excessive aggregate clumping as shown in fig. 1.5. More importantly, the findings confirmed the postulation that aggregate development is highly dependent on the suspension culture vessel and the agitation setup [148]. This is exemplified when comparing the aggregate sizes in CSTR cultures and static control suspension cultures, for which notably lower end-point aggregate sizes of 180 µm were observed (fig. 3.24). The deviations between culture formats in regard to average aggregate diameter μ and standard deviation σ were largely owed to the increased probability of aggregates to merge into larger species in agitated cell suspensions. This, however, is further dependent on multiple factors such as the seeding density, impeller design, and agitation speed [158, 122, 81]. To offer a remedy to this challenge, the developed imaging device is independent of culture vessel dimensions due to its bypass-design, thus rendering it applicable for future scaling studies in bioreactors of various sizes and agitation setups.

The investigation of potential harm that might be inflicted onto hiPSC aggregates during liquid handling was a vital aspect to address. In this regard, the data that was obtained through the assessment of cell viability in combination with LDH activity measurements provided evidence for the suitability of the liquid handling procedure (fig. 3.22). Conclusively, and, as a further aspect to guarantee process reproducibility, manual sampling steps were successfully omitted. More importantly, by maintaining a closed-system-setup, the risk of contamination that would arise from manual sampling was thereby successfully evaded.

Another strength of the developed imaging system is the comparably high rate of aggregate counting. Referring to studies that were performed by others, aggregate size development was commonly investigated by imaging of manually drawn bioreactor samples. In doing so, considerably lower aggregate counts in the range of a few hundreds were obtained per measurement, which eventually had a notable impact on measurement accuracy [71, 74]. Additionally, sampled cells were discarded after analysis. In contrast, the technology that was developed in the context of this study delivered data at statistical relevance while omitting cell loss due to sampling. During operation, the suspension culture platform was able to generate data on aggregate formation at a rate of approximately 1000 aggregates per minute. Finally, the high-contrast black/white images that were generated by the dark-field mode of the *in situ* microscope were easily analyzed by the tailored algorithm. Hereby, a detection rate of approximately 90 % was achieved, which qualified the algorithm for reliable, high throughput aggregate size monitoring.

4.3 Energy metabolism of hiPSC aggregates

A detailed characterization of aggregate size development is also of essential interest to interpret energy metabolism and cell health in aggregate cultures. For instance, the activity of LDH enzymes was observed to be consistently higher in CSTR cultures at the beginning of each passage, indicating that cells were more prone to lysis in agitated environments after re-seeding (fig. 3.25). In the end, however, LDH activity was greater in static suspension control cultures towards passaging days. Considering the observation that hiPSC self-aggregation was enhanced in CSTR culture, the data consequently suggest that aggregation protected hiPSCs from cell lysis. One possibility to clarify this observation is to investigate cell apoptosis by e.g. flow cytometry analysis of phosphatidylserine by fluorochrome-labeled annexin V. From this data, a more detailed evaluation of cell health is possible.

The analysis of metabolites in CSTR and suspension control cultures showed that cell proliferation was increased in non-agitated culture setups at first. This was demonstrated by the comparably rapid consumption of glucose in the medium of static cultures during the first passage (fig. 3.28). This effect, however, was diminished throughout the following passaging cycles, and glucose uptake was synchronized between the two culture formats. In fact, significant variations between CSTR and static cultures were detected solely on day 2. The same development was observed for the formation of lac-

tate, where significantly higher concentrations were detected on days 2-4. The data thereby suggested that hiPSCs had fully adapted to the agitated culture environment and shear stress in a CSTR following the first passage.

In order to fully capture the metabolic profile, a precise knowledge on the current viable cell density is necessary. The acquisition of reliable cell count data for aggregated hiPSCs, however, is challenging. One reason for this is that, in contrast to single cell suspensions, sampling from an aggregate suspension culture is highly prone to falsifications due to the uneven distribution of biomass in the culture vessel. Therefore, cell yield was evaluated only at the end of each passage when the entire culture vessel would be harvested (data not shown). Still, a substantial portion of cultured cells were lost during the passaging procedure. More precisely, considerable amounts of cells remained clogged on the cell strainer during the dissociation step described in section 2.2.3. Thereby, the actual cell yield was dramatically reduced to an unknown extent. For future studies, a single cell-based passaging strategy will greatly increase manual handling of hiPSC suspensions [158]. In addition, it deserves mentioning that the aggregate size does not necessarily correlate to the number of cells that reside within. This is mainly caused by irregularly shaped cavities that are commonly found within aggregates [33].

Nevertheless, the data provided in fig. 3.28 further indicates that neither of the bulk carbon sources, glucose and glutamine, was depleted on passaging days. This observation implied that cell growth limitation did not occur as a consequence of energy source availability. A possible reason for the stagnation of cell proliferation is the accumulation of metabolic waste products. For instance, the concentration of lactate in suspension control cultures slightly surpassed the critical level of 1.3 g l^{-1} (15 mM) that has been reported to impair cell proliferation and productivity in hiPSCs [50]. This is recognizable by the lactate concentration plateaus towards the end of each passage (fig. 3.28). For CSTR cultures on the other hand, maximum lactate concentrations of about 1.2 g l^{-1}were reached, thereby evading the proliferation-inhibiting environment. The acidification of the cell culture medium by the accumulation of lactate is believed to limit cell growth by lowering the pH [185]. While some reports showed that the pH is one of the critical factors of decreased cell growth [174], other studies postulate that the accumulation of lactate delayed iPSC growth even under pH control [50]. Consequently, enhancing lactate removal from cell culture media by perfusion systems will be key strategies for achieving high cell densities while omitting effects on cell proliferation and pluripotency [25]. Glutamine is the other major energy substrate that provides for more than half of the cell energy metabolism in mammalian cell culture [102, 139, 199]. Besides its role as energy source, glutamine is a precursor for nucleic acid synthesis, and apoptosis is induced upon glutamine depletion [197, 147]. The corresponding waste product, ammonia, accumulates during batch cultures and has been shown to be significantly growth inhibitory to cells in culture [19]. The inhibitory effect, however, is highly dependent on the cell type and cell line in culture [123, 31]. For hiPSC batch cultures, ammonia-derived proliferation impairment was reported at concentrations above 5 mM [25]. By implication, the ammonia concentrations of 2-2.5 mM that were obtained for hiPSC suspension cultures performed in this study represent rather low ammonia levels and were unlikely to compromise cell growth.

As mentioned above, the availability of energy metabolites was not a limiting factor for cell proliferation. However, the cell culture medium that was used in this study was composed of a multitude of substances that, upon depletion, may have caused cell proliferation arrest. A list of biochemical compounds that were used in the medium was provided by Ludwig et al. [90]. Therefore, the depletion of a single or several substances poses another possible explanation for the stagnation of hiPSC growth. Compounds that were likely to cause this effect included the supplemented growth factors (e.g. GABA, pipecolic acid, bFGF, or TGF-β) and/or amino acids. To further investigate this assumption, enzyme-linked immunosorbent assay (ELISA) measurements of growth factors and high performance liquid chromatography (HPLC) analysis of amino acids are necessary.

4.4 Validation of hiPSC culture platform system functionality

To provide evidence for the suspension culture platform functionality, a range of biomarkers was subsequently investigated to verify the pluripotent nature of CSTR-cultured hiPSCs. In this regard, hiPSC identity was successfully demonstrated by mRNA quantification of the key pluripotency marker genes *OCT3/4*, *SOX-2*, and *NANOG* [84] as well as by PluriTest analysis (fig. 3.27). Further, the translation of marker genes was investigated by performing flow cytometry analysis on the protein level. As shown in figure 3.26, CSTR-cultured cells showed consistent gene expression patterns for *OCT3/4*, *SOX-2*, and *NANOG* compared to standard monolayer control cultures. In addition, flow cytometry data revealed the robust protein expression of OCT3/4, SOX-2 and NANOG in CSTR-hiPSCs after four passaging cycles.

The data was further strengthened by the confirmation of cell pluripotency by the mRNA-matching assay termed PluriTest [106]. The PluriTest relies on a bioinformatic approach that was initially developed to replace the teratoma assay. Until recently, the teratoma assay has remained the assay of choice to demonstrate pluripotency of stem cells *in vivo* [43]. For producing teratomas, undifferentiated hiPSCs are injected into immunocompromised mice, commonly sub-cutaneous, intramuscular, under the capsule of the kidney, or into the spinal chord [55, 183, 15]. Throughout the resultant tumor formation, the animals need to be continuously monitored until the tumor is removed for analysis. Besides the arising ethical questions, teratoma assays are time-consuming and laborious, and take up to four months until the mature teratomas are excised out of the animals to be assessed for the presence of cells from the three germ layers by immunofluorescence staining. In addition, the standardization of animal-based assays remains a considerable challenge [107, 157].

In contrast, PluriTest is a purely data-driven, microarray-based approach to rapidly assess the pluripotent nature of hiPSC *in vitro* cultures . PluriTest predicts stem cell pluripotency by matching the transcriptome of the investigated sample against an empirical model that has been generated from a large dataset of gene expression profiles of pluripotent and non-pluripotent somatic cells and tissues. The assay not only indicates cell pluripotency, but it also reveals contamination by differen-

tiated cells, and genomic and epigenomic abnormalities that alter gene expression patterns as found in e.g. germ cell tumor cell lines [54]. The output characteristics of the PluriTest algorithm are two summary scores. The first summary score is the pluripotency score that indicates the pluripotency of the cell sample based on the similarity of its gene expression signature to gene expression profiles of validated pluripotent stem cell lines from the database. The second summary score is a novelty score that detects the presence of conspicuous gene expression patterns. In order to pass the PluriTest, a designated pluripotent cell line is characterized by simultaneously exhibiting a high pluripotency and a low-novelty score, which was shown for all CSTR and control samples (fig. 3.27). Consequently, the outcome of the combined gene and protein analysis robustly substantiated the suitability of the developed CSTR system to maintain the pluripotent state of suspension hiPSCs in the long term.

4.5 Conclusion & Outlook

The unique properties of human pluripotent stem cells have contributed to their growing significance in fields such as regenerative medicine, disease modeling, and drug discovery. To face the increasing demand for robust and reproducible hiPSC bioprocesses, a variety of engineering tools such as CAD, CFD simulations, and 3D-printing, were utilized to develop, construct, and characterize a highly versatile, CSTR-based hiPSC suspension culture platform that facilitated the characterization of hiPSC aggregation in real-time through the deployment of *in situ* microscopy. The functionality of the developed hiPSC culture system was successfully validated by confirming the maintenance of the pluripotent cell state on transcript and protein level following four passaging cycles. In this matter, the expression of key pluripotency markers was successfully confirmed by qRT-PCR and flow cytometry. In addition, the PluriTest algorithm was used to compare the genetic similarity of CSTR-cultured hiPSC to a large reference dataset of pluripotent hESCs. The positive PluriTest results ultimately substantiate the robust system functionality. Taken together, the combination of the developed CSTR system and tailored incubator prototype is a valuable tool for the robust expansion of high quality stem cells that simultaneously offers advanced characterization of aggregation in hiPSC suspension bioprocesses.

In a next step, it would be interesting to investigate the aggregation behavior of other stem cell types and cell lines that are derived from either murine or human origin e.g. ESCs, MSCs. Also, a full three-germ-layer differentiation profile of these cell types, including IMR 90-4 iPSCs, is of great interest. In this regard, the study of the impact of aggregate size on differentiation potential and efficiency is facilitated by the developed ISM system. To decrease manual labour, the automation of the ISM imaging procedure is possible. Therefore, the ISM will require external triggers from the incubator's SPS system. Likewise, the automated addition of feeding substrate is possible and will be a valuable asset for future CSTR experiments. To allow for a more economical use of culture medium, the fabrication of even smaller CSTR systems is easy to implement according to the engineering parameters guideline presented in section 3.4. In this sense, the generated CSTR CAD design is rapidly down-scaled and component manufacture is feasible at negligible expense. Here, alternative 3D printing techniques are readily available (e.g. SLA) to omit the use of manually crafted parts such as the glass vessel or stirrer. Likewise, hiPSC expansion runs may be conducted in printed CSTR designs of increasing scales to increase the culture volume and thus hiPSC yield as needed.

Bibliography

[1] Tabassum Ahsan and Robert M Nerem. Fluid shear stress promotes an endothelial-like phenotype during the early differentiation of embryonic stem cells. *Tissue Engineering Part A*, 16(11):3547–3553, 2010.

[2] Muhammad Al-Hajj and Michael F Clarke. Self-renewal and solid tumor stem cells. *Oncogene*, 23(43):7274, 2004.

[3] Michal Amit, Judith Chebath, Victoria Margulets, Ilana Laevsky, Yael Miropolsky, Kohava Shariki, Meital Peri, Idit Blais, Guy Slutsky, Michel Revel, et al. Suspension culture of undifferentiated human embryonic and induced pluripotent stem cells. *Stem Cell Reviews and Reports*, 6(2):248–259, 2010.

[4] Antje Appelt-Menzel, Alevtina Cubukova, Katharina Günther, Frank Edenhofer, Jörg Piontek, Gerd Krause, Tanja Stüber, Heike Walles, Winfried Neuhaus, and Marco Metzger. Establishment of a human blood-brain barrier co-culture model mimicking the neurovascular unit using induced pluri-and multipotent stem cells. *Stem cell reports*, 8(4):894–906, 2017.

[5] Antje Appelt-Menzel, Ivo Schwedhelm, Fabian Kühn, Alevtina Cubukova, Frank Edenhofer, Heike Walles, and Jan Hansmann. Evaluation of various bioreactor process systems for the production of induced pluripotent stem cells. *Journal of Translational Science*, 2(5):277–285, 2016.

[6] Piero M Armenante and Gwo-Ming Chang. Power consumption in agitated vessels provided with multiple-disk turbines. *Industrial & engineering chemistry research*, 37(1):284–291, 1998.

[7] Ariel A Avilion, Silvia K Nicolis, Larysa H Pevny, Lidia Perez, Nigel Vivian, and Robin Lovell-Badge. Multipotent cell lineages in early mouse development depend on sox2 function. *Genes & development*, 17(1):126–140, 2003.

[8] Ruchi Bajpai, Jacqueline Lesperance, Min Kim, and Alexey V Terskikh. Efficient propagation of single cells accutase-dissociated human embryonic stem cells. *Molecular Reproduction and Development: Incorporating Gamete Research*, 75(5):818–827, 2008.

[9] Celine Liu Bauwens, Raheem Peerani, Sylvia Niebruegge, Kimberly A Woodhouse, Eugenia Kumacheva, Mansoor Husain, and Peter W Zandstra. Control of human embryonic stem cell colony and aggregate size heterogeneity influences differentiation trajectories. *Stem cells*, 26(9):2300–2310, 2008.

[10] Glenn S Belinsky and Srdjan D Antic. Mild hypothermia inhibits differentiation of human embryonic and induced pluripotent stem cells. *Biotechniques*, 55(2):79–82, 2013.

[11] Jonathan I Betts, Steven D Doig, and Frank Baganz. Characterization and application of a miniature 10 ml stirred-tank bioreactor, showing scale-down equivalence with a conventional 7 l reactor. *Biotechnology progress*, 22(3):681–688, 2006.

[12] Mounir Bouaifi and Michel Roustan. Power consumption, mixing time and homogenisation energy in dual-impeller agitated gas–liquid reactors. *Chemical Engineering and Processing: Process Intensification*, 40(2):87–95, 2001.

[13] Stefan R Braam, Robert Passier, and Christine L Mummery. Cardiomyocytes from human pluripotent stem cells in regenerative medicine and drug discovery. *Trends in pharmacological sciences*, 30(10):536–545, 2009.

[14] Ludwik K Branski, Gerd G Gauglitz, David N Herndon, and Marc G Jeschke. A review of gene and stem cell therapy in cutaneous wound healing. *Burns*, 35(2):171–180, 2009.

[15] Ali H Brivanlou, Fred H Gage, Rudolf Jaenisch, Thomas Jessell, Douglas Melton, and Janet Rossant. Setting standards for human embryonic stem cells. *Science*, 300(5621):913–916, 2003.

[16] David E Buchholz, Sherry T Hikita, Teisha J Rowland, Amy M Friedrich, Cassidy R Hinman, Lincoln V Johnson, and Dennis O Clegg. Derivation of functional retinal pigmented epithelium from induced pluripotent stem cells. *Stem cells*, 27(10):2427–2434, 2009.

[17] Jochen Büchs, Ulrike Maier, Claudia Milbradt, and Bernd Zoels. Power consumption in shaking flasks on rotary shaking machines: I. power consumption measurement in unbaffled flasks at low liquid viscosity. *Biotechnology and Bioengineering*, 68(6):589–593, 2000.

[18] Paul W Burridge, David Anderson, Helen Priddle, Maria D Barbadillo Munoz, Sarah Chamberlain, Cinzia Allegrucci, Lorraine E Young, and Chris Denning. Improved human embryonic stem cell embryoid body homogeneity and cardiomyocyte differentiation from a novel v-96 plate aggregation system highlights interline variability. *Stem Cells*, 25(4):929–938, 2007.

[19] M Butler and RE Spier. The effects of glutamine utilisation and ammonia production on the growth of bhk cells in microcarrier cultures. *Journal of Biotechnology*, 1(3-4):187–196, 1984.

[20] LM Calvi, GB Adams, KW Weibrecht, JM Weber, DP Olson, MC Knight, RP Martin, E Schipani, P Divieti, F Rv Bringhurst, et al. Osteoblastic cells regulate the haematopoietic stem cell niche. *Nature*, 425(6960):841, 2003.

[21] Ian Chambers, Douglas Colby, Morag Robertson, Jennifer Nichols, Sonia Lee, Susan Tweedie, and Austin Smith. Functional expression cloning of nanog, a pluripotency sustaining factor in embryonic stem cells. *Cell*, 113(5):643–655, 2003.

[22] Ian Chambers, Jose Silva, Douglas Colby, Jennifer Nichols, Bianca Nijmeijer, Morag Robertson, Jan Vrana, Ken Jones, Lars Grotewold, and Austin Smith. Nanog safeguards pluripotency and mediates germline development. *Nature*, 450(7173):1230, 2007.

[23] Guokai Chen, Daniel R Gulbranson, Zhonggang Hou, Jennifer M Bolin, Victor Ruotti, Mitchell D Probasco, Kimberly Smuga-Otto, Sara E Howden, Nicole R Diol, Nicholas E Propson, et al. Chemically defined conditions for human ipsc derivation and culture. *Nature methods*, 8(5):424, 2011.

[24] Vincent C Chen, Sylvana M Couture, Jingjing Ye, Ziguang Lin, Giau Hua, Hsiao-I P Huang, Jun Wu, David Hsu, Melissa K Carpenter, and Larry A Couture. Scalable gmp compliant suspension culture system for human es cells. *Stem cell research*, 8(3):388–402, 2012.

[25] Xiaoli Chen, Allen Chen, Tsung Liang Woo, Andre BH Choo, Shaul Reuveny, and Steve KW Oh. Investigations into the metabolism of two-dimensional colony and suspended microcarrier cultures of human embryonic stem cells in serum-free media. *Stem Cells and Development*, 19(11):1781–1792, 2010.

[26] Yusuf Chisti. Hydrodynamic damage to animal cells. *Critical reviews in biotechnology*, 21(2):67–110, 2001.

[27] Lily Chu and David K Robinson. Industrial choices for protein production by large-scale cell culture. *Current opinion in biotechnology*, 12(2):180–187, 2001.

[28] Diana L Clarke, Clas B Johansson, Johannes Wilbertz, Biborka Veress, Erik Nilsson, Helena Karlström, Urban Lendahl, and Jonas Frisen. Generalized potential of adult neural stem cells. *Science*, 288(5471):1660–1663, 2000.

[29] Magdaline Costa, Mirella Dottori, Elizabeth Ng, Susan M Hawes, Koula Sourris, Pegah Jamshidi, Martin F Pera, Andrew G Elefanty, and Edouard G Stanley. The hesc line envy expresses high levels of gfp in all differentiated progeny. *Nature methods*, 2(4):259, 2005.

[30] Larry A Couture. Scalable pluripotent stem cell culture. *Nature biotechnology*, 28(6):562, 2010.

[31] HJ Cruz, CM Freitas, PM Alves, JL Moreira, and MJT Carrondo. Effects of ammonia and lactate on growth, metabolism, and productivity of bhk cells. *Enzyme and microbial technology*, 27(1-2):43–52, 2000.

[32] Ricardo Cruz-Acuña and Andrés J García. Synthetic hydrogels mimicking basement membrane matrices to promote cell-matrix interactions. *Matrix Biology*, 57:324–333, 2017.

[33] Stephen M Dang, Michael Kyba, Rita Perlingeiro, George Q Daley, and Peter W Zandstra. Efficiency of embryoid body formation and hematopoietic development from embryonic stem cells in different culture systems. *Biotechnology and bioengineering*, 78(4):442–453, 2002.

[34] Thomas Dreher, Ute Husemann, Thorsten Adams, Davy de Wilde, and Gerhard Greller. Design space definition for a stirred single-use bioreactor family from 50 to 2000 l scale. *Engineering in Life Sciences*, 14(3):304–310, 2014.

[35] Micha Drukker, Helena Katchman, Gil Katz, Smadar Even-Tov Friedman, Elias Shezen, Eran Hornstein, Ofer Mandelboim, Yair Reisner, and Nissim Benvenisty. Human embryonic stem cells and their differentiated derivatives are less susceptible to immune rejection than adult cells. *Stem cells*, 24(2):221–229, 2006.

[36] Leonardo DÕAiuto, Yun Zhi, Dhanjit Kumar Das, Madeleine R Wilcox, Jon W Johnson, Lora McClain, Matthew L MacDonald, Roberto Di Maio, Mark E Schurdak, Paolo Piazza, et al. Large-scale generation of human ipsc-derived neural stem cells/early neural progenitor cells and their neuronal differentiation. *Organogenesis*, 10(4):365–377, 2014.

[37] Dominik Egger, Ivo Schwedhelm, Jan Hansmann, and Cornelia Kasper. Hypoxic three-dimensional scaffold-free aggregate cultivation of mesenchymal stem cells in a stirred tank reactor. *Bioengineering*, 4(2):47, 2017.

[38] Regine Eibl, Dieter Eibl, Ralf Pörtner, Gerardo Catapano, and Peter Czermak. *Cell and tissue reaction engineering*. Springer Science & Business Media, 2008.

[39] Martin J Evans and Matthew H Kaufman. Establishment in culture of pluripotential cells from mouse embryos. *nature*, 292(5819):154, 1981.

[40] Christel Fenge, Cornelia Klein, Carsten Heuer, Ursula Siegel, and Elisabeth Fraune. Agitation, aeration and perfusion modules for cell culture bioreactors. *Cytotechnology*, 11(3):233–244, 1993.

[41] Francesca Ferraro, Cristina Lo Celso, and David Scadden. Adult stem cels and their niches. In *The Cell Biology of Stem Cells*, pages 155–168. Springer, 2010.

[42] Michael C Flickinger. *Encyclopedia of Industrial Biotechnology: Bioprocess, Bioseparation, and Cell Technology, 7 Volume Set*. John Wiley & Sons, ISBN, 2010.

[43] Karin Gertow, Stefan Przyborski, Jeanne F Loring, Jonathan M Auerbach, Olga Epifano, Timo Otonkoski, Ivan Damjanov, and Lars Ährlund-Richter. Isolation of human embryonic stem cell–derived teratomas for the assessment of pluripotency. *Current protocols in stem cell biology*, 3(1):1B–4, 2007.

[44] NK Gill, M Appleton, F Baganz, and GJ Lye. Quantification of power consumption and oxygen transfer characteristics of a stirred miniature bioreactor for predictive fermentation scale-up. *Biotechnology and bioengineering*, 100(6):1144–1155, 2008.

[45] Priyanka Gupta, Mohd-Zulhilmi Ismadi, Paul J Verma, Andreas Fouras, Sameer Jadhav, Jayesh Bellare, and Kerry Hourigan. Optimization of agitation speed in spinner flask for microcarrier structural integrity and expansion of induced pluripotent stem cells. *Cytotechnology*, 68(1):45–59, 2016.

[46] Sebastian Haas, Norbert Weidner, and Jürgen Winkler. Adult stem cell therapy in stroke. *Current opinion in neurology*, 18(1):59–64, 2005.

[47] Penelope J Hallett, Michela Deleidi, Arnar Astradsson, Gaynor A Smith, Oliver Cooper, Teresia M Osborn, Maria Sundberg, Michele A Moore, Eduardo Perez-Torres, Anna-Liisa Brownell, et al. Successful function of autologous ipsc-derived dopamine neurons following transplantation in a non-human primate model of parkinsonÕs disease. *Cell stem cell*, 16(3):269–274, 2015.

[48] Konrad Hochedlinger and Rudolf Jaenisch. Nuclear reprogramming and pluripotency. *Nature*, 441(7097):1061, 2006.

[49] Tracy A Hookway, Jessica C Butts, Emily Lee, Hengli Tang, and Todd C McDevitt. Aggregate formation and suspension culture of human pluripotent stem cells and differentiated progeny. *Methods*, 101:11–20, 2016.

[50] Ikki Horiguchi, Yusuke Urabe, Keiichi Kimura, and Yasuyuki Sakai. Effects of glucose, lactate and basic fgf as limiting factors on the expansion of human induced pluripotent stem cells. *Journal of bioscience and bioengineering*, 125(1):111–115, 2018.

[51] Chris S Hughes, Lynne M Postovit, and Gilles A Lajoie. Matrigel: a complex protein mixture required for optimal growth of cell culture. *Proteomics*, 10(9):1886–1890, 2010.

[52] Dietmar W Hutmacher and Harmeet Singh. Computational fluid dynamics for improved bioreactor design and 3d culture. *Trends in biotechnology*, 26(4):166–172, 2008.

[53] Richard O Hynes. Integrins: versatility, modulation, and signaling in cell adhesion. *Cell*, 69(1):11–25, 1992.

[54] International Stem Cell Initiative et al. Assessment of established techniques to determine developmental and malignant potential of human pluripotent stem cells. *Nature communications*, 9, 2018.

[55] Mason A Israel, Shauna H Yuan, Cedric Bardy, Sol M Reyna, Yangling Mu, Cheryl Herrera, Michael P Hefferan, Sebastiaan Van Gorp, Kristopher L Nazor, Francesca S Boscolo, et al. Probing sporadic and familial alzheimerÕs disease using induced pluripotent stem cells. *Nature*, 482(7384):216, 2012.

[56] Z Jaworski, AW Nienow, and KN Dyster. An lda study of the turbulent flow field in a baffled vessel agitated by an axial, down-pumping hydrofoil impeller. *The Canadian Journal of Chemical Engineering*, 74(1):3–15, 1996.

[57] Donghui Jing, Abhirath Parikh, John M Canty Jr, and Emmanuel S Tzanakakis. Stem cells for heart cell therapies. *Tissue Engineering Part B: Reviews*, 14(4):393–406, 2008.

[58] Tomáš Jirout and František Rieger. Impeller design for mixing of suspensions. *Chemical Engineering Research and Design*, 89(7):1144–1151, 2011.

[59] Johanna Jokinen, Elina Dadu, Petri Nykvist, Jarmo Käpylä, Daniel J White, Johanna Ivaska, Piia Vehviläinen, Hilkka Reunanen, Hannu Larjava, Lari Häkkinen, et al. Integrin-mediated cell adhesion to type i collagen fibrils. *Journal of Biological Chemistry*, 279(30):31956–31963, 2004.

[60] Beth Helene Junker. Scale-up methodologies for escherichia coli and yeast fermentation processes. *Journal of bioscience and bioengineering*, 97(6):347–364, 2004.

[61] Stephan Kaiser, Valentin Jossen, Carmen Schirmaier, Dieter Eibl, Silke Brill, Christian van den Bos, and Regine Eibl. Fluid flow and cell proliferation of mesenchymal adipose-derived stem cells in small-scale, stirred, single-use bioreactors. *Chemie Ingenieur Technik*, 85(1-2):95–102, 2013.

[62] Stephan C Kaiser, Regine Eibl, and Dieter Eibl. Engineering characteristics of a single-use stirred bioreactor at bench-scale: The mobius cellready 3l bioreactor as a case study. *Engineering in Life Sciences*, 11(4):359–368, 2011.

[63] Gordon M Keller. In vitro differentiation of embryonic stem cells. *Current opinion in cell biology*, 7(6):862–869, 1995.

[64] Henning Kempf, Christina Kropp, Ruth Olmer, Ulrich Martin, and Robert Zweigerdt. Cardiac differentiation of human pluripotent stem cells in scalable suspension culture. *Nature protocols*, 10(9):1345, 2015.

[65] Henning Kempf, Ruth Olmer, Christina Kropp, Michael Rückert, Monica Jara-Avaca, Diana Robles-Diaz, Annika Franke, David A Elliott, Daniel Wojciechowski, Martin Fischer, et al. Controlling expansion and cardiomyogenic differentiation of human pluripotent stem cells in scalable suspension culture. *Stem cell reports*, 3(6):1132–1146, 2014.

[66] Julie C Kiefer. Back to basics: Sox genes. *Developmental Dynamics*, 236(8):2356–2366, 2007.

[67] Hynda K Kleinman and George R Martin. Matrigel: basement membrane matrix with biological activity. In *Seminars in cancer biology*, volume 15, pages 378–386. Elsevier, 2005.

[68] Hynda K Kleinman, Mary L McGarvey, Lance A Liotta, Pamela Gehron Robey, Karl Tryggvason, and George R Martin. Isolation and characterization of type iv procollagen, laminin, and heparan sulfate proteoglycan from the ehs sarcoma. *Biochemistry*, 21(24):6188–6193, 1982.

[69] Matthias Kraume. Mischvorgänge–ein lebendiges arbeitsgebiet. *Chemie Ingenieur Technik*, 75(10):1456–1459, 2003.

[70] Matthias Kraume. *Mischen und Rühren: Grundlagen und moderne Verfahren*. John Wiley & Sons, 2006.

[71] Christina Kropp, Henning Kempf, Caroline Halloin, Diana Robles-Diaz, Annika Franke, Thomas Scheper, Katharina Kinast, Thomas Knorpp, Thomas O Joos, Axel Haverich, et al. Impact of feeding strategies on the scalable expansion of human pluripotent stem cells in single-use stirred tank bioreactors. *Stem cells translational medicine*, 5(10):1289–1301, 2016.

[72] Kurt T Kunas and Eleftherios T Papoutsakis. Damage mechanisms of suspended animal cells in agitated bioreactors with and without bubble entrainment. *Biotechnology and Bioengineering*, 36(5):476–483, 1990.

[73] Robert P Kusy and John Q Whitley. Degradation of plastic polyoxymethylene brackets and the subsequent release of toxic formaldehyde. *American journal of orthodontics and dentofacial orthopedics*, 127(4):420–427, 2005.

[74] Chee Keong Kwok, Yuichiro Ueda, Asifiqbal Kadari, Katharina Günther, Süleyman Ergün, Antoine Heron, Aletta C Schnitzler, Martha Rook, and Frank Edenhofer. Scalable stirred suspension culture for the generation of billions of human induced pluripotent stem cells using single-use bioreactors. *Journal of tissue engineering and regenerative medicine*, 12(2):e1076–e1087, 2018.

[75] Mai T Lam and Michael T Longaker. Comparison of several attachment methods for human ips, embryonic and adipose-derived stem cells for tissue engineering. *Journal of tissue engineering and regenerative medicine*, 6(S3):s80–s86, 2012.

[76] Robert Lanza, Robert Langer, and Joseph P Vacanti. *Principles of tissue engineering*. Academic press, 2011.

[77] Alvaro R Lara, Enrique Galindo, Octavio T Ramírez, and Laura A Palomares. Living with heterogeneities in bioreactors. *Molecular biotechnology*, 34(3):355–381, 2006.

[78] Andrew S Lee, Chad Tang, Mahendra S Rao, Irving L Weissman, and Joseph C Wu. Tumorigenicity as a clinical hurdle for pluripotent stem cell therapies. *Nature medicine*, 19(8):998, 2013.

[79] Oscar K Lee, Tom K Kuo, Wei-Ming Chen, Kuan-Der Lee, Shie-Liang Hsieh, and Tain-Hsiung Chen. Isolation of multipotent mesenchymal stem cells from umbilical cord blood. *Blood*, 103(5):1669–1675, 2004.

[80] Seung-Won Lee, Hye Jeong Lee, Han Sung Hwang, Kisung Ko, Dong Wook Han, and Kinarm Ko. Optimization of matrigel-based culture for expansion of neural stem cells. *Animal Cells and Systems*, 19(3):175–180, 2015.

[81] Yuguo Lei and David V Schaffer. A fully defined and scalable 3d culture system for human pluripotent stem cell expansion and differentiation. *Proceedings of the National Academy of Sciences*, 110(52):E5039–E5048, 2013.

[82] Hau Wan Leung, Allen Chen, Andre BH Choo, Shaul Reuveny, and Steve KW Oh. Agitation can induce differentiation of human pluripotent stem cells in microcarrier cultures. *Tissue Engineering Part C: Methods*, 17(2):165–172, 2010.

[83] Vered Levy, Catherine Lindon, Ying Zheng, Brian D Harfe, and Bruce A Morgan. Epidermal stem cells arise from the hair follicle after wounding. *The FASEB Journal*, 21(7):1358–1366, 2007.

[84] Mo Li and Juan Carlos Izpisua Belmonte. Ground rules of the pluripotency gene regulatory network. *Nature Reviews Genetics*, 18(3):180, 2017.

[85] Olle Lindvall, Zaal Kokaia, and Alberto Martinez-Serrano. Stem cell therapy for human neurodegenerative disorders–how to make it work. *Nature medicine*, 10(7s):S42, 2004.

[86] Ning Liu, Ru Zang, Shang-Tian Yang, and Yan Li. Stem cell engineering in bioreactors for large-scale bioprocessing. *Engineering in Life Sciences*, 14(1):4–15, 2014.

[87] Lye T Lock and Emmanuel S Tzanakakis. Stem/progenitor cell sources of insulin-producing cells for the treatment of diabetes. *Tissue engineering*, 13(7):1399–1412, 2007.

[88] Christian Löffelholz, Ute Husemann, Gerhard Greller, Wolfram Meusel, Jörg Kauling, Peter Ay, Matthias Kraume, Regine Eibl, and Dieter Eibl. Bioengineering parameters for single-use bioreactors: Overview and evaluation of suitable methods. *Chemie Ingenieur Technik*, 85(1-2):40–56, 2013.

[89] Christian Löffelholz, Stephan C Kaiser, Sören Werner, and Dieter Eibl. Cfd as a tool to characterize single-use bioreactors. *Single-Use Technology in Biopharmaceutical Manufacture*, pages 263–279, 2010.

[90] Tenneille E Ludwig, Mark E Levenstein, Jeffrey M Jones, W Travis Berggren, Erika R Mitchen, Jennifer L Frane, Leann J Crandall, Christine A Daigh, Kevin R Conard, Marian S Piekarczyk, et al. Derivation of human embryonic stem cells in defined conditions. *Nature biotechnology*, 24(2):185, 2006.

[91] Dongrui Ma, Murni Tio, Shin Hui Ng, Li Zeng, Christina Ying Yan Lim, Yi Zhao, and Eng King Tan. Derivation of human induced pluripotent stem cell (ipsc) line with lrrk2 gene r1398h variant in parkinson's disease. *Stem cell research*, 18:48–50, 2017.

[92] Paolo MacChiarini, Thorsten Walles, Christian Biancosino, and Heike Mertsching. First human transplantation of a bioengineered airway tissue. *The Journal of thoracic and cardiovascular surgery*, 128(4):638–641, 2004.

[93] Nimet Maherali, Tim Ahfeldt, Alessandra Rigamonti, Jochen Utikal, Chad Cowan, and Konrad Hochedlinger. A high-efficiency system for the generation and study of human induced pluripotent stem cells. *Cell stem cell*, 3(3):340–345, 2008.

[94] Michiko Mandai, Akira Watanabe, Yasuo Kurimoto, Yasuhiko Hirami, Chikako Morinaga, Takashi Daimon, Masashi Fujihara, Hiroshi Akimaru, Noriko Sakai, Yumiko Shibata, et al. Autologous induced stem-cell–derived retinal cells for macular degeneration. *New England Journal of Medicine*, 376(11):1038–1046, 2017.

[95] Gail R Martin. Isolation of a pluripotent cell line from early mouse embryos cultured in medium conditioned by teratocarcinoma stem cells. *Proceedings of the National Academy of Sciences*, 78(12):7634–7638, 1981.

[96] Shinji Masui, Yuhki Nakatake, Yayoi Toyooka, Daisuke Shimosato, Rika Yagi, Kazue Takahashi, Hitoshi Okochi, Akihiko Okuda, Ryo Matoba, Alexei A Sharov, et al. Pluripotency governed by sox2 via regulation of oct3/4 expression in mouse embryonic stem cells. *Nature cell biology*, 9(6):625, 2007.

[97] Giuseppe Mazza, Walid Al-Akkad, Andrea Telese, Lisa Longato, Luca Urbani, Benjamin Robinson, Andrew Hall, Kenny Kong, Luca Frenguelli, Giusi Marrone, et al. Rapid production of human liver scaffolds for functional tissue engineering by high shear stress oscillation-decellularization. *Scientific reports*, 7(1):5534, 2017.

[98] Sergey P Medvedev, Elena V Grigor'eva, Alexander I Shevchenko, Anastasia A Malakhova, Elena V Dementyeva, Alexander A Shilov, Evgeny A Pokushalov, Alla M Zaidman, Maria A Aleksandrova, Egor Yu Plotnikov, et al. Human induced pluripotent stem cells derived from fetal neural stem cells successfully undergo directed differentiation into cartilage. *Stem cells and development*, 20(6):1099–1112, 2010.

[99] Zara Melkoumian, Jennifer L Weber, David M Weber, Andrei G Fadeev, Yue Zhou, Paula Dolley-Sonneville, Jiwei Yang, Liqun Qiu, Catherine A Priest, Christopher Shogbon, et al. Synthetic peptide-acrylate surfaces for long-term self-renewal and cardiomyocyte differentiation of human embryonic stem cells. *Nature biotechnology*, 28(6):606, 2010.

[100] Gisela CC Mendes, Teresa RS Brandao, and Cristina LM Silva. Ethylene oxide sterilization of medical devices: a review. *American journal of infection control*, 35(9):574–581, 2007.

[101] W Meusel, C Löffelholz, Ulf Husemann, T Dreher, G Greller, and J Kauling. *Recommendations for process engineering characterisation of single-use bioreactors and mixing systems by using experimental methods*. DECHEMA, 2016.

[102] WM Miller, HW Blanch, and CR Wilke. A kinetic analysis of hybridoma growth and metabolism in batch and continuous suspension culture: effect of nutrient concentration, dilution rate, and ph. *Biotechnology and Bioengineering*, 67(6):853–871, 2000.

[103] Kaoru Mitsui, Yoshimi Tokuzawa, Hiroaki Itoh, Kohichi Segawa, Mirei Murakami, Kazutoshi Takahashi, Masayoshi Maruyama, Mitsuyo Maeda, and Shinya Yamanaka. The homeoprotein nanog is required for maintenance of pluripotency in mouse epiblast and es cells. *cell*, 113(5):631–642, 2003.

[104] Kateri A Moore and Ihor R Lemischka. Stem cells and their niches. *Science*, 311(5769):1880–1885, 2006.

[105] Arieh Moussaieff, Matthieu Rouleau, Daniel Kitsberg, Merav Cohen, Gahl Levy, Dinorah Barasch, Alina Nemirovski, Shai Shen-Orr, Ilana Laevsky, Michal Amit, et al. Glycolysis-mediated changes in acetyl-coa and histone acetylation control the early differentiation of embryonic stem cells. *Cell metabolism*, 21(3):392–402, 2015.

[106] Franz-Josef Müller, Björn Brändl, and Jeanne F Loring. Assessment of human pluripotent stem cells with pluritest. 2012.

[107] Franz-Josef Müller, Johanna Goldmann, Peter Löser, and Jeanne F Loring. A call to standardize teratoma assays used to define human pluripotent cell lines. *Cell stem cell*, 6(5):412–414, 2010.

[108] Franz-Josef Müller, Bernhard M Schuldt, Roy Williams, Dylan Mason, Gulsah Altun, Eirini P Papapetrou, Sandra Danner, Johanna E Goldmann, Arne Herbst, Nils O Schmidt, et al. A bioinformatic assay for pluripotency in human cells. *Nature methods*, 8(4):315, 2011.

[109] William L Murphy, Todd C McDevitt, and Adam J Engler. Materials as stem cell regulators. *Nature materials*, 13(6):547, 2014.

[110] Charles E Murry, Hans Reinecke, and Lil M Pabon. Regeneration gaps: observations on stem cells and cardiac repair. *Journal of the American College of Cardiology*, 47(9):1777–1785, 2006.

[111] Jennifer Nichols, Branko Zevnik, Konstantinos Anastassiadis, Hitoshi Niwa, Daniela Klewe-Nebenius, Ian Chambers, Hans Schöler, and Austin Smith. Formation of pluripotent stem cells in the mammalian embryo depends on the pou transcription factor oct4. *Cell*, 95(3):379–391, 1998.

[112] Sylvia Niebruegge, Andrea Nehring, Harald Bär, Magnus Schroeder, Robert Zweigerdt, and Juergen Lehmann. Cardiomyocyte production in mass suspension culture: embryonic stem cells as a source for great amounts of functional cardiomyocytes. *Tissue Engineering Part A*, 14(10):1591–1601, 2008.

[113] Alvin W Nienow, Georgina McLeod, and Christopher J Hewitt. Studies supporting the use of mechanical mixing in large scale beer fermentations. *Biotechnology letters*, 32(5):623–633, 2010.

[114] AW Nienow, DJ Wisdom, J Solomon, V Machon, and J Vlcek. The effect of rheological complexities on power consumption in an aerated, agitated vessel. *Chemical Engineering Communications*, 19(4-6):273–293, 1983.

[115] Hitoshi Niwa, Jun-ichi Miyazaki, and Austin G Smith. Quantitative expression of oct-3/4 defines differentiation, dedifferentiation or self-renewal of es cells. *Nature genetics*, 24(4):372, 2000.

[116] Satoshi Nori, Yohei Okada, Akimasa Yasuda, Osahiko Tsuji, Yuichiro Takahashi, Yoshiomi Kobayashi, Kanehiro Fujiyoshi, Masato Koike, Yasuo Uchiyama, Eiji Ikeda, et al. Grafted human-induced pluripotent stem-cell–derived neurospheres promote motor functional recovery after spinal cord injury in mice. *Proceedings of the National Academy of Sciences*, page 201108077, 2011.

[117] Pramono Nugroho, Hiroshi Mitomo, Fumio Yoshii, and Tamikazu Kume. Degradation of poly (l-lactic acid) by γ-irradiation. *Polymer Degradation and Stability*, 72(2):337–343, 2001.

[118] Jeannette Nussbaum, Elina Minami, Michael A Laflamme, Jitka AI Virag, Carol B Ware, Amanda Masino, Veronica Muskheli, Lil Pabon, Hans Reinecke, and Charles E Murry. Transplantation of undifferentiated murine embryonic stem cells in the heart: teratoma formation and immune response. *The FASEB Journal*, 21(7):1345–1357, 2007.

[119] Yingzi Oh, Heming Wei, Dongrui Ma, Xiaoming Sun, and Reginald Liew. Clinical applications of patient-specific induced pluripotent stem cells in cardiovascular medicine. *Heart*, 98(6):443–449, 2012.

[120] Koji Okamoto, Hitoshi Okazawa, Akihiko Okuda, Masaharu Sakai, Masami Muramatsu, and Hiroshi Hamada. A novel octamer binding transcription factor is differentially expressed in mouse embryonic cells. *Cell*, 60(3):461–472, 1990.

[121] Keisuke Okita, Tomoko Ichisaka, and Shinya Yamanaka. Generation of germline-competent induced pluripotent stem cells. *nature*, 448(7151):313, 2007.

[122] Ruth Olmer, Andreas Lange, Sebastian Selzer, Cornelia Kasper, Axel Haverich, Ulrich Martin, and Robert Zweigerdt. Suspension culture of human pluripotent stem cells in controlled, stirred bioreactors. *Tissue Engineering Part C: Methods*, 18(10):772–784, 2012.

[123] Sadettin S Ozturk, Mark R Riley, and Bernhard O Palsson. Effects of ammonia and lactate on hybridoma growth, metabolism, and antibody production. *Biotechnology and bioengineering*, 39(4):418–431, 1992.

[124] Sofie OÕBrien, Yonsil Park, Samira Azarin, and Wei-Shou Hu. Cell culture bioprocess technology: Biologics and beyond. In *Cell Culture Technology*, pages 1–21. Springer, 2018.

[125] Felicia W Pagliuca, Jeffrey R Millman, Mads Gürtler, Michael Segel, Alana Van Dervort, Jennifer Hyoje Ryu, Quinn P Peterson, Dale Greiner, and Douglas A Melton. Generation of functional human pancreatic β cells in vitro. *Cell*, 159(2):428–439, 2014.

[126] Eleftherios T Papoutsakis. Fluid-mechanical damage of animal cells in bioreactors. *Trends in Biotechnology*, 9(1):427–437, 1991.

[127] In-Hyun Park, Rui Zhao, Jason A West, Akiko Yabuuchi, Hongguang Huo, Tan A Ince, Paul H Lerou, M William Lensch, and George Q Daley. Reprogramming of human somatic cells to pluripotency with defined factors. *Nature*, 451(7175):141, 2008.

[128] Erika Pastrana, Violeta Silva-Vargas, and Fiona Doetsch. Eyes wide open: a critical review of sphere-formation as an assay for stem cells. *Cell stem cell*, 8(5):486–498, 2011.

[129] Ronak Patel and Abraham J Alahmad. Growth-factor reduced matrigel source influences stem cell derived brain microvascular endothelial cell barrier properties. *Fluids and Barriers of the CNS*, 13(1):6, 2016.

[130] JA Sánchez Pérez, EM Rodríguez Porcel, JL Casas López, JM Fernández Sevilla, and Y Chisti. Shear rate in stirred tank and bubble column bioreactors. *Chemical Engineering Journal*, 124(1-3):1–5, 2006.

[131] Maurizio Pesce and Hans R Schöler. Oct-4: gatekeeper in the beginnings of mammalian development. *Stem cells*, 19(4):271–278, 2001.

[132] Donald G Phinney and Darwin J Prockop. Concise review: mesenchymal stem/multipotent stromal cells: the state of transdifferentiation and modes of tissue repairÑcurrent views. *Stem cells*, 25(11):2896–2902, 2007.

[133] Julia M Polak and Anne E Bishop. Stem cells and tissue engineering: past, present, and future. *Annals of the New York Academy of Sciences*, 1068(1):352–366, 2006.

[134] Daria Popova, Adam Stonier, David Pain, Nigel J Titchener-Hooker, and Suzanne S Farid. Representative mammalian cell culture test materials for assessment of primary recovery technologies: A rapid method with industrial applicability. *Biotechnology journal*, 10(1):162–170, 2015.

[135] Mark J Powers, Dena M Janigian, Kathryn E Wack, Carolyn S Baker, Donna Beer Stolz, and Linda G Griffith. Functional behavior of primary rat liver cells in a three-dimensional perfused microarray bioreactor. *Tissue engineering*, 8(3):499–513, 2002.

[136] Sharon C Presnell, Bryon Petersen, and Mohammad Heidaran. Stem cells in adult tissues. In *Seminars in cell & developmental biology*, volume 13, pages 369–376. Elsevier, 2002.

[137] Darwin J Prockop, Carl A Gregory, and Jeffery L Spees. One strategy for cell and gene therapy: harnessing the power of adult stem cells to repair tissues. *Proceedings of the National Academy of Sciences*, 100(suppl 1):11917–11923, 2003.

[138] Kristiina Rajala, Mari Pekkanen-Mattila, and Katriina Aalto-Setälä. Cardiac differentiation of pluripotent stem cells. *Stem cells international*, 2011, 2011.

[139] Lawrence J Reitzer, Burton M Wice, and David Kennell. Evidence that glutamine, not sugar, is the major energy source for cultured hela cells. *Journal of Biological Chemistry*, 254(8):2669–2676, 1979.

[140] Benjamin E Reubinoff, Martin F Pera, Chui-Yee Fong, Alan Trounson, and Ariff Bongso. Embryonic stem cell lines from human blastocysts: somatic differentiation in vitro. *Nature biotechnology*, 18(4):399, 2000.

[141] Tannishtha Reya, Sean J Morrison, Michael F Clarke, and Irving L Weissman. Stem cells, cancer, and cancer stem cells. *nature*, 414(6859):105, 2001.

[142] Angie Rizzino. Sox2 and oct-3/4: a versatile pair of master regulators that orchestrate the self-renewal and pluripotency of embryonic stem cells. *Wiley Interdisciplinary Reviews: Systems Biology and Medicine*, 1(2):228–236, 2009.

[143] Daisy A Robinton and George Q Daley. The promise of induced pluripotent stem cells in research and therapy. *Nature*, 481(7381):295, 2012.

[144] Elen S Rosler, Gregory J Fisk, Ximena Ares, John Irving, Takumi Miura, Mahendra S Rao, and Melissa K Carpenter. Long-term culture of human embryonic stem cells in feeder-free conditions. *Developmental dynamics: an official publication of the American Association of Anatomists*, 229(2):259–274, 2004.

[145] Mitchell H Rosner, M Alessandra Vigano, Keiko Ozato, Paula M Timmons, Francoise Poirie, Peter WJ Rigby, and Louis M Staudt. A pou-domain transcription factor in early stem cells and germ cells of the mammalian embryo. *Nature*, 345(6277):686, 1990.

[146] JH Rushton. Power characteristics of mixing impellers part 1. *Chem. Eng. Prog.*, 46:395–404, 1950.

[147] Anna Sanfeliu and Gregory Stephanopoulos. Effect of glutamine limitation on the death of attached chinese hamster ovary cells. *Biotechnology and bioengineering*, 64(1):46–53, 1999.

[148] Magnus Schroeder, Sylvia Niebruegge, Andreas Werner, Elmar Willbold, Monika Burg, Manfred Ruediger, Loren J Field, Juergen Lehmann, and Robert Zweigerdt. Differentiation and lineage selection of mouse embryonic stem cells in a stirred bench scale bioreactor with automated process control. *Biotechnology and bioengineering*, 92(7):920–933, 2005.

[149] Mariane Secco, Eder Zucconi, Natassia M Vieira, Luciana LQ Fogaça, Antonia Cerqueira, Maria Denise F Carvalho, Tatiana Jazedje, Oswaldo K Okamoto, Alysson R Muotri, and Mayana Zatz. Multipotent stem cells from umbilical cord: cord is richer than blood! *Stem cells*, 26(1):146–150, 2008.

[150] Vincent FM Segers and Richard T Lee. Stem-cell therapy for cardiac disease. *Nature*, 451(7181):937, 2008.

[151] Cheryle A Séguin, Jonathan S Draper, Andras Nagy, and Janet Rossant. Establishment of endoderm progenitors by sox transcription factor expression in human embryonic stem cells. *Cell stem cell*, 3(2):182–195, 2008.

[152] Arindom Sen, Michael S Kallos, and Leo A Behie. Effects of hydrodynamics on cultures of mammalian neural stem cell aggregates in suspension bioreactors. *Industrial & engineering chemistry research*, 40(23):5350–5357, 2001.

[153] Margarida Serra, Catarina Brito, Claudia Correia, and Paula M Alves. Process engineering of human pluripotent stem cells for clinical application. *Trends in biotechnology*, 30(6):350–359, 2012.

[154] Mehdi Shafa, Roman Krawetz, Yuan Zhang, Jerome B Rattner, Anna Godollei, Henry J Duff, and Derrick E Rancourt. Impact of stirred suspension bioreactor culture on the differentiation of murine embryonic stem cells into cardiomyocytes. *BMC cell biology*, 12(1):53, 2011.

[155] Mehdi Shafa, Kirsten Sjonnesen, Akihiro Yamashita, Shiying Liu, Marek Michalak, Michael S Kallos, and Derrick E Rancourt. Expansion and long-term maintenance of induced pluripotent stem cells in stirred suspension bioreactors. *Journal of tissue engineering and regenerative medicine*, 6(6):462–472, 2012.

[156] Shikha Sharma, Ravali Raju, Siguang Sui, and Wei-Shou Hu. Stem cell culture engineering–process scale up and beyond. *Biotechnology journal*, 6(11):1317–1329, 2011.

[157] Steven D Sheridan, Vasudha Surampudi, and Raj R Rao. Analysis of embryoid bodies derived from human induced pluripotent stem cells as a means to assess pluripotency. *Stem cells international*, 2012, 2012.

[158] Harmeet Singh, Pamela Mok, Thavamalar Balakrishnan, Siti Norfiza Binte Rahmat, and Robert Zweigerdt. Up-scaling single cell-inoculated suspension culture of human embryonic stem cells. *Stem cell research*, 4(3):165–179, 2010.

[159] RK Sinnott. *Coulson & Richardson's Chemical Enginering: Volume 6/Chemical Engineering Design*. Elsevier Butterworth Heinemann, 1999.

[160] Winfried Storhas. Bioreaktoren und periphere einrichtungen. *Vieweg, Braunschweig*, 1994.

[161] Lars Storsberg. *Comsol Multiphysics Strömungsmechanik (CFD) Training Course*. Comsol Multiphysics GmbH.

[162] Philippe Sucosky, Diego F Osorio, Jason B Brown, and G Paul Neitzel. Fluid mechanics of a spinner-flask bioreactor. *Biotechnology and bioengineering*, 85(1):34–46, 2004.

[163] Rutger-Jan Swijnenburg, Sonja Schrepfer, Feng Cao, Jeremy I Pearl, Xiaoyan Xie, Andrew J Connolly, Robert C Robbins, and Joseph C Wu. In vivo imaging of embryonic stem cells reveals patterns of survival and immune rejection following transplantation. *Stem cells and development*, 17(6):1023–1029, 2008.

[164] Jaymi T Taiani, Roman J Krawetz, Nicole I zur Nieden, Yiru Elizabeth Wu, Michael S Kallos, John R Matyas, and Derrick E Rancourt. Reduced differentiation efficiency of murine embryonic stem cells in stirred suspension bioreactors. *Stem cells and development*, 19(7):989–998, 2009.

[165] Kazutoshi Takahashi, Koji Tanabe, Mari Ohnuki, Megumi Narita, Tomoko Ichisaka, Kiichiro Tomoda, and Shinya Yamanaka. Induction of pluripotent stem cells from adult human fibroblasts by defined factors. *cell*, 131(5):861–872, 2007.

[166] Kazutoshi Takahashi and Shinya Yamanaka. Induction of pluripotent stem cells from mouse embryonic and adult fibroblast cultures by defined factors. *cell*, 126(4):663–676, 2006.

[167] Takanori Takebe, Keisuke Sekine, Masahiro Enomura, Hiroyuki Koike, Masaki Kimura, Takunori Ogaeri, Ran-Ran Zhang, Yasuharu Ueno, Yun-Wen Zheng, Naoto Koike, et al. Vascularized and functional human liver from an ipsc-derived organ bud transplant. *Nature*, 499(7459):481, 2013.

[168] Norifumi Takeda, Rajan Jain, Matthew R LeBoeuf, Qiaohong Wang, Min Min Lu, and Jonathan A Epstein. Interconversion between intestinal stem cell populations in distinct niches. *Science*, 334(6061):1420–1424, 2011.

[169] Ze-Wei Tao, Mohamed Mohamed, Matthew Hogan, Laura Gutierrez, and Ravi K Birla. Optimizing a spontaneously contracting heart tissue patch with rat neonatal cardiac cells on fibrin gel. *Journal of tissue engineering and regenerative medicine*, 11(1):153–163, 2017.

[170] SH Teoh, ZG Tang, and Garth W Hastings. Thermoplastic polymers in biomedical applications: structures, properties and processing. In *Handbook of biomaterial properties*, pages 270–301. Springer, 1998.

[171] James A Thomson, Joseph Itskovitz-Eldor, Sander S Shapiro, Michelle A Waknitz, Jennifer J Swiergiel, Vivienne S Marshall, and Jeffrey M Jones. Embryonic stem cell lines derived from human blastocysts. *science*, 282(5391):1145–1147, 1998.

[172] Tudorita Tumbar, Geraldine Guasch, Valentina Greco, Cedric Blanpain, William E Lowry, Michael Rendl, and Elaine Fuchs. Defining the epithelial stem cell niche in skin. *Science*, 303(5656):359–363, 2004.

[173] Jochen Utikal, Nimet Maherali, Warakorn Kulalert, and Konrad Hochedlinger. Sox2 is dispensable for the reprogramming of melanocytes and melanoma cells into induced pluripotent stem cells. *Journal of cell science*, 122(19):3502–3510, 2009.

[174] Sandra Varum, Ana S Rodrigues, Michelle B Moura, Olga Momcilovic, Charles A Easley IV, João Ramalho-Santos, Bennett Van Houten, and Gerald Schatten. Energy metabolism in human pluripotent stem cells and their differentiated counterparts. *PloS one*, 6(6):e20914, 2011.

[175] Raghavan V Venkat, Louis R Stock, and Jeffrey J Chalmers. Study of hydrodynamics in microcarrier culture spinner vessels: a particle tracking velocimetry approach. *Biotechnology and bioengineering*, 49(4):456–466, 1996.

[176] L Vija, D Farge, J-F Gautier, P Vexiau, C Dumitrache, A Bourgarit, F Verrecchia, and J Larghero. Mesenchymal stem cells: Stem cell therapy perspectives for type 1 diabetes. *Diabetes & metabolism*, 35(2):85–93, 2009.

[177] LG Villa-Diaz, AM Ross, J Lahann, and PH Krebsbach. Concise review: the evolution of human pluripotent stem cell culture: from feeder cells to synthetic coatings. *Stem cells*, 31(1):1–7, 2013.

[178] Sanna Vuoristo, Ismo Virtanen, Minna Takkunen, Jaan Palgi, Yamato Kikkawa, Patricia Rousselle, Kiyotoshi Sekiguchi, Timo Tuuri, and Timo Otonkoski. Laminin isoforms in human embryonic stem cells: synthesis, receptor usage and growth support. *Journal of cellular and molecular medicine*, 13(8b):2622–2633, 2009.

[179] Si-Jing Wang and Jian-Jiang Zhong. A novel centrifugal impeller bioreactor. i. fluid circulation, mixing, and liquid velocity profiles. *Biotechnology and bioengineering*, 51(5):511–519, 1996.

[180] Henry Weichert, J Lüders, Mario Becker, Thorsten Adams, and J Weyand. Integrated optical single-use sensors: Moving toward a true single-use factory for biologics and vaccine production. *BioProcess International*, 12:20–24, 2014.

[181] Sören Werner, Stephan C Kaiser, Matthias Kraume, and Dieter Eibl. Computational fluid dynamics as a modern tool for engineering characterization of bioreactors. *Pharmaceutical Bioprocessing*, 2(1):85–99, 2014.

[182] Marius Wernig, Alexander Meissner, Ruth Foreman, Tobias Brambrink, Manching Ku, Konrad Hochedlinger, Bradley E Bernstein, and Rudolf Jaenisch. In vitro reprogramming of fibroblasts into a pluripotent es-cell-like state. *nature*, 448(7151):318, 2007.

[183] Robin L Wesselschmidt. The teratoma assay: an in vivo assessment of pluripotency. In *Human Pluripotent Stem Cells*, pages 231–241. Springer, 2011.

[184] Jessica M Williams, Adebisi Adewunmi, Rachel M Schek, Colleen L Flanagan, Paul H Krebsbach, Stephen E Feinberg, Scott J Hollister, and Suman Das. Bone tissue engineering using polycaprolactone scaffolds fabricated via selective laser sintering. *Biomaterials*, 26(23):4817–4827, 2005.

[185] Anja Wilmes, Caroline Rauch, Giada Carta, Georg Kern, Florian Meier, Wilfried Posch, Doris Wilflingseder, Lyle Armstrong, Majlinda Lako, Mario Beilmann, et al. Towards optimisation of induced pluripotent cell culture: Extracellular acidification results in growth arrest of ipsc prior to nutrient exhaustion. *Toxicology in Vitro*, 45:445–454, 2017.

[186] Russell P Wolfe, Jardin Leleux, Robert M Nerem, and Tabassum Ahsan. Effects of shear stress on germ lineage specification of embryonic stem cells. *Integrative Biology*, 4(10):1263–1273, 2012.

[187] Jincheng Wu, Yongjia Fan, and Emmanuel S Tzanakakis. Increased culture density is linked to decelerated proliferation, prolonged g1 phase, and enhanced propensity for differentiation of self-renewing human pluripotent stem cells. *Stem cells and development*, 24(7):892–903, 2014.

[188] Jincheng Wu, Mahboubeh Rahmati Rostami, Diana P Cadavid Olaya, and Emmanuel S Tzanakakis. Oxygen transport and stem cell aggregation in stirred-suspension bioreactor cultures. *PLoS One*, 9(7):e102486, 2014.

[189] Chunhui Xu, Margaret S Inokuma, Jerrod Denham, Kathaleen Golds, Pratima Kundu, Joseph D Gold, and Melissa K Carpenter. Feeder-free growth of undifferentiated human embryonic stem cells. *Nature biotechnology*, 19(10):971, 2001.

[190] Ren-He Xu, Ruthann M Peck, Dong S Li, Xuezhu Feng, Tenneille Ludwig, and James A Thomson. Basic fgf and suppression of bmp signaling sustain undifferentiated proliferation of human es cells. *Nature methods*, 2(3):185, 2005.

[191] Shinpei Yamaguchi, Hironobu Kimura, Masako Tada, Norio Nakatsuji, and Takashi Tada. Nanog expression in mouse germ cell development. *Gene Expression Patterns*, 5(5):639–646, 2005.

[192] Shinya Yamanaka. Strategies and new developments in the generation of patient-specific pluripotent stem cells. *Cell stem cell*, 1(1):39–49, 2007.

[193] Young Il Yeom, Guy Fuhrmann, Catherine E Ovitt, Alexander Brehm, Kazuyuki Ohbo, Michael Gross, K Hubner, and HR Scholer. Germline regulatory element of oct-4 specific for the totipotent cycle of embryonal cells. *Development*, 122(3):881–894, 1996.

[194] Benjamin S Youn, Arindom Sen, Michael S Kallos, Leo A Behie, Adele Girgis-Gabardo, Natasza Kurpios, Maria Barcelon, and John A Hassell. Large-scale expansion of mammary epithelial stem cell aggregates in suspension bioreactors. *Biotechnology progress*, 21(3):984–993, 2005.

[195] Junying Yu, Maxim A Vodyanik, Kim Smuga-Otto, Jessica Antosiewicz-Bourget, Jennifer L Frane, Shulan Tian, Jeff Nie, Gudrun A Jonsdottir, Victor Ruotti, Ron Stewart, et al. Induced pluripotent stem cell lines derived from human somatic cells. *science*, 318(5858):1917–1920, 2007.

[196] Huabing Yuan, Nicoletta Corbi, Claudio Basilico, and Lisa Dailey. Developmental-specific activity of the fgf-4 enhancer requires the synergistic action of sox2 and oct-3. *Genes & development*, 9(21):2635–2645, 1995.

[197] Mariia Yuneva, Nicola Zamboni, Peter Oefner, Ravi Sachidanandam, and Yuri Lazebnik. Deficiency in glutamine but not glucose induces myc-dependent apoptosis in human cells. *The Journal of cell biology*, 178(1):93–105, 2007.

[198] Holm Zaehres, M William Lensch, Laurence Daheron, Sheila A Stewart, Joseph Itskovitz-Eldor, and George Q Daley. High-efficiency rna interference in human embryonic stem cells. *Stem Cells*, 23(3):299–305, 2005.

[199] H Ronald Zielke, Pinar T Ozand, J Tyson Tildon, David A Sevdalian, and Marvin Cornblath. Reciprocal regulation of glucose and glutamine utilization by cultured human diploid fibroblasts. *Journal of cellular physiology*, 95(1):41–48, 1978.

[200] Marko Zlokarnik. *Stirring*. John Wiley & Sons, 2008.

[201] Marko Zlokarnik. *Rührtechnik: Theorie und Praxis*. Springer-Verlag, 2013.

[202] Nicole I zur Nieden, Jaymi T Cormier, Derrick E Rancourt, and Michael S Kallos. Embryonic stem cells remain highly pluripotent following long term expansion as aggregates in suspension bioreactors. *Journal of biotechnology*, 129(3):421–432, 2007.

Chapter 5

Supplementary

EVOS Algorithm syntax

Algorithm 5.1 Image processing algorithm used for images acquired by digital inverted lab microscope.

```
run("Set Scale...", "distance=446 known=1000 unit=um");
run("8-bit");
run("Median...", "radius=10");
run("Unsharp Mask...", "radius=10 mask=0.50");
run("Gamma...", "value=0.50");
run("Subtract Background...", "rolling=150 light");
run("Enhance Contrast...", "saturated=0,01 normalize");
run("Auto Threshold", "method=Default");
setOption("BlackBackground", false);
run("Make Binary");
makeRectangle(1556, 1178, 492, 156);
setForegroundColor(255, 255, 255);
run("Fill", "slice");
run("Select None");
selectWindow("del 25 d1.tif");
run("Analyze Particles...", "size=2000-3140000 circularity=0.80-1.00
        show=Outlines display exclude include summarize");
```

ISM Algorithm syntax

Algorithm 5.2 Image processing algorithm used for images acquired by custom-built *in situ* microscope.

```
run("Set Scale...", "distance=100 known=586 unit=um");
run("8-bit");
run("Median...", "radius=3");
run("Unsharp Mask...", "radius=5 mask=0.50");
run("Gamma...", "value=1.25");
run("Subtract Background...", "rolling=12");
run("Enhance Contrast...", "saturated=1.2 normalize");
run("Auto Threshold", "method=Default white");
setOption("BlackBackground", false);
run("Make Binary");
run("Watershed");
run("Analyze Particles...", "size=2000.00-3140000.00 circularity=0.80-1.00
      show=Outlines display exclude include summarize");
```

Comsol syntax

Table 5.1: *Comsol syntax expressions*

Name	Comsol syntax expression	Unit
flow velocity	spf.U	m s^{-1}
viscous shear stress	spf.sr*spf.mu	Pa
turbulent shear stress	spf.sr*spf.muT	Pa
tracer concentration	c	mol m^{-3}
guassian function	gp1(t[1/s])	-

Table 5.2: *Variables used for stirrer power number computations*

Variable name	Comsol syntax	Unit	Description
tau_rw	x*(spf.T_stressy)-y*(spf.T_stressx)	N m^{-1}	Torque per area
P_rw	tau_rw*rot1.alphat	W m^{-2}	Power draw per area
NRe	Da^2*N0*rho_u/Re_mu	-	stirrer Reynolds number
Np	intop1(P_rw)/(N0^3*Da^5*rho_u)	-	stirrer power number

Publication list

- Antje Appelt-Menzel*, **Ivo Schwedhelm***, Fabian Kühn, Alevtina Cubukova, Frank Edenhofer, Heike Walles, and Jan Hansmann. Evaluation of various bioreactor process systems for the production of induced pluripotent stem cells. *Journal of Translational Science*, 2(5):277–285, 2016.

- Dominik Egger*, **Ivo Schwedhelm***, Jan Hansmann, and Cornelia Kasper. Hypoxic three-dimensional scaffold-free aggregate cultivation of mesenchymal stem cells in a stirred tank reactor. *Bioengineering*, 4(2):47, 2017.

- Ram-Kumar Ramani-Mohan*, **Ivo Schwedhelm***, Anna Finne-Wistrand, Melanie Krug, Thomas Schwarz, Franz Jakob, Heike Walles, and Jan Hansmann. Deformation strain is the main physical driver for skeletal precursors to undergo osteogenesis in earlier stages of osteogenic cell maturation. *Journal of Tissue Engineering and Regenerative Medicine*, 12(3):e1474–e1479, 2018.

- Jan Hansmann, **Ivo Schwedhelm**, Andreas Clementi, Dominik Egger, and Cornelia Kasper. Automation of cell culture processes. *Cell Culture Technology*, pages 155–168. Springer, 2018.

- Lisa Rödling, **Ivo Schwedhelm**, Saskia Kraus, Karen Bieback, Jan Hansmann, and Cornelia Lee-Thedieck. 3d models of the hematopoietic stem cell niche under steady-state and active conditions. *Scientific Reports*, 7(1):4625, 2017.

- Sebastian Schuerlein, Thomas Schwarz, Steffan Krziminski, Sabine Gätzner, Anke Hoppensack, **Ivo Schwedhelm**, Matthias Schweinlin, Heike Walles, and Jan Hansmann. A versatile modular bioreactor platform for tissue engineering. *Biotechnology Journal*, 12(2):1600326, 2017.

- Matthias Schweinlin, Sabine Wilhelm, **Ivo Schwedhelm**, Jan Hansmann, Rene Rietscher, Christian Jurowich, Heike Walles, and Marco Metzger. Development of an advanced primary human in vitro model of the small intestine. *Tissue Engineering Part C: Methods*, 22(9):873–883, 2016.

- Submitted: **Ivo Schwedhelm**, Daniela Zdzieblo, Antje Appelt-Menzel, Constantin Berger, Tobias Schmitz, Bernhard Schuldt, Andre Franke, Franz-Josef Müller, Ole Pless, Thomas Schwarz, Philipp Wiedemann, Heike Walles, Jan Hansmann. Automated real-time monitoring of human pluripotent stem cell aggregation in stirred tank reactors.

Acknowledgement

Prof. Jan Hansmann für eine exzellente Betreuung vor Ort und für die mir zur Verfügung gestellten Mittel und Möglichkeiten um das Projekt zu einem erfolgreichen Abschluss zu führen. Danke für das Gefühl, dass ich bei jeder Wind- und Wetterlage ein offenes Ohr finden würde.

Prof. Heike Walles dass ich Teil der LTERM Familie sein durfte. Danke für die einzigartige und wertschätzende Atmosphäre am Lehrstuhl an dem man nicht nur Wissenschaftler, sondern auch Mensch sein durfte.

Prof. Philipp Wiedemann für die äußerst solide Begleitung über meine Zeit an der HS Mannheim hinaus. Danke für das stete Interesse am Fortschritt der Arbeit und für all die wertvollen Ratschläge, die das Projekt maßgeblich geformt haben.

Thomas Schwarz für die Blicke hinter das fränkische Bollwerk während den unvergesslichen Fahrten nach Wien, Riad oder Sommerhausen.

Alevtina für die revitalisierenden After-Work-Treffen auf der alten Mainbrücke.

Steffan, SchürSe, Marc, Tobi Schmitz, Alan, Miri, Shabbaz für die erfolgreiche Verteidigung der Werkstatt gegen jegliche Form des grauen Alltags.

Daniela, Consti und Antje für den großen Einsatz während der Endphase des Projektes.

Alex Kahlig für eine wertvolle Freundschaft und seine Mission mich über die Ziellinie zu schubsen.

Meiner Segel-Crew Jenny, CeeDee, Erwin, Elli, Benny und Skippy für die Erfahrung auch bei Schräglage Zwiebeln zu schneiden.

Meinen Esslingern für die unerschütterliche Brücke in die schwäbische Heimat.

Meinen Unplugged-Band-Brüdern Chris und Matzi. Es war mir eine große Ehre mit euch die Fußgängerzonen Würzburgs zu beschallen!

Leo, Kerstin, Lui, Franzi, Muriel, Sebastian, Olga und Max für die Zeit in der Friedenstrasse 8.

Meinen Kollegen beim Juliusspital Weingut Dorothea, Wolfgang, Joe, Markus, Heiner, Ruth & Werner.

Meiner Familie für die unaufgeforderte (kulinarische) Unterstützung zu jeder Zeit.

Und natürlich dir Juli. Danke für unsere kleine, perfekte Welt.

Affidavit

I herewith confirm that my thesis entitled “A non-invasive microscopy platform for the online monitoring of hiPSC aggregation in suspension cultures in small-scale stirred tank bioreactors” is the result of my own work. I did not receive any help or support from commercial consultants. All sources and / or materials applied are listed and specified in the thesis.

Furthermore, I confirm that this thesis has not yet been submitted as part of another examination process neither in identical nor in similar form.

Würzburg,